Renato Manuel Monteiro Nora

Bachelor in Micro and Nanotechnologies Engineering

Characterization of undoped and doped ZnO Nanowires for Optoelectronic Applications

Dissertation submitted in partial fulfilment
of the requirements for the degree of

Master of Science in
Micro and Nanotechnologies Engineering

Advisor: Joana Vaz Pinto, Assistant Professor,
Faculty of Sciences and Technology,
NOVA University of Lisbon
Co-advisor: João Pedro Oliveira, Assistant Professor,
Faculty of Sciences and Technology,
NOVA University of Lisbon

Examination Committee:

Chairperson: Luís Miguel Pereira, Associate Professor of DCM, FCT-UNL
Vogal(s): Joana Vaz Pinto, Assistant Professor of DCM, FCT-UNL
Rita Salazar Branquinho, Assistant Professor of DCM, FCT-UNL

FACULDADE DE
CIÊNCIAS E TECNOLOGIA
UNIVERSIDADE NOVA DE LISBOA

September 2019

Characterization of undoped and doped ZnO Nanowires for Optoelectronic applications

Nobody ever figures out what life is all about, and it doesn´t matter. Explore the world.
Nearly everything is really interesting if you go into it deeply enough.

— Richard Feynman

Acknowledgements

I would like to thank my supervisor, Prof. Dra. Joana Vaz Pinto, and co-supervisor, Dr.João Pedro Oliveira, for all the guidance, time and availability provided to teach and help me, despite their busy schedules and to Ana Pimentel for all the supervision and assistance on the chemical synthesis, and also for being always available to answering my questions related to that matter.

I would also like to acknowledge Prof. Dr. Rodrigo Martins, in the quality of President of the Department of Science and Materials and thank you for all the passion and hard work that elevates our department and master´s course.

To Prof. Dr. Elvira Fortunato, in the quality of President of CENIMAT, my thank you for your incredible work and commitment to our investigation centre which is internationally acknowledge much due to your efforts and achievements.

My thank you to all the professors, docents and researchers, that teaches me and helped me to become a better engineer.

I would like to thank also to my fellow colleagues and friend that were doing their thesis at the same time as me for all the positive spirit, energy and good time that they show while working on our thesis.

To the people of room 202 and specially to my friends Carolina Natal, Margarida Glória, Joana Cristina, Ricardo Nogueira, Hadassa Valle, my thank you for enduring my jokes, for the longest and very interesting conversations, for the pauses in the study to drink coffee and for making me have the best time while studying hard.

To my closest friends, Luís Bettencourt, Guilherme Castelo, Guilherme Ferreira, Joan Concha and Mafalda Pina, thank you for studying with me and making all a lot easier and for making me learn that there´s other life beyond college.

To the most important and special friends, Bernardo Rodrigues, Sofia Pádua and Mariana Matias, for being always there in the hardest moments and the best ones, for making me be what I ‘am today.

Por fim, gostava de agradecer a toda a minha família, e em especial aos meus pais, por terem tornado isto possível e pelo apoio incondicional que demonstraram ao longo destes 5 anos.

Abstract

Metal oxide nanostructures such as ZnO have a huge impact due to its unique properties. This work focuses on the synthesis and characterization of ZnO NWs. In particular, Rietveld Refinement method is implemented to perform a deeper structural characterization of the nanostructure's properties.

Undoped and doped NWs (Ca, Eu, Ga) morphological, structural and optical properties were studied, varying the post-annealing temperature (in undoped nanowires) from 300 °C to 700 °C and doping concentration (in doped NWs) from 1 to 5 mol% on both microwave and conventional oven.

The structural and morphological characterization of undoped NWs by SEM showed that the microwave synthesis promoted the formation of wurtzite ZnO nanowires and flower-like structures, while conventional synthesis formed more dispersed nanowires. In both cases average dimensions of 5 μm of length and near 1 μm of diameter were observed with a very broad size distribution.

The synthesis of doped NWs revealed morphology changes when compared to the undoped ones, and in particular for the europium doped NWs, $Eu(OH)_3$ was formed attached to ZnO NWs. UV-Vis spectroscopy was also performed to determine the band gap. Differences were observed between undoped and doped ZnO NWs and between not annealed ZnO NWs and the annealed ones with band gap values between 3.1 and 3.2 eV, as also reported in literature.

Rietveld Refinement method was implemented on these NWs to study the evolution of the crystal structure of NWs. The lattice parameters were determined, and the results showed a decrease of the c/a ratio with increasing annealing temperature in undoped NWs. However, the overall tendency does not follow a standard behavior in doped ZnO NWs. No major differences were found when comparing microwave and conventional synthesis in the doped material. A protocol for Rietveld Refinement was developed as a tool for a deeper microstructural characterization of nanocrystalline structures.

Keywords: Hydrothermal synthesis, post-annealing, doping concentration, Rietveld Refinement, lattice parameters, UV-Vis spectroscopy

Resumo

Nanoestruturas de óxido de metal, como o ZnO, têm um enorme impacto devido às suas propriedades únicas. Este trabalho concentra-se na síntese e caracterização de nanofios de ZnO. Em particular, o método de refinamento de Rietveld é implementado para realizar uma caracterização estrutural mais profunda das propriedades da nanoestrutura.

As propriedades morfológicas, estruturais e óticas dos nanofios não dopados e dopados (Ca, Eu, Ga) foram estudadas, variando a temperatura pós-recozimento (em nanofios não dopados) de 300 °C a 700 °C e a concentração de dopagem (em NWs dopados) de 1 a 5 % molar no microondas e no forno convencional.

A caracterização estrutural e morfológica das nanopartículas não dopadas por SEM mostrou que a síntese por microondas promoveu a formação de nanofios de ZnO de wurtzite e estruturas semelhantes a flores, enquanto a síntese convencional formou nanofios mais dispersos. Em ambos os casos, foram observadas dimensões médias de 5 μm de comprimento e perto de 1 μm de diâmetro, com uma distribuição de tamanho muito grande.

A síntese de nanotubos dopados revelou alterações morfológicas quando comparadas às não dopadas, e em particular para os nanotubos dopados com európio, foi formado $Eu(OH)_3$ ligado aos nanotubos de zinco. A espectroscopia UV-Vis também foi realizada para determinar a diferença no hiato energético. Observaram-se diferenças entre os nanofios de ZnO não dopados e dopados e entre os nanofios de ZnO não recozidos e os recozidos com valores de hiato energético entre 3.1 e 3.2 eV, como também relatado na literatura.

O método de Refinamento de Rietveld foi implementado nesses nanofios para estudar a evolução da estrutura cristalina dos mesmos. Os parâmetros da rede foram determinados e os resultados mostraram uma diminuição na proporção com o aumento da temperatura de recozimento nos nanofios não dopadas. No entanto, a tendência geral não segue um comportamento padrão nos nanofios de ZnO dopados. Não foram encontradas grandes diferenças na comparação entre microondas e síntese convencional no material dopado. Um protocolo para o refinamento de Rietveld foi desenvolvido como uma ferramenta para uma caracterização microestrutural mais profunda das estruturas nanocristalinas.

Palavras-Chave: Síntese Hidrotermal, pós-recozimento, Concentração de dopante, Refinamento de Rietveld, parâmetros de rede, espectroscopia UV-VIS

Contents

List of Figures

List of Tables

Symbols

mol%	Percentage by mol
E_g	Optical Band Gap
α	Linear Absorption Coefficient
h	Planck Constant
λ	Wavelength
ν	Frequency of Vibration
A	Proportionality Constant
m	Value of the Optical Band Gap Transition
τ	Size of the Crystallite
K	Scherrer Constant
β	Full Width at Half Maximum of the Diffraction Peak
θ	Bragg Angle of the Diffraction Peak
σ	Rietveld Fitting

Acronyms

IPA	Isopropanol
RT	Room Temperature
MW	Microwave
NW	Nanowire
SEM	Scanning Electron Microscopy
UV	Ultraviolet
VIS	Visible
NIR	Near Infrared Radiation
XRD	X-Ray Diffraction
CO	Conventional Oven

Objectives

The main purpose of this work is the structural and morphological characterization of zinc oxide (ZnO) nanowires synthetized by solvothermal methods using conventional and microwave ovens, to be used in optoelectronic devices. The nanowires are to be compared according to the type of heating step (conventional or microwave oven), post-annealing temperature (from 300° to 700°C), doping agent (calcium/europium/gallium) and dopant concentration (1 mol% to 5 mol%). This comparison is to be conducted by different characterization techniques as morphological (SEM), structural (XRD) and optical (UV-VIS spectroscopy).

In particular Rietveld Refinement method will be applied to study the crystallinity of ZnO, which is a method that allows to fit XRD data and extract the structural parameters of the crystal lattice from a partial or complete ab initio structure solution, such as unit cell dimensions, phase quantities, crystallite sizes/shapes, atomic coordinates/bond lengths, micro strain in crystal lattice, texture, and vacancies.

Motivation

ZnO is one of the most promising and studied semiconductor in optoelectronics. The study of its properties at the micro and nanoscale in nanostructures plays a very important role due to the ever-growing relevance that this material is getting in the semiconductor´s research and industry world. ZnO material has interesting physical properties like a large exciton binding energy, high electron mobility, high thermal conductivity and his wide and direct band gap [1]. These promising and versatile nanostructures can be synthetized in a wide range of forms, for instance, nanowires with a variety of applications such as UV sensors [2], biosensors , cosmetics, storage [3], optoelectronic devices, displays, among others [4].

Its importance is also enhanced by its synthesis, which has easier and greener processes and by its abundance being a non-toxic, biodegradable and biocompatible material.

Hence, studying single crystals structures of ZnO is essential to understanding the material and its properties. Since those structures are very small at a nanoscale, it’s very difficult to study them, so if we could characterize those single crystals at microscale, it would be an improvement for structural and electrical characterizations. The aim of this work is the synthesis of nanowires and, by means of post-annealing and doping, characterize them structurally using Rietveld Refinement method.

CHAPTER 1

1. Introduction

1.1. ZnO nanostructures: general properties and applications

Nowadays nanotechnology as seen many powerful advancements in numerous fields of science by means of working with materials and devices at a nanoscale using different advanced techniques. These nanostructures are defined by having a size between 1-100 nm and in general, possess three different morphologies: zero-dimensional (0D), one dimensional (1D), and two-dimensional (2D) nanostructures, all of which in the last few years have been a common material for the development of new cutting-edge technologies in energy storage, data storage, optics, medicine, biology, microelectronics and communications as a result of having exceptional magnetic, optical and electrical properties [5]–[7].

Amongst today´s world most used materials, metal oxides nanostructures made a huge impact on society due to their unique properties and versatile functionalities. Many metal oxides such as titanium dioxide (TiO_2), tungsten oxide (WO_3), tin oxides (SnO and SnO_2), copper oxides (CuO and CuO_2) and zinc oxide (ZnO) have been reported by being low-cost, nontoxic, abundant and reliable [8]–[13]. In particular ZnO, is an n-type semiconductor with unique properties such as a direct and wide band gap (E_g=3.37 eV) and high exciton binding energy (60 meV) at room temperature [9], [14]. Besides that, ZnO nanomaterials are highly stable and possess good mechanical strength (between 25 and 150 GPa), and high electron mobility (200 cm^2/V s) [15], [16].

ZnO has a wurtzite crystal structure (P63mc) at ambient conditions with a hexagonal unit cell as represented in Figure 1.1 and lattice parameters a = b = 0.3296 nm and c = 0.52065 nm.

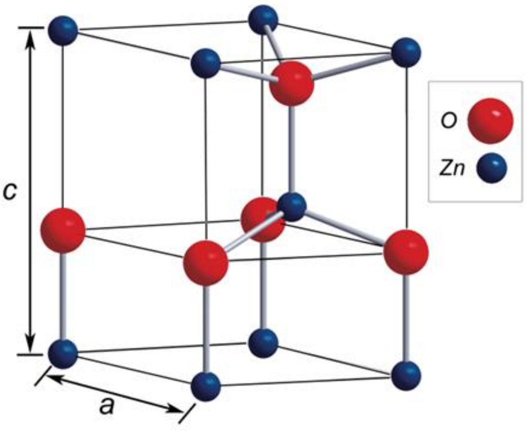

Figure 1.1: Scheme of the hexagonal wurtzite structure of ZnO [17]

This structure consists of alternating planes composed of tetrahedrally coordinated O_{2-} and Zn^{2+} stacked along the c-axis which results in an absence of a centre of symmetry in its wurtzite structure (Figure 1.1) along with large electromechanical coupling that contributes to strong piezoelectric and pyroelectric properties.

Due to such remarkable properties, ZnO can work in different areas of study such as from thin film transistors to piezoelectric devices and biomedical applications [9], [18], [19].

1.2. ZnO synthesis methods

There are several chemical, electrochemical and physical techniques used to prepare ZnO nanostructures with different morphologies. Solvothermal and hydrothermal synthesis are some examples of techniques that play a role on the different optoelectronic and electrical properties of the nanostructures as well as different solvents that can change the crystal morphology [20]–[22].

Because of today´s societal challenges, where the use of nanodevices and nano systems are essential for sustainability, new reliable and low-cost strategies are required to generate systems which can be appropriate for the variety of nanoelectronics and biological applications.

In a wide-ranging way, the classification of different types of synthesis can be divided as solution state synthesis and gas state synthesis. As for the first one, it represents all methods in which a liquid environment is present for the growing process, commonly called solvothermal process or hydrothermal process if it is in the presence of an aqueous solution [23]–[25].

As for the gas state synthesis, these methods can be characterized by using a gaseous environment inside a reaction chamber and require high temperatures (ranging from 500 °C to 1500 °C), being a disadvantage when it comes to the usage. This approach includes various techniques such as physical vapour deposition, chemical vapour deposition, vapour phase transport, metal organic chemical vapour deposition, thermal oxidation and condensation of pure Zn and microwave assisted thermal decomposition [25]–[28].

Considering the solution-based synthesis, the most used method is the solvothermal growth from a zinc acetate hydrate precursor, which is the chosen route in this work. This method of solvothermal growth can either be applied using a conventional or microwave oven [9], [29]. As comparing both, it comes out some essential characteristics which differentiate one another. Microwave oven due to his ability of produce nanostructures in just a few minutes became more popular than conventional oven [30]–[32]. Likewise, microwave oven can grow nanostructures with greater uniformity and less thermal gradient effect problems, which can be found on conventional oven due to his convection type of heating.

However, with a faster synthesis some problems arise. As a result of a faster synthesis produced by localized heating of the molecules in solution, defects begin to appear in the nanostructures, as well as different morphologies, shapes and sizes with the change of the microwave power, time and temperature [30]–[32].

1.3. **Doped ZnO nanostructures**

ZnO nanostructures may have very different properties that can be tuned by the synthesis parameters such as time, temperature, solvents, etc. Its electrical and structural properties are highly dependent of the defect density. By doping, different properties may arise as will be seen further [23], [33]–[38].

The efficiency of doping elements like Al, Ga, In, Cu, Sb, etc in ZnO is strongly influenced by the synthesis method depending also on parameters such as the dopant electronegativity and ionic radius [34], [39]. For instance, as reported in [40], that gallium is a very promising metal as a dopant, since it has a similar ionic radius compared to Zn resulting in a substitution without any lattice distortion leading to a stress-free ZnO:Ga material [41]. Another example of how the photocatalytic properties change is Fe and Cu, which produce lattice defects that influence the material performance. Not only optical and morphological properties can be altered but also physical properties can change as well using, for instance, Ni and In as a dopant having advantages in both environment and industrial applications. This capacity combined with a facile route of synthesis presents distinct advantages such has low cost, homogeneity on the molecular level due to the mixing of liquid precursors, excellent composition control and lower crystallization temperature [42]. The length to diameter ratio (aspect ratio) is another characteristic to consider, which can be changed by doping. This value can be less than 10 for nanorods and more than 10 for nanowires, as expected in [43], although the ratio is very debated in science community.

The present work is devoted to find the effects of the doping of ZnO nanowires with different dopant agents on the structural and optical properties of the nanostructures. Different dopants (Ga, Ca and Eu) with different atomic radius will be studied having different doping levels.

1.4. **Structural Characterization of ZnO nanostructures by Rietveld Method**

ZnO nanostructures can be characterized using many different techniques such as Scanning Electron Microscopy (SEM), Transmission Electron Microscopy (TEM), X-ray diffraction (XRD), X-ray photoelectron spectroscopy (XPS) and spectrophotometry among others.

Regarding the morphological characterization, SEM can be an excellent tool as it gives the possibility to see different sizes, shapes and morphologies of the doped and undoped ZnO nanostructures [44]. As for structural characterization, XRD measurements can be performed. The hydrothermally growth of ZnO nanostructures exhibit hexagonal wurtzite structure. This is shown by the analysis of different diffractograms for different ZnO structures grown through hydrothermal methods which peaks could be indexed according to JCPDS card No. 79-2205 [45]–[47]. An example of this result is shown in Figure 1.2.

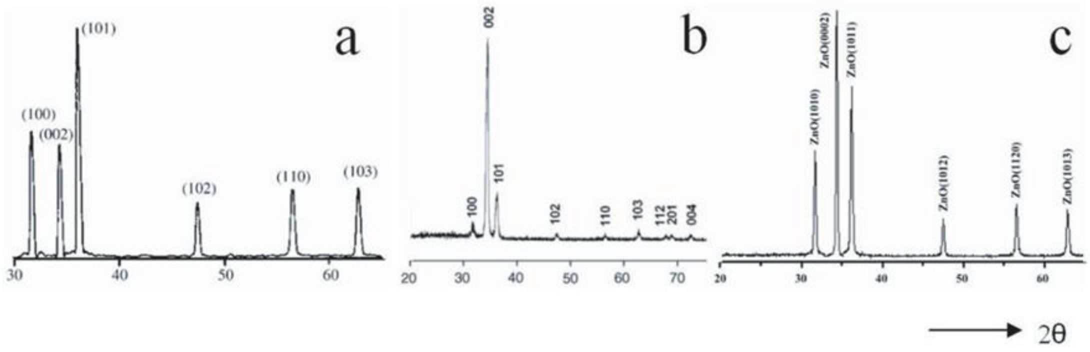

Figure 1.2: Typical x-ray diffraction (XRD) patterns for different ZnO nanostructures prepared using hydrothermal methods (a) nanoparticles, (b) nanowires and (c) nanoflowers [48].

Another important aspect to analyse the internal structure of ZnO nanostructures are the lattice parameters. The Rietveld method, as proposed by Hugo M. Rietveld, is one powerful technique to get structural information of nanocrystalline materials. This fits a calculated profile (including all structural and instrumental parameters) to experimental data by using a non-linear least squares method, and requires the many free parameters including peak shape, unit cell dimensions and coordinates of all atoms in the crystal structure [49]–[51].

It is possible to determine the accuracy of a crystal structure model by fitting a profile to a 1D plot of observed intensity vs diffraction angle. It is important to remember that Rietveld refinement requires a crystal structure model and offers no way to come up with such a model on its own. However, it can be used to find structural details missing from a partial or complete ab initio structure solution, such as unit cell dimensions, phase quantities, crystallite sizes/shapes, atomic coordinates/bond lengths, micro strain in crystal lattice, texture, and vacancies. The successful outcome of the refinement is directly related to the quality of the data, the quality of the model (including initial approximations), and the experience of the user [52], [53].

As for ZnO material, due to the three types of fastest-growth directions — <0001>, <01$\bar{1}$0> and <2$\bar{1}\bar{1}$0> — as well as the ± (0001) polar-surface-induced phenomena it is a versatile functional material that has a diverse group of growth morphologies and understanding the fundamental physical properties is crucial to the rational design of functional devices which requires detailed study of its structural properties [54]–[57]. In the present study, effects of doping with different elements at different mol% and annealing at high temperatures on lattice parameters will be studied.

CHAPTER 2

2. Methods and Materials

2.1. **ZnO Synthesis**

Although considering a solvothermal growth assisted by microwave and conventional irradiation, the ZnO (Zinc Oxide) nanostructures have been synthetized from the precursors zinc acetate dihydrate ($Zn (CH_3COO)_2{\cdot}2H_2O$; 98 to 101.0 %, CAS: 5970−45−6) from Alfa Aesar and sodium hydroxide (NaOH; CAS: 1310−73−2) from Eka. Deionized water and 2-ethoxyethanol ($C_4H_{10}O_2$; CAS: 110-80-5) from Honeywell, were the solvents used.

It was used surfactant, sodium lauryl sulphate ($NaC_{12}H_{25}SO_4$; 95 %, CAS: 151-21-3) from Scharlau to stabilize the nanostructures, prevent the development of agglomerates and to help assist with the length growth of the nanowires.

The preparation was made by dissolving the zinc acetate solution with molar concentration of 0.45 M at constant stirring, $Zn (CH_3COO)_2{\cdot}2H_2O$ in deionized water and adding NaOH to reach a molar concentration of 8 M of solution. This produces a transparent solution of $Zn (OH)_4^{-2}$ (solution A).

It was prepared a surfactant solution (solution B) by dissolving $NaC_{12}H_{25}SO_4$ in deionized water with a final molar concentration of 1.04 mM. The chemical reactions for the ZnO nanowires synthesis from Zn (II) acetate can be described as follow [9]:

$$ZnO(CH_3COO)_2 \cdot 2H_2O + 2NaOH \rightarrow Zn(OH)_2 + 2CH_3COONa + 2H_2O \tag{1}$$

$$Zn(OH)_2 + 2H_2O \rightarrow Zn(OH)_4^{2-} + 2H^+ \tag{2}$$

$$Zn(OH)_4^{2-} \rightarrow ZnO + H_2O + 2OH^- \tag{3}$$

To synthetize ZnO nanostructures it was used a microwave and an oven. The first one was helped by the usage of 50 ml Teflon vessels in which 10 ml of 2-ethoxyethanol was added with 5ml of solution B and 2 ml of solution A. The vessels were loaded into CEM Mars One microwave, with capacity for 12 vessels in which 3 vessels were used with the following microwave parameters of 110 °C of temperature, 600 W of power and 30 min of synthesis time (with heating ramp time of 7 min), already optimized for this reaction. When the synthesis is finished, the vessels were allowed to cooldown at room temperature.

As for convention oven a similar process was conducted. The vessels used were also Teflon, with a capacity of 17 ml, which were placed in a stainless-steel autoclave and loaded into a Heraeus furnace from Thermo Scientific. In each vessel was added 10 ml of deionized water, 5 ml of solution B and 2 ml of solution A. The oven parameters were 80 °C of temperature (with a heating ramp rate of 200 °C/h) and 24 h of synthesis time.

After either microwave or oven assisted synthesis was complete, a white precipitate was obtained. This precipitate was then washed with deionized water alternated with 2-isopropanol (IPA) and centrifuged at 4000 rpm for 3 min at least 3 times each. The powders were set to dry at room temperature for at least 72 h.

2.2. **Doped ZnO Nanostructures**

For doping the nanowires it must be considered the procedure in the section 2.1 where dopants as calcium ($(CH_3COO)_2Ca\cdot xH_2O$; 99.99 %, CAS: 62-54-4) from Sigma-Aldrich, europium ($Eu(NO_3)_3\cdot 5H_2O$; 99.9 %, CAS: 63026-01-7) from Sigma-Aldrich and gallium ($Ga(NO_3)_3\cdot xH_2O$; 99.9 %, CAS: 69365-72-6) from Sigma-Aldrich were set in the reaction varying the concentration percentage between 1 mol% and 5 mol%. These dopants were introduced before the adding of NaOH in the solution A of section 2.1.

2.3. **Nanowires dispersion and deposition on glass substrates**

Considering future characterization of ZnO nanowires, a dispersion has been made in IPA (isopropanol) with concentration of 1 mg/ml. Afterwards, the dispersion was placed in ultrasonic bath for 15 min to prevent nanowire aggregations. The next step consisted in spin-coating the dispersed solution on glass and silicon substrates (2.5 x 2.5 cm^2) using a velocity 3000 rpm for 30 s. To evaporate IPA, the substrates were heated on a hotplate at 60 °C.

2.4. **Nanowire annealing**

For further characterization the powders and substrates were annealed in a Nabertherm L030K1BN L311 B170 Muffle Furnace at different annealing temperatures between 300 °C and 700 °C. A heating rate of 5 °C/min was used in all annealings, and the samples were kept at the annealing temperature for 2 h before cooldown.

2.5. **Characterization Techniques**

For the morphology analysis, the experimental study was conducted in the Hitachi Tabletop Microscope TM3030 and on Carl Zeiss AURIGA Crossbeam workstation instrument.

For the optical band gap analysis, the measurements were performed with the use of a Spectrometer UV-Vis-NIR – Perkin Elmer Lambda 950. Those measurements have been carried out from 200 nm to 800 nm, with a scanning step size of 1 nm.

The structural and crystallite size analysis was determined using a PANalytical Xpert PRO X-ray diffractometer, with a monochromatic CuKα radiation source (wavelength 1.540598 Å). XRD measurements have been carried out from 20° to 100° (2θ), with a scanning step size of 0.016°. The data were then analysed by Rietveld Refinement using Gsas II – Crystallography Data Analysis Software [58].

CHAPTER 3

3. Results and Discussion

3.1. **Undoped ZnO nanowires**

In this section the results concerning the synthesis of ZnO nanostructures by microwave and conventional oven are presented and discussed. Annealings (from 300 to 700 °C) were also performed and the effect on the structural, morphological and optical properties is discussed.

3.1.1. Synthesis Route – Microwave *Vs* Conventional

As previously discussed, two solvothermal synthesis routes were performed during this work using the same zinc precursors and reagents but changing the temperature and pressure step, using either an autoclave irradiated in a microwave oven or using a conventional oven. The chosen parameters were optimized for each route in previous work [59].

As it can be seen in Figure 3.1, both routes lead to the production of ZnO nanowires with wurtzite structure although some changes in morphology were also detected. In fact, the synthesis assisted by MW lead to the presence of more aggregated nanostructures (Figure 3.1a) while the conventional oven (CO) route was characterized by more dispersed NWs, that when aggregated form spikes-like nanostructure (Figure 3.1b).

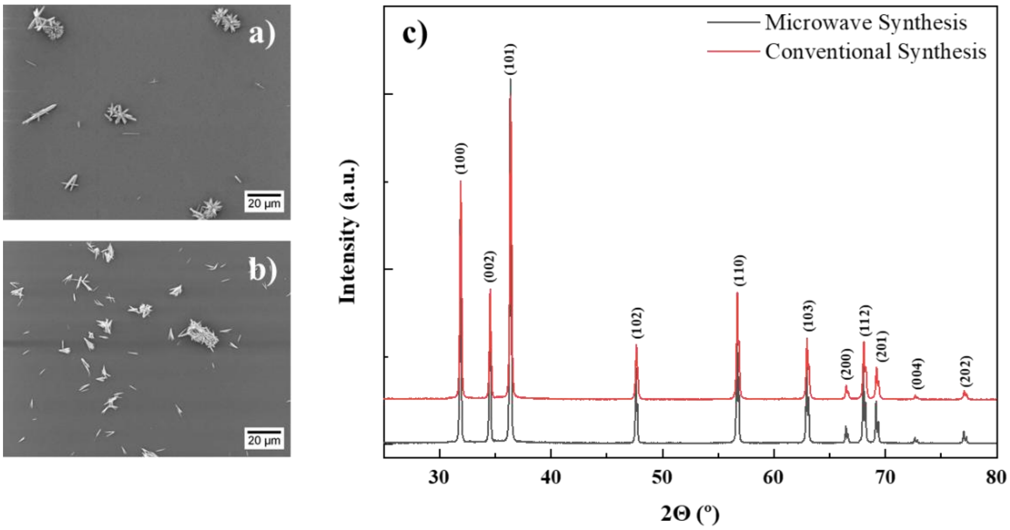

Figure 3.1: SEM images of nanowires produced by microwave synthesis (a) and by conventional synthesis (b). XRD diffractograms of ZnO nanostructures produced by microwave synthesis and conventional synthesis (c).

XRD allowed to confirm the ZnO wurtzite structure and no other phase was identified on both syntheses (Figure 3.1c). The first 3 peaks between 30° and 40° which represent the diffraction planes (100), (002) and (101) are the ones with more intensity. This diffraction planes combined with (102), (110), (103), and (112) diffraction planes represent the wurtzite-type hexagonal ZnO (space group P63mc), corresponding to ICDD 01-089-0511. Amongst the recognized peaks, (101) plane was the prominent one, which indicates the growth orientation on this plane.

A statistical and qualitative analysis was performed in these samples, considering SEM images with lower amplification to have an overall inspection of the homogeneity of the samples. In the analysis, the length of many (> than 100) isolated NWs were measured resulting in average length of 5 μm and 4 μm for the microwave and conventional synthesis respectively. This last synthesis method results in more isolated NWs.

Considering the aggregates of ZnO NWs, a similar statistical analysis was performed in order to obtain the apparent diameter of the aggregate. In microwave synthesis NWs form near spherical aggregates with an average apparent diameter of 7 μm. As for conventional synthesis these aggregates showed in a wide range of non-spherical forms with a broad size distribution.

In Figure 3.2, it is possible to observe some of the results (at different magnifications) for different ZnO nanostructure morphologies, which are dispersed and deposited in silicon (as described in Methods and Materials, chapter 2).

Through the analysis of the SEM images, it is possible to determine that from the microwave synthesis not only nanowires can be obtained, but also flower-like structures with hexagonal flat tops as also reported in [30], [60], [61]. This structure formation can be related with the Ostwald ripening in which the nanowires combine to form bigger structures (larger crystals) in order to reduce the overall interfacial energy of the system. The larger crystals in this process are more energetically favoured than smaller ones [9], [30]. As a consequence of a faster production of nanowires by microwave synthesis, flower-like structures are more likely to appear (Figure 3.2(a)).

A lot of parameters influence the way crystals grow and each solvent has its own way of interaction with conventional and microwave irradiation. This difference can cause changes in temperature and pressure inside the Teflon vessels which originates morphology changes.

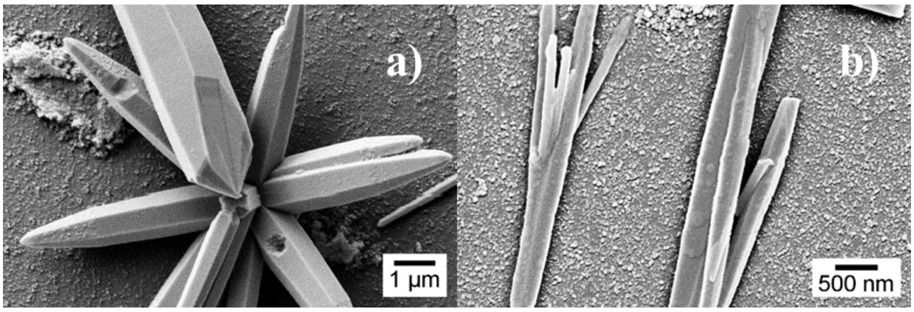

Figure 3.2: SEM images of nanostructures produced by microwave synthesis (a) and by conventional synthesis (b).

For determining the crystallite size of ZnO nanowires and find a connection between two types of synthesis, Scherrer´s equation was used (equation 4).

$$\tau = \frac{K\lambda}{\beta\cos\theta}, \tag{4}$$

where τ is the size of the crystallite, K is a numerical constant (Scherrer constant) equal to 0.9 (for nanoparticles), λ is the wavelength of the incident x-rays, β the full width at half maximum of the diffraction peak, and θ is the Bragg angle of the diffraction peak.

As noticeable in Table 3.1, the crystallite size in microwave synthesis is bigger than in conventional synthesis. This happens because it was used different types of heating which influences directly the way the crystal growth (Oswald Ripening) and interact with each other having a big impact on this evolution.

3.1.2. ZnO annealed Nanowires

In order to characterize the structure and to be sure about the material that was synthetized, an XRD analysis was performed for each annealed temperature condition. A few examples of XRD diffractograms produced by microwave oven and SEM images of annealed nanostructures are shown in Figure 3.3, as well as a graphic with different crystallite sizes for each annealed temperature produced by microwave synthesis and conventional synthesis in Figure 3.4.

As can be seen in Figure 3.3, the annealing was made on both ZnO nanostructures formed by microwave (Figure 3.3(a)) and conventional synthesis (Figure 3.3(b)). It is observed that in the first one it begins to appear some holes and grooves on the structure of the nanoflowers which as a preference along the NWs, as can be seen in [62]. As for conventional synthesis, with the annealing, nanowires appear to become curved on the edges.

A statistical and qualitative analysis was performed in these post-annealed samples as well considering SEM images with lower amplification to have an overall inspection of the homogeneity of the samples. Same analysis as in section 3.1.1 was made for post-annealed nanostructures, and the length of isolated NWs were measured resulting in a decreasing from 5 to 4 μm for the microwave and 4 to 3 μm for conventional synthesis. However, a wide distribution of lengths is needed to take into account in both syntheses as well.

On both synthesis it's also possible to see a fusion of the nanowires by those edges. Neither annealing temperature changed considerable the general shape of nanowires produced by conventional synthesis nor by microwave synthesis.

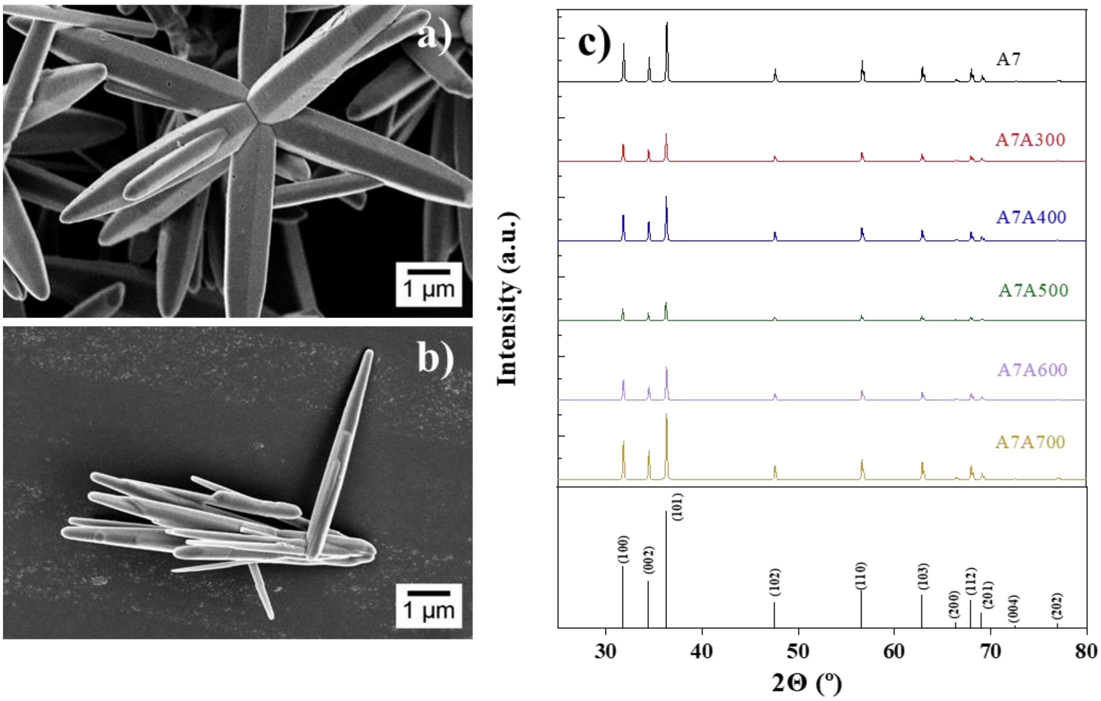

Figure 3.3: SEM images of nanowires produced by microwave synthesis (a) and by conventional synthesis (b) annealed at 700 °C. XRD diffractograms of ZnO nanostructures produced by microwave synthesis, annealed at different temperatures (c).

The XRD diffractograms of all the different annealing temperatures tested in this work for microwave (Figure 3.3) and conventional oven (Annex B – Figure 6.4), showed that ZnO was indeed the produced material. As happens in undoped ZnO nanowires those diffraction patterns represent the wurtzite-type hexagonal ZnO (space group P63mc), corresponding to ICDD 01-089-0511. Amongst the recognized peaks, (101) plane was the prominent one, which indicates the growth orientation on this plane.

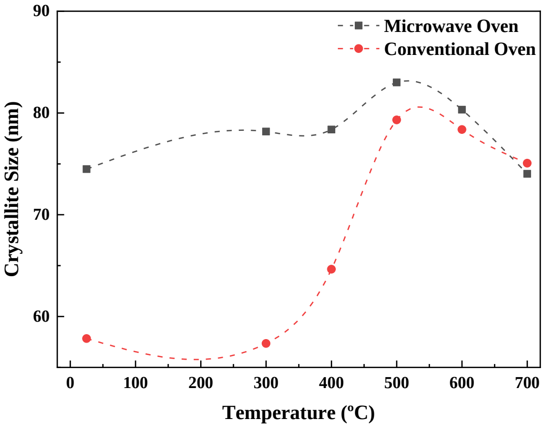

Figure 3.4: Average crystallite size of the 3 peaks with more intensity for different annealing temperatures for both microwave and conventional syntheses. The standart deviation values are to small to be represented.

For determining the crystallite size of ZnO nanowires and find a connection between different annealing temperatures, Scherrer´s equation was used (equation 4).

Table 3.1: Crystallite sizes calculated for microwave and conventional synthesis when annealing temperature is a variable.

	Miller Indices (hkl)	**Temperature (°C)**					
		25	**300**	**400**	**500**	**600**	**700**
Crystallite size (nm) Microwave synthesis	**100**	74.3	77.4	77.9	83.2	80.4	73.3
	002	74.5	78.3	78.4	82.2	80.3	74.1
	101	74.7	78.8	78.8	83.6	80.3	74.6
	Average	74.5 ± 0.2	78.2 ± 0.7	78.4 ± 0.5	83 ± 0.7	80.3 ± 0.1	74 ± 0.6
Crystallite size (nm) Conventional Synthesis	**100**	58.9	57.5	64.4	79.9	79.1	75.5
	002	57.7	57.3	64.7	79.3	78.3	75.0
	101	56.9	57.3	64.9	78.8	77.7	74.7
	Average	57.8 ± 1.0	57.4 ± 0.1	64.7 ± 0.2	79.3 ± 0.6	78.4 ± 0.7	75.1 ± 0.4

As seen in Table 3.1 and Figure 3.4, the crystallite size values tend to increase as the annealing temperature increases from 25 °C to 500 °C. This may be due to the fact that increasing of atomic mobility with the increase of annealing temperature, enhances the ability of atoms to find the most energetically favoured sites. Another explanation is that densities of vacancies, interstitials and dislocations of ZnO nanowires decrease with the increased annealing temperature [63], [64]. So, the annealing temperature can have an effect on ZnO nanostructures, although not having a clear linear evolution as expected.

3.1.3. Band Gap and Rietveld Refinement Method

With the UV-VIS spectroscopy it is possible to determine the ZnO NWs optical band gap (E_g). A study of the impact of the different conditions can be conducted regarding its effects in the spectrum of this type of characterization and its consequent optical band gap value. The raw data was given as the percentage of reflectance as a function of the light's wavelength. According to equation 5, it is possible to plot $(\alpha h\nu)^m$ against h/λ (the Tauc plot) as found in Figure 3.5, where α is the linear absorption coefficient of the material, m is a constant related to the type of optical transition (equal to 2 in this case, since we are dealing with a direct band gap transition), h/λ is the photon energy and A is the proportionality constant.

$$(\alpha h\nu)^m = A(h\nu - E_g) \tag{5}$$

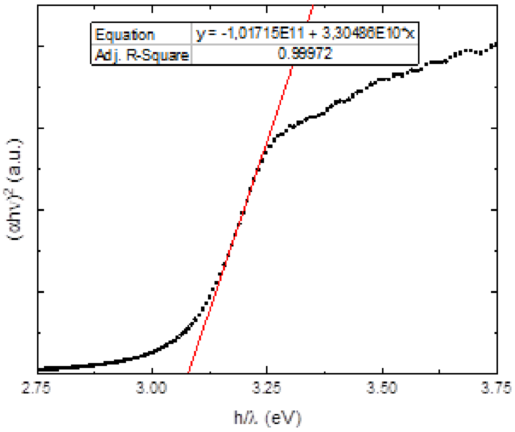

Figure 3.5: Tauc plot representing the process of the optical band gap calculation from the data of the UV-VIS spectrophotometry.

In Figure 3.5 was plotted a linear fit, which indicates that, when y = 0, it is possible to extract the value of the optical band gap. In Table 3.2 are the values of band gap calculated for different annealing temperatures.

From room temperature to 300 °C, band gap increases significantly. This change in band gap can be attributed to the increase of particle size [65] or to electron impurity scattering, as expected in [66]. Another explanation may be due to the fact that those minimal differences in band gap above 300 °C might be attributed to film stress alterations, crystallite size variations or changes in the film stoichiometry where the effect of O variations clarify the band gap shift [67].

All the variations in lattice parameters and band gap also happens to ZnO nanowires produced by conventional synthesis, which values variations are practically the same.

The XRD data of ZnO annealed at different temperatures were refined by Rietveld Refinement using the program GSAS software with the procedure in Annex C – Rietveld Refinement Procedure, and the extracted lattice parameters are given in Table 3.2 for microwave synthesis. The standard values for ZnO nanowires are given by COD ID 2300450 (a = b = 3.2493; c = 5.2057). In Figure 3.6, it's possible to see an example of an experimental and simulated pattern produced by microwave synthesis without annealing.

As it can be seen in Figure 3.7, the ratio (c/a) of lattice parameters varies with annealing temperature indicating the presence of strain in the lattice as expected by [68]. This ratio is decreasing with temperature, also representing a denser atomic packing of the atoms for higher annealing temperature [69].

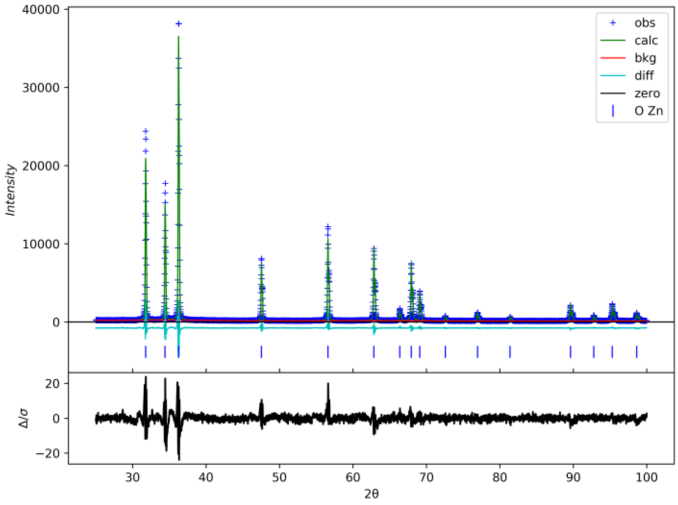

Figure 3.6: Example of an experimental and simulated diffraction pattern with Rietveld refinement using Gsas of ZnO nanowires produced by microwave sinthesys without annealing.

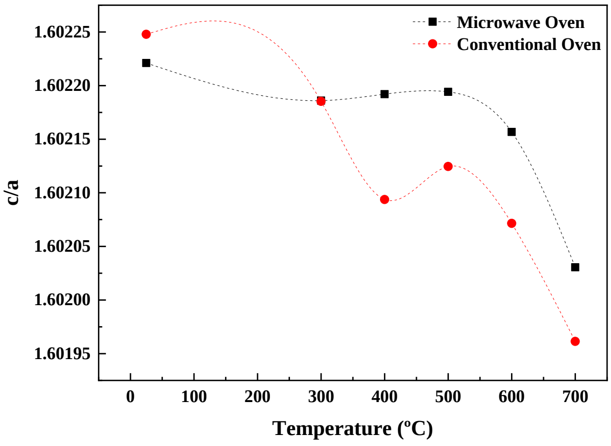

Figure 3.7: ratio of lattice parameters (c/a) for different anealling temperatures for both microwave and conventional synthesis.

Table 3.2: Rietveld Refinement parameters and band gap of ZnO nanowires annealed at different temperatures produced by microwave synthesis.

Temperature (°C)	***a=b*** (Å)	***c*** (Å)	***c/a***	***E_g (eV)***
25	3.24987	5.20701	1.60222	3.060
300	3.24883	5.20523	1.60218	3.161
400	3.24913	5.20573	1.60219	3.138
500	3.24867	5.20500	1.60219	3.132
600	3.24927	5.20584	1.60216	3.162
700	3.24937	5.20559	1.60203	3.161

As noticeable on Table 3.2, the overall values of lattice parameters decrease with temperature. ZnO nanoparticles have several defects such as oxygen vacancies, lattice disorders and dislocations. As a result of post-annealing, these defects are removed and the lattice contracts. Also lattice relaxation due to dangling bonds should be considered. The dangling bonds on ZnO surface interact with oxygen ions from the atmosphere and due to electrostatic attraction, lattice is slightly contracted.

3.2. **Doped ZnO Nanostructures**

In this section it was investigated the nanostructure of doped ZnO nanowires (doped from 1 to 5 mol%) produced by microwave oven and conventional oven and the effect on the structural, morphological and optical properties is discussed.

3.2.1. Calcium Doping

3.2.1.1. Structural and Morphological Characterization – SEM and XRD

In this subsection it was analysed the morphology of ZnO nanowires looking over at the synthesis parameters such as the type of heating stage and doping.

In Figure 3.8, it is possible to observe some of the results (at different magnifications) for different ZnO nanostructure morphologies synthetized and doped with different molar percentages (1 to 5 mol%) of calcium, which were dispersed and deposited in silicon (as described in Methods and Materials, chapter 2).

Through analysing the SEM images, it is possible to see that the morphology of calcium doped ZnO nanowires change with doping molar percentage. In Figure 3.8a, the covered nanowires, produced by conventional synthesis, appear to be aligned in the same direction with rugosities covering its surfaces. When doping was increased to 5 mol% (Figure 3.8b), the holes seems to disappear, the rugosities became less visible and the nanowire seem to be covered smoothly all over its surface. As for microwave synthesis (Annex A, Figure 6.1), same thing occurs in which the hexagonal shape of the nanowire (Figure 6.1a), is masked, changing it form to a less hexagonal one (Figure 6.1b).

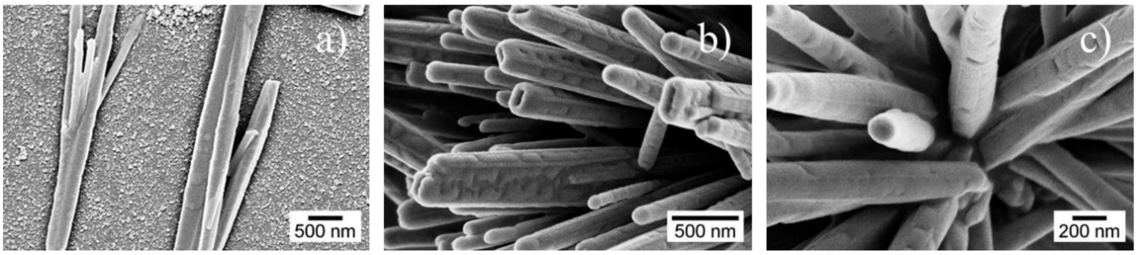

Figure 3.8: SEM images of nanostructures produced by conventional synthesis with 0 mol% (a), 1 mol% (b) and 5 mol% of calcium (c).

Effectively, the reaction of calcium with ZnO nanowires change his morphology. It's always needed to consider that non-controllable variables may change the final product of synthesis.

A few examples of XRD diffractograms produced by conventional synthesis are shown in Figure 3.9, as well as a magnification area of the diffraction pattern showing a reflection of another phase.

In all the different doping percentages tested in this study for microwave and conventional oven, the XRD reports confirmed that ZnO was indeed the produced material. The first 3 peaks between 30° and 40° which represents the diffraction planes (100), (002) and (101) are the ones with more intensity.

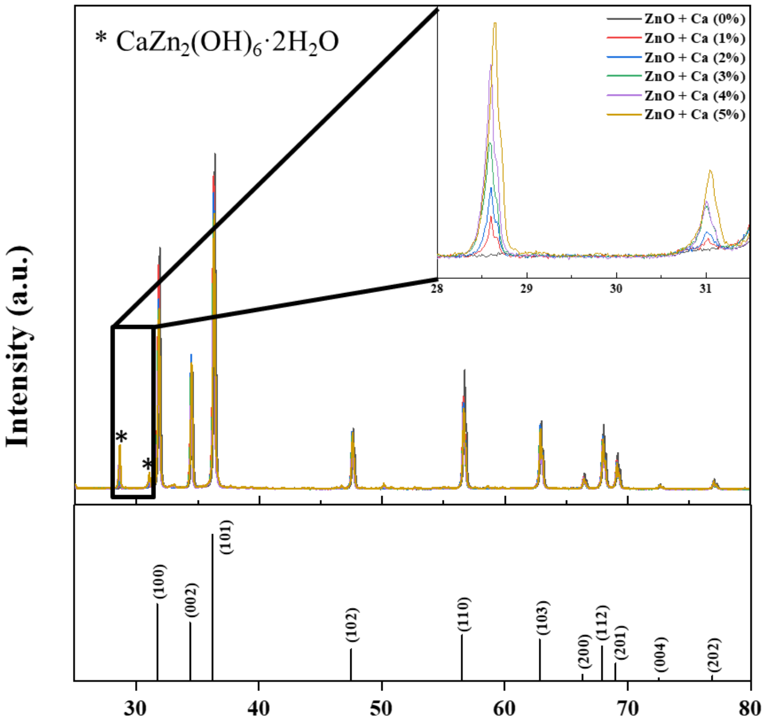

Figure 3.9: Example of XRD diffractograms of different calcium doping percentages produced by conventional synthesis. The inset shows a magnified area of the diffraction pattern of these samples in which the reflections of other phase were visible.

These diffraction planes combined with (102), (110), (103), and (112) diffraction planes represents the wurtzite-type hexagonal ZnO (space group P63mc), corresponding to ICDD 01-089-0511. Along the recognized peaks, (101) plane was the noticeable one, which indicates the growth orientation on this plane.

It is also shown the growth of a fourth more intense peak along the mol% of calcium doped ZnO between 25° and 30°, which occurrence may be due to a phase segregation associated with $CaZn_2(OH)_6\cdot 2H_2O$ phase, matching with ICDD 01-070-1561. The average crystallite size of the 3 more intense peaks, for each doping percentage, in both microwave and conventional synthesis, is presented on Figure 3.10.

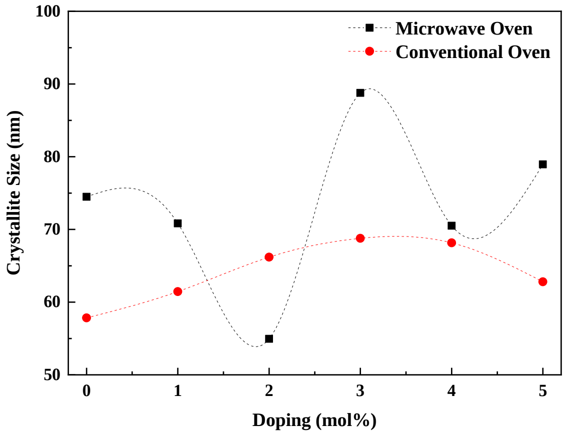

Figure 3.10: Average crystallite size of the 3 peaks with more intensity of calcium doped ZnO for both microwave and conventional synthesis. The standart deviation values are to small to be represented.

For determining the crystallite size of ZnO nanowires and find a connection between different mol% of calcium, Scherrer´s equation was used (equation 4). The Table 3.3 presents the determined values for both microwave and conventional synthesis.

Table 3.3: Crystallite sizes calculated for calcium doped ZnO produced by microwave and conventional synthesis when mol% doping is a variable.

	Miller Indices (hkl)	**Doping (mol%)**					
		0	**1**	**2**	**3**	**4**	**5**
Crystallite size (nm) Microwave synthesis	**100**	74.3	71.1	54.7	88.9	70.3	78.7
	002	74.5	70.8	55.0	88.8	70.5	79.0
	101	74.7	70.6	55.2	88.6	70.7	79.1
	average	74.5 ± 0.2	70.8 ± 0.2	54.9 ± 0.3	88.8 ± 0.2	70.5 ± 0.2	78.9 ± 0.2
Crystallite size (nm) Conventional Synthesis	**100**	58.9	61.8	66.5	68.6	67.9	63.0
	002	57.7	61.4	66.2	68.8	68.2	62.8
	101	56.9	61.1	65.9	68.9	68.4	62.7
	Average	57.8 ± 1.0	61.5 ± 0.4	66.2 ± 0.3	68.8 ± 0.2	68.2 ± 0.2	62.8 ± 0.2

It is noticeable from Table 3.3 and Figure 3.10 that in microwave synthesis the samples do not exhibit a homogeneous crystallite size distribution, which can be seen by the differences of those values. This can be explained by the shifting of 2θ of the diffraction planes towards lower values (Annex B - Figure 6.8) with the increase in mol% of dopant agent, which affects directly the crystallite sizes as well as the full width at half maximum and as a consequence the lattice parameters which it will be seen further [70]. In figure 3.11 is shown the shifting in 2θ of the most intense peak for conventional synthesis, corresponding to (101) diffraction plane.

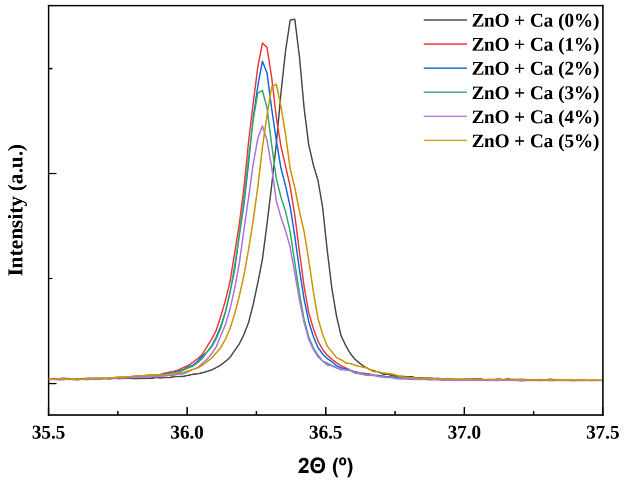

Figure 3.11: Zoom in on (101) difraction plane of XRD diffractograms of different calcium doping percentages produced by conventional synthesis.

Additionally, this behaviour may be attributed to local distortions of the wurtzite lattice caused by some residual stress inside the nanowires [70]. Same explanation can be given to conventional synthesis (Figure 3.11) , although a smaller variation of crystallite sizes are shown, compared with microwave synthesis and these values seem to slower increase when mol% is increased.

3.2.2. Europium Doping

3.2.2.1. Structural and Morphological Characterization – SEM and XRD

In this subsection it was analysed the morphology of ZnO nanowires, using europium as doping agent, looking over at the synthesis parameters such as the type of heating stage and doping.

In Figure 3.12, it is possible to observe some of the results (at different magnifications) for different ZnO nanostructure morphologies and doped with different molar percentages (1 to 5 mol%) of europium, which were dispersed and deposited in silicon (as described in Methods and Materials, chapter 2).

Through analysing the SEM images, it is possible to see that the morphology of europium doped ZnO nanowires changes with doping molar percentage of europium. In Figure 3.12a, the nanowires have a well-defined hexagonal shape with some agglomerates around them and a pencil-like shape on the edges. As for Figure 3.12b, when molar percentage was increased to 5 mol%, the structure remains nearly the same with these agglomerates increasing in quantity and appearing at the edges of those nanowires. As for conventional synthesis, a similar thing happens as it can be seen in Annex A, Figure 6.2a and Figure 6.2b.

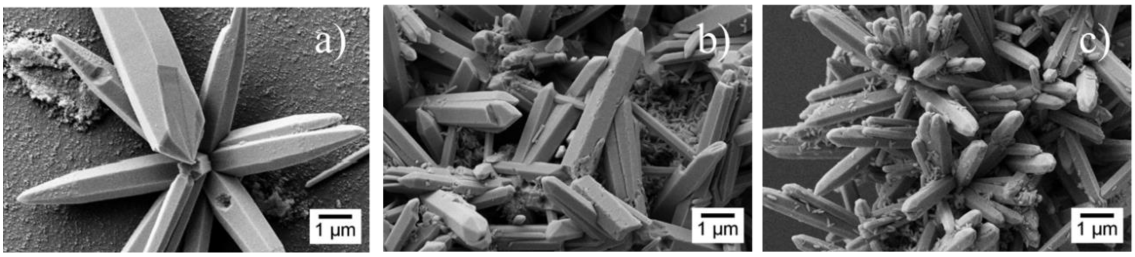

Figure 3.12: SEM images of nanostructures produced by microwave synthesis with 0 mol% (a), 1 mol% (b) and 5 mol% of europium (c).

A few examples of XRD diffractograms produced by microwave oven are shown in Figure 3.13 as well as a magnification area of the diffraction pattern showing a reflection of secondary phase associated with Eu(OH)$_3$ and occurring at diffraction angles that agrees well with ICDD card number 01-083-2305. The XRD reports shows the presence of ZnO as well. The first 3 peaks between 30° and 40° which represent the diffraction planes (100), (002) and (101) are the ones with more intensity. This diffraction planes combined with (102), (110), (103), and (112) diffraction planes represent the wurtzite-type hexagonal ZnO (space group P63mc), corresponding to ICDD 01-089-0511.

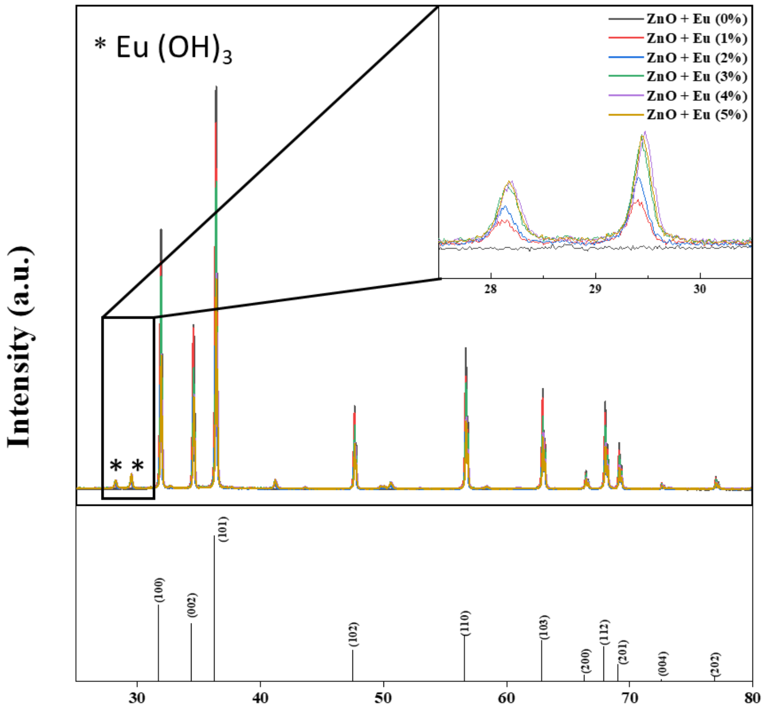

Figure 3.13: Example of XRD diffractograms of different europium doping percentages produced by microwave synthesis. The inset shows magnified area of the diffraction pattern of these samples in which the reflections of secondary phases were visible.

Amongst the recognized peaks, (101) plane was the noticeable one, which indicates the growth orientation on this plane. As for conventional synthesis same investigation was performed, reaching the same results (Annex B - Figure 6.6).

With the increase in mol% of europium, the intensity of diffraction peaks of secondary phases (Eu $(OH)_3$) increased. An incomplete reaction on further addition of Eu^{3+} ions may be the root in which those ions segregate on the surface due to its bigger ionic radius comparatively to Zn^{2+} (Eu^{3+} ionic radius = 0.95 Ǻ and Zn^{2+} ionic radius = 0.74 Ǻ). Additionally, the small shift of the diffraction peaks can be happening because of the small amount of Eu^{3+} that were introduced into Zn^{2+} interstitial sites [71]. The average crystallite size of them for each doping percentage in both microwave and conventional synthesis is revealed on Figure 3.14.

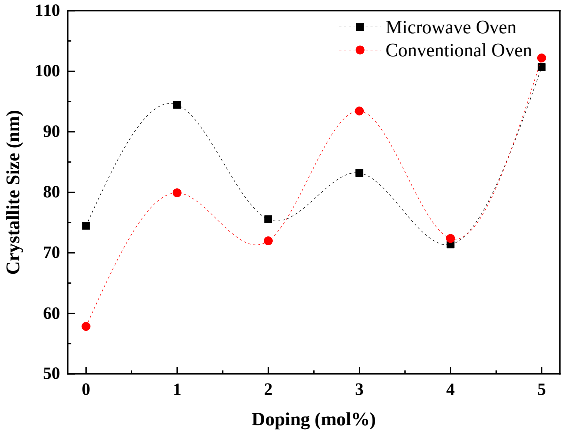

Figure 3.14: Average crystallite size of the 3 peaks with more intensity of europium doped ZnO for both microwave and conventional synthesis. The standart deviation values are to small to be represented.

For determining the crystallite size of ZnO nanowires and find a connection between different mol% of europium, Scherrer´s equation was used (equation 4). The Table 3.4 exposes the determined values for both microwave and conventional synthesis.

Table 3.4: Crystallite sizes calculated for europium doped ZnO produced by microwave and conventional synthesis when mol% doping is a variable.

	Miller Indices (hkl)	**Doping (mol%)**					
		0	**1**	**2**	**3**	**4**	**5**
Crystallite size (nm) Microwave synthesis	**100**	74.3	95.0	75.5	83.0	71.0	90.9
	002	74.5	94.4	75.6	83.2	71.4	106.1
	101	74.7	94.0	75.6	83.4	71.7	105.0
	Average	74.5 ± 0.2	94.5 ± 0.5	75.5 ± 0.1	83.2 ± 0.2	71.4 ± 0.3	100.7 ± 8.5
Crystallite size (nm) Conventional Synthesis	**100**	58.9	80.5	71.6	94.1	71.9	100.9
	002	57.7	79.8	72.0	93.3	72.4	102.3
	101	56.9	79.4	72.3	92.8	72.7	103.4
	Average	57.8 ± 1.0	79.9 ± 0.6	72.0 ± 0.3	93.4 ± 0.7	72.4 ± 0.4	102.2 ± 1.3

As can be seen in Table 3.4 and Figure 3.14 that crystallite size values doesn´t have a linear evolution with mol% of europium. Differences in the 2θ of the diffraction planes influence directly the value of the crystallite size. Having small shifts, as seen in Figure 3.15, as well as differences in full width at half maximum on the 3 most relevant peaks result in variations of the crystallite size can be an indication of the replacement of Zn^{2+} by the Eu^{3+} in the lattice. Additionally, as the Eu^{3+} have a larger ionic radius (0.95 Å) than Zn^{2+}(0.74 Å), this can cause a unit cell volume expansion on ZnO lattice [72].

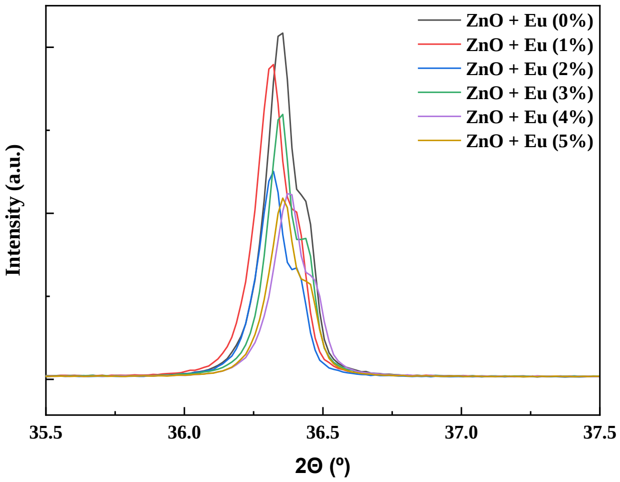

Figure 3.15: Zoom in on (101) difraction plane of XRD diffractograms of different europium doping percentages produced by microwave synthesis.

The peak shifting mixed with non-linear changes in crystallite size values can be attributed to lattice distortions, strain in the lattice or lattice mismatching [73]. Overall, the evolution of the crystallite sizes in both microwave and conventional synthesis resemble nearly the same.

3.2.3. Gallium Doping

3.2.3.1. Structural and Morphological Characterization – SEM and XRD

In this subsection it was analysed the morphology and ZnO nanowires looking over at the synthesis parameters such as the type of heating stage and doping.

In Figure 3.16, it is possible to observe some of the outcomes (at different magnifications) for different ZnO nanostructure morphologies synthetized and doped with different molar percentages (1 to 5 mol%) of gallium, which were dispersed and deposited in silicon (as described in Methods and Materials, chapter 2).

Through examining the SEM images, it is possible to see that doping with gallium does not create a distinct difference in morphology and shape in comparison with pure ZnO (Figure

3.2a and b). It can be seen in Figure 3.16a that long ZnO nanowires produced by microwave synthesis tend to agglomerate into flower-like assembly with pencil-like edges. As for conventional synthesis, it is shown in Figure 6.3a and Figure 6.3b, long ZnO nanowires slimmer than those synthetized by microwave synthesis, with urchin-like structure and curved edges. However, in both syntheses, the increasing of mol% doesn´t affect the overall shape of the nanowires.

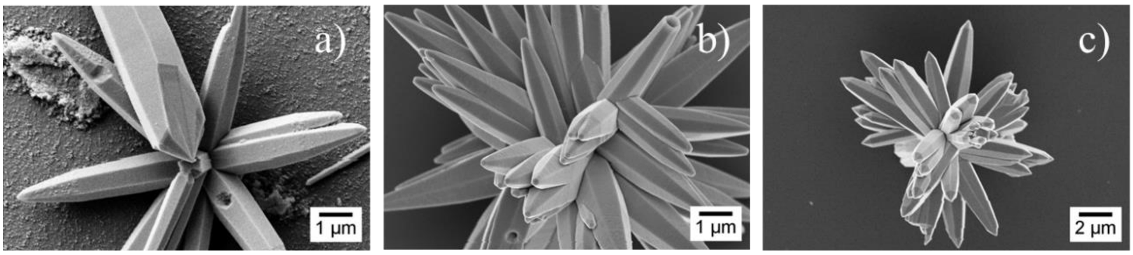

Figure 3.16: SEM images of nanostructures produced by microwave synthesis with 0 mol% (a), 1 mol% (b) and 5 mol% of gallium (c).

This retention in those attributes can be interesting when electronics and optoelectronic applications of ZnO-based semiconductors are the focus [74], as it is in this study.

XRD allowed to confirm the ZnO wurtzite structure and no other phase was identified on both syntheses. A few examples of XRD diffractograms produced by microwave oven are shown in Figure 3.17, as well as a graphic with different crystallite sizes for each doping molar percentage of gallium produced by microwave synthesis and conventional synthesis in Figure 3.18.

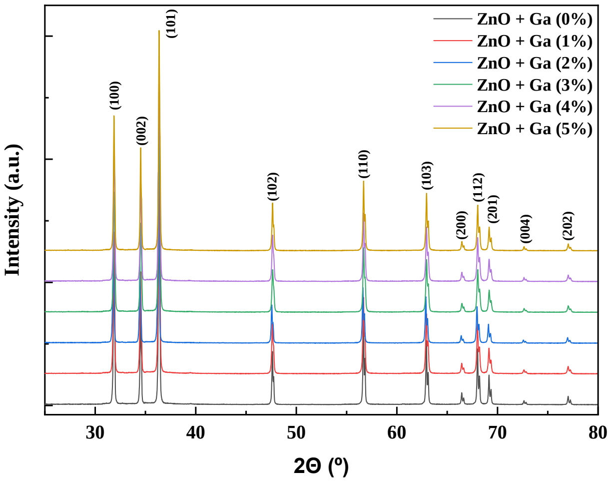

Figure 3.17: Example of XRD diffractograms of different gallium doping molar percentages produced by microwave synthesis.

As happens with ZnO annealed nanowires in subsection 3.1.2, the first 3 peaks between 30° and 40° which represent the diffraction planes (100), (002) and (101) are the ones with more intensity. This diffraction planes combined with (102), (110), (103), and (112) diffraction planes represent the wurtzite-type hexagonal ZnO (space group P63mc), corresponding to ICDD 01-

089-0511. Amongst the recognized peaks, (101) plane was the prominent one, which indicates the growth orientation on this plane.

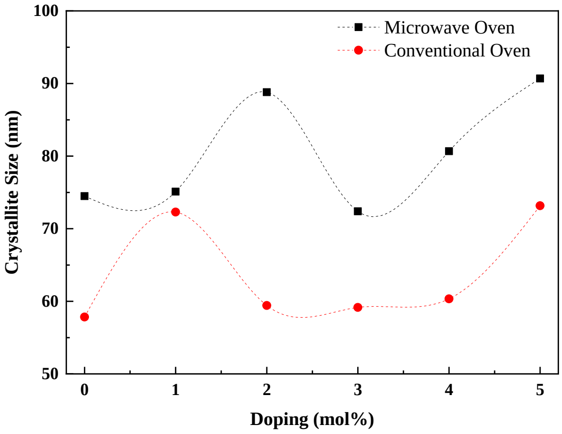

Figure 3.18: Average crystallite size of the 3 peaks with more intensity of gallium doped ZnO for both microwave and conventional synthesis. The standart deviation values are to small to be represented.

This reports are identical of those with pure ZnO (Figure 3.3, subsection 3.1.2) regardless of the incorporation of gallium in ZnO crystal with a small lattice distortion and crystallite size variation. Once more, Scherrer's equation was used to determine the crystallite sizes of those nanostructures, as can be seen in Table 3.5.

Table 3.5: Crystallite sizes calculated for gallium doped ZnO produced by microwave and conventional synthesis when mol% doping is a variable.

	Miller Indices (hkl)	**Doping (mol%)**					
		0	**1**	**2**	**3**	**4**	**5**
Crystallite size (nm) Microwave synthesis	**100**	74.3	75.3	90.5	73.0	81.4	92.1
	002	74.5	75.1	88.5	72.3	80.6	90.5
	101	74.7	75.0	87.4	71.9	80.0	89.5
	Average	74.5 ± 0.2	75.1 ± 0.2	88.8 ± 1.6	72.4 ± 0.5	80.7 ± 0.7	90.7 ± 1.3
Crystallite size (nm) Conventional Synthesis	**100**	58.9	72.7	60.5	60.2	60.7	73.7
	002	57.7	72.3	59.3	59.0	60.3	73.1
	101	56.9	71.9	58.5	58.3	60.0	72.7
	Average	57.8 ± 1.0	72.3 ± 0.4	59.4 ± 1.0	59.2 ± 0.9	60.3 ± 0.4	73.2 ± 0.5

According to Table 3.5 and Figure 3.18, the values of crystallite size increased from 0 to 2 mol% and from 3 to 5 mol%. This can be attributed to smaller radius of Ga^{3+} ion (61 Ǻ) compared to that of Zn^{2+} ion (74 Ǻ) in the host ZnO lattice, which contributes to the variation in the size of the unit cell, due to distortions of ZnO lattice and the saturation of Ga doping. Figure 3.19 shows a zoom in on (101) diffraction plane, in which is possible to see that when mol% increase, the peak is shifted towards both sides (low and high 2θ). This can be an indication of a variation in lattice spacing and consequently, differences in crystallite size which is attributed to the smaller radius of Ga^{3+}. Nevertheless, when there is a shift towards high 2θ, it can occur degradation of the crystal quality of the nanostructure, as expected in [75].

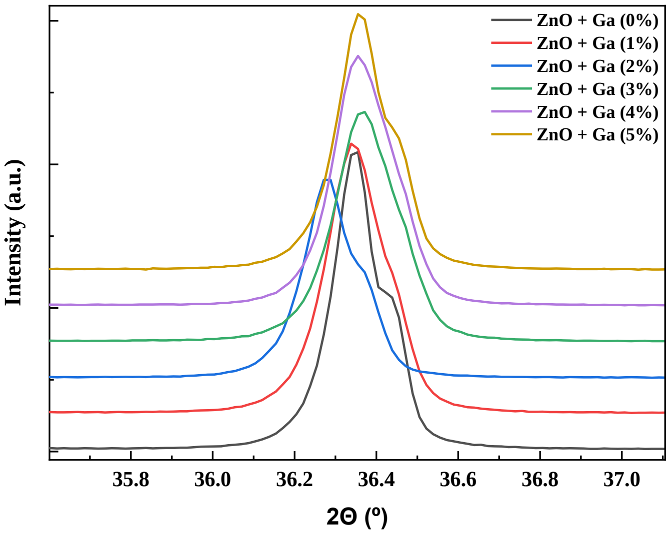

Figure 3.19: Zoom in on (101) difraction plane of XRD diffractograms of different gallium doping molar percentages produced by microwave synthesis.

In conventional synthesis an opposite shifting through lower 2θ, can be seen in Annex B - Figure 6.10, which is the result of a better quality of the present crystal. However, the values of crystallite size seem to vary less than in microwave synthesis, which apparently may be due to a differently type of synthesis that provides different temperature profiles to the material.

3.2.4. Rietveld Refinement

In this subsection its was analysed how the molar percentage of the dopant agent affects the lattice parameters.

The XRD data of ZnO doped with different percentages of calcium, europium and gallium were refined by Rietveld Refinement using the program GSAS software with the procedure in Annex C – Rietveld Refinement Procedure, and the extracted lattice parameters are given in Table 3.6 for microwave synthesis. The standard values for ZnO nanowires is given by COD ID 2300450 (a = b = 3.2493; c = 5.2057; V = 47.5984). In Figure 3.20, Figure 3.21 and Figure 3.22 is shown a graphic representing the evolution of lattice parameters of the ZnO nanowires produced by microwave and conventional synthesis throughout different doping molar percentages (1 to 5 mol%) and different types of doping agents (Ca, Eu, Ga).

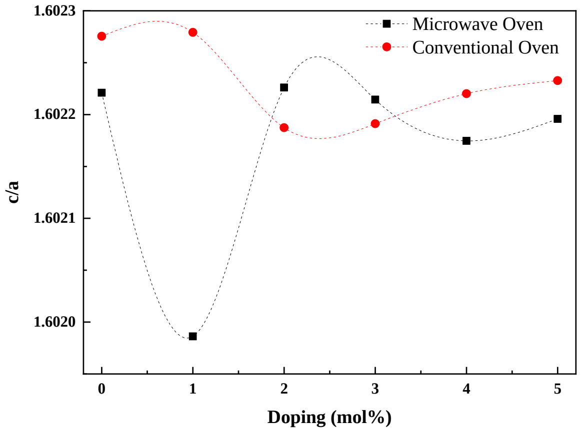

Figure 3.20: Ratio of lattice parameters (a and c) for different molar percentages of calcium for both microwave and conventional synthesis.

As noticeable on Figure 3.20, the increase of doping molar percentage leads to differences in the values of lattice parameters and an overall increase in unit cell parameter. This effect is expected in [76], because the ions of Ca^{2+} (100 Å) have bigger ionic radius than Zn^{2+} (74 Å) and then it suggests that those calcium ions replace the zinc in the lattice sites. Also, this fluctuations in the values may happen because of the appearance of a secondary phase, as can be seen in [77]. As for conventional synthesis, it is possible to see an overall smaller change in the ratio values, when compared with microwave synthesis. This may be attributed to less lattice distortions taking place in ZnO structure synthetized by conventional synthesis since the interaction between the ZnO material and the temperature profile provided in both syntheses is different.

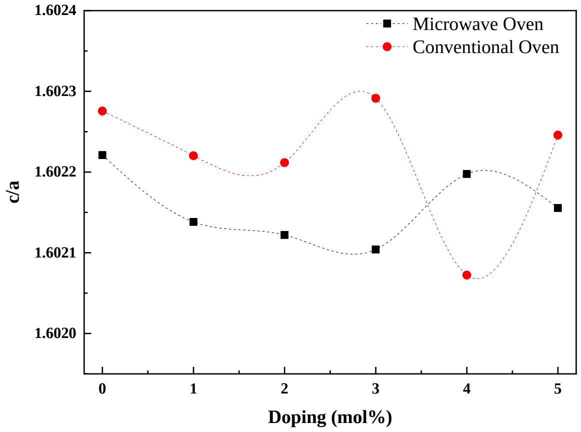

Figure 3.21: Ratio of lattice parameters (a and c) for different molar percentages of europium for both microwave and conventional synthesis.

As happened in calcium doped ZnO NWs, the ratio (c/a) of europium doped ZnO NWs varied throughout mol%. As seen in [78], the increase in lattice parameters may have is cause by the doping with bigger sized ions as Eu^{3+} (95 Å) compared with Zn^{2+} (74 Å). In this study the lattice parameters values of europium doped ZnO varied with different concentrations, around the undoped ZnO value (0 mol%), not having a specific linear evolution as could be expected.

Another explanation for this fact is the 2θ shifting around higher and lower values throughout mol% of dopant agent, which ultimately affects a and c parameters.

Figure 3.21 shows that these differences are more abrupt in conventional synthesis than in microwave synthesis, especially from 3 mol% to 5 mol%, where those changes are significantly more visible.

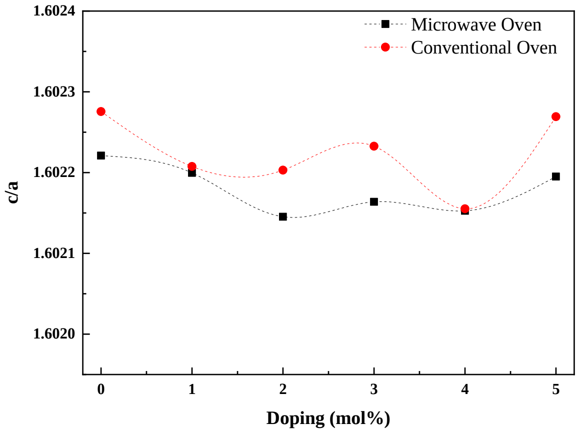

Figure 3.22: Ratio of lattice parameters (a and c) for different molar percentages of gallium for both microwave and conventional synthesis.

As visible in Figure 3.22 the increase of doping molar percentage leads to a general decrease in c/a values. This fact can be explained by wurtzite to rocksalt transformation in high pressure experiments where the behaviour might be explained by internal pressure produced by dopants, as expected in [79]. Accordingly, to Vegard´s law, a substitution by an atom with larger ionic radius, increases the lattice parameters a and b. The ionic radius of Ga^{3+} (61 Ǻ) is smaller than Zn^{2+} (74 Ǻ), and those values still increase. These changes in lattice parameters (a, b and c) cannot be answered by only taking ionic radius into account. Another explanation could be the relaxation of lattice parameters due to a decrease in internal attractive forces in the crystal [79] and by that justify the increase in values of lattice parameters a and c in this work. The small differences in c/a ratio from microwave to conventional synthesis allows to determine that their lattice behaviour is similar.

Table 3.6: Rietveld Refinement parameters and band gap of doped ZnO nanowires produced by microwave synthesis.

	Calcium				***Europium***				***Gallium***			
Doping (mol%)	**a=b** (Å)	**c** (Å)	**c/a**	E_g **(eV)**	**a=b** (Å)	**c** (Å)	**c/a**	E_g **(eV)**	**a=b** (Å)	**c** (Å)	**c/a**	E_g **(eV)**
0	3.2499	5.2070	1.6022	3.060	3.2499	5.2070	1.6022	3.060	3.2499	5.2070	1.6022	3.060
1	3.2493	5.2054	1.6020	3.146	3.2494	5.2059	1.6021	3.198	3.2510	5.2080	1.6022	3.134
2	3.2497	5.2068	1.6022	3.216	3.2507	5.2081	1.6021	3.228	3.2499	5.2068	1.6022	3.178
3	3.2505	5.2080	1.6022	3.230	3.2499	5.2066	1.6021	3.234	3.2508	5.2083	1.6022	3.152
4	3.2501	5.2073	1.6022	3.252	3.2508	5.2084	1.6022	3.214	3.2509	5.2084	1.6022	3.118
5	3.2498	5.2069	1.6022	3.245	3.2495	5.2062	1.6022	3.237	3.2509	5.2086	1.6022	3.150

The Table 3.6 summarizes all the lattice parameters values, c/a ratios and band gaps, for different dopant agents studied (Ca, Eu and Ga) and their different doping molar percentages in microwave synthesis. It is reported that pure ZnO has a band gap between 3.1 and 3.2 eV [80]. The band gap of all doped ZnO NWs increases significantly from the undoped to 1 mol% and after that it has smaller non-linear changes.

In a broad manner, it is possible to say that the lattice parameters and band gaps are strongly dependent on the type and mol% for each doping agent.

CHAPTER 4

4. Conclusions and Future Perspectives

This work intended to synthetize and characterize annealed and doped ZnO nanowires for optoelectronic applications. The ZnO nanowires characterization was performed based on the synthetized ZnO morphology, structure and optical characteristics.

The SEM images for each different synthesis conditions showed that annealing temperature and doping does impact the morphology and surface of these nanowires. Comparisons were made regarding the aspect and length. It was found that in conventional synthesis the highest the annealing temperature was, the lowest the length of the nanowires. At the same time, the length on the microwave synthesis varied in a way which was not possible to take effectively conclusions. As for the dopant agents, the type of dopant and the molar percentage of it has influenced differently the morphology of the ZnO nanowires altering the shape of the undoped nanowire.

An XRD analysis was also conducted to verify the structure and material synthetized, as well as the crystallite sizes. For undoped nanowires the obtained peaks matched with hexagonal wurtzite crystalline structure, as well as, for undoped annealed nanowires. As for the doped ZnO nanowires, it was spotted other phases in XRD diffractograms. The europium doped ZnO nanowires, for instance, as a phase associated with Eu $(OH)_3$ which may be the origin of some segregation. When comparing types of heating, the microwave synthesis and conventional synthesis has some disparities on crystallite size values, which may be described by differences in temperature and pressure. As for doped nanostructures the variations in crystallite size were mainly caused by distortions in the lattice sites. All this was true for both types of synthesis experimented.

It was analysed the microstructural information of the doped ZnO NWs with Rietveld Refinement method and lattice parameters were taken for both syntheses. It is concluded that the values are different when applied to different types of dopants, as well as when looked for both syntheses and each doping agent. The c/a ratio presented, varies with mol% and has no particular standard behaviour, nevertheless is sufficient to conclude that those ions affect the overall lattice system depending of the size of the ionic radius in comparison with Zn^{2+} ionic radius.

The optical band gap of all the undoped and doped ZnO, as well as, annealed ZnO nanostructures were analysed. The values are between 3.1 and 3.2 eV which is in good agreement with literature. The differences between each annealed temperature, as well as, between each mol% of doping agent is, in general, too small to effectively and reliably reach major conclusions.

This work allows to show that there is a lot of potential in the area of ZnO nanostructures and in particular of ZnO NWs. However, some research is required to be made to improve the knowledge of how these systems behave. In the future, a characterization of the annealed doped ZnO is required as well as some improvement and optimization of the synthesis for dopants with the objective of isolate doped ZnO NWs.

Characterization techniques as FTIR, AFM, Raman, Photoluminescence, XPS and TEM must be considered in future investigations to a deeper understanding of the ZnO behaviour. As for Rietveld Refinement Method, an optimization as well as an integration with other software that allows to build a simulation of the diffraction pattern of the material (in this case ZnO) with the integrated atoms in the lattice must be taken into account.

CHAPTER 5

5. Bibliography

[1] T. Terada, ‘Capillary cavernous hemangioma of the lymph node’, *Int. J. Clin. Exp. Pathol.*, vol. 6, no. 6, pp. 1200–1201, 2013.

[2] C. Soci *et al.*, ‘ZnO nanowire UV photodetectors with high internal gain’, *Nano Lett.*, vol. 7, no. 4, pp. 1003–1009, 2007.

[3] L. Schmidt-Mende and J. L. MacManus-Driscoll, ‘ZnO - nanostructures, defects, and devices’, *Mater. Today*, vol. 10, no. 5, pp. 40–48, 2007.

[4] G. Yi, C. Wang, and W. Il Park, ‘박진호(1208)Zno Nano Rods.Pdf’, vol. 22, 2005.

[5] Z. L. Wang, ‘Novel nanostructures of ZnO for nanoscale photonics, optoelectronics, piezoelectricity, and sensing’, *Appl. Phys. A Mater. Sci. Process.*, vol. 88, no. 1, pp. 7–15, 2007.

[6] T. Guo, M. S. Yao, Y. H. Lin, and C. W. Nan, ‘A comprehensive review on synthesis methods for transition-metal oxide nanostructures’, *CrystEngComm*, vol. 17, no. 19, pp. 3551–3585, 2015.

[7] I. Level, *Fazendo crescer a aplicação*, vol. 5. 1988.

[8] D. Nunes, A. Pimentel, L. Santos, P. Barquinha, E. Fortunato, and R. Martins, ‘Photocatalytic TiO2 Nanorod Spheres and Arrays Compatible with Flexible Applications’, *Catalysts*, vol. 7, no. 12, p. 60, 2017.

[9] A. Pimentel *et al.*, ‘Synthesis of long ZnO nanorods under microwave irradiation or conventional heating’, *J. Phys. Chem. C*, vol. 118, no. 26, pp. 14629–14639, 2014.

[10] D. Nunes *et al.*, *Structural, optical, and electronic properties of metal oxide nanostructures*. 2018.

[11] L. Santos *et al.*, ‘WO3 nanoparticle-based conformable pH sensor’, *ACS Appl. Mater. Interfaces*, vol. 6, no. 15, pp. 12226–12234, 2014.

[12] D. Nunes, A. Pimentel, P. Barquinha, P. A. Carvalho, E. Fortunato, and R. Martins, ‘Cu2O polyhedral nanowires produced by microwave irradiation’, *J. Mater. Chem. C*, vol. 2, no. 30, pp. 6097–6103, 2014.

[13] H. L. Karlsson, P. Cronholm, J. Gustafsson, and L. Mo, ‘Copper Oxide Nanoparticles Are Highly Toxic A Comparison between Metal Oxide Nanoparticles and Carbon Nanotubes - Chemical Research in Toxicology (ACS Publications)’, *Chem. Res. Toxicol.*, vol. 21, pp. 1726–1732, 2008.

[14] A. Pimentel *et al.*, ‘Effect of solvents on ZnO nanostructures synthesized by solvothermal method assisted by microwave radiation: a photocatalytic study’, *J. Mater. Sci.*, vol. 50,

no. 17, pp. 5777–5787, 2015.

[15] C. B. Ong, L. Y. Ng, and A. W. Mohammad, ‘A review of ZnO nanoparticles as solar photocatalysts: Synthesis, mechanisms and applications’, *Renew. Sustain. Energy Rev.*, vol. 81, no. March 2017, pp. 536–551, 2018.

[16] E. Fortunato *et al.*, ‘Zinc oxide, a multifunctional material: From material to device applications’, *Appl. Phys. A Mater. Sci. Process.*, vol. 96, no. 1, pp. 197–205, 2009.

[17] K. M. H, ‘Group one impurities in single crystalline Zinc Oxide’, no. January, 2011.

[18] A. B. Djurišić, X. Chen, Y. H. Leung, and A. Man Ching Ng, ‘ZnO nanostructures: Growth, properties and applications’, *J. Mater. Chem.*, vol. 22, no. 14, pp. 6526–6535, 2012.

[19] S. Baruah *et al.*, ‘Hydrothermal growth of ZnO nanostructures’, *Appl. Phys. Lett.*, vol. 86, no. 1, pp. 1–3, 2014.

[20] Y. Meng, Y. Lin, and Y. Lin, ‘Electrodeposition for the synthesis of ZnO nanorods modified by surface attachment with ZnO nanoparticles and their dye-sensitized solar cell applications’, *Ceram. Int.*, vol. 40, no. 1 PART B, pp. 1693–1698, 2014.

[21] J. Rodrigues *et al.*, ‘ZnO micro/nanocrystals grown by laser assisted flow deposition’, *Oxide-based Mater. Devices V*, vol. 8987, p. 89871F, 2014.

[22] B. Liu and H. C. Zeng, ‘Hydrothermal Synthesis of ZnO Nanorods in Diameter Regime of 50 nm - supporting info’, *J. Am. Chem. Soc.*, pp. S1–S2, 2003.

[23] S. Baruah and J. Dutta, ‘Hydrothermal growth of ZnO nanostructures’, *Sci. Technol. Adv. Mater.*, vol. 10, no. 1, 2009.

[24] T. Ichikawa and S. Shiratori, ‘Fabrication and evaluation of ZnO nanorods by liquid-phase deposition’, *Inorg. Chem.*, vol. 50, no. 3, pp. 999–1004, 2011.

[25] J. Pérez-Juste, I. Pastoriza-Santos, L. M. Liz-Marzán, and P. Mulvaney, ‘Gold nanorods: Synthesis, characterization and applications’, *Coord. Chem. Rev.*, vol. 249, no. 17-18 SPEC. ISS., pp. 1870–1901, 2005.

[26] W. I. Park, D. H. Kim, S. W. Jung, and G. C. Yi, ‘Metalorganic vapor-phase epitaxial growth of vertically well-aligned ZnO nanorods’, *Appl. Phys. Lett.*, vol. 80, no. 22, pp. 4232–4234, 2002.

[27] A. M. Bagamadova and A. K. Omaev, ‘Gas-phase synthesis of zinc oxide nanorods’, *Tech. Phys. Lett.*, vol. 41, no. 9, pp. 874–876, 2015.

[28] N. I. Rusli, M. Tanikawa, M. R. Mahmood, K. Yasui, and A. M. Hashim, ‘Growth of high-density zinc oxide nanorods on porous silicon by thermal evaporation’, *Materials (Basel).*, vol. 5, no. 12, pp. 2817–2832, 2012.

[29] N. SHOJAEE, T. EBADZADEH, and A. AGHAEI, ‘ Microwave assisted hydrothermal synthesize of ZnO nanorods and their characterization ’, *Int. J. Mod. Phys. Conf. Ser.*, vol.

05, pp. 72–78, 2012.

[30] A. Ul Hassan Sarwar Rana, M. Kang, and H. S. Kim, ‘Microwave-assisted Facile and Ultrafast Growth of ZnO Nanostructures and Proposition of Alternative Microwave-assisted Methods to Address Growth Stoppage’, *Sci. Rep.*, vol. 6, no. January, pp. 1–13, 2016.

[31] S. T. Tan, A. A. Umar, M. Yahaya, C. C. Yap, and M. M. Salleh, ‘Ultrafast formation of ZnO nanorods via seed-mediated microwave assisted hydrolysis process’, *J. Phys. Conf. Ser.*, vol. 431, no. 1, 2013.

[32] D. S. Y. Jayathilake *et al.*, ‘Microwave-Assisted Synthesis and Processing of Al-Doped, Ga-Doped, and Al, Ga Codoped ZnO for the Pursuit of Optimal Conductivity for Transparent Conducting Film Fabrication’, *ACS Sustain. Chem. Eng.*, vol. 5, no. 6, pp. 4820–4829, 2017.

[33] S. Y. Bae, C. W. Na, J. H. Kang, and J. Park, ‘Comparative structure and optical properties of Ga-, In-, and Sn-doped ZnO nanowires synthesized via thermal evaporation’, *J. Phys. Chem. B*, vol. 109, no. 7, pp. 2526–2531, 2005.

[34] S. Cimitan, S. Albonetti, L. Forni, F. Peri, and D. Lazzari, ‘Solvothermal synthesis and properties control of doped ZnO nanoparticles’, *J. Colloid Interface Sci.*, vol. 329, no. 1, pp. 73–80, 2009.

[35] S. B. Majumder, M. Jain, P. S. Dobal, and R. S. Katiyar, ‘Investigations on solution derived aluminium doped zinc oxide thin films’, *Mater. Sci. Eng. B Solid-State Mater. Adv. Technol.*, vol. 103, no. 1, pp. 16–25, 2003.

[36] J. Zuo, C. Xu, L. Zhang, B. Xu, and R. Wu, ‘Sb-induced size effects in ZnO nanocrystallites’, *J. Raman Spectrosc.*, vol. 32, no. 11, pp. 979–981, 2001.

[37] C. Xu, M. Kim, J. Chun, and D. Kim, ‘Growth of Ga-doped ZnO nanowires by two-step vapor phase method’, *Appl. Phys. Lett.*, vol. 86, no. 13, pp. 1–3, 2005.

[38] T. Agne *et al.*, ‘Doping of the nanocrystalline semiconductor zinc oxide with the donor indium’, *Appl. Phys. Lett.*, vol. 83, no. 6, pp. 1204–1206, 2003.

[39] Z. Potůček, Z. Bryknar, P. Ptáček, and Z. Hubička, ‘Luminescence of defects in Li-doped ZnO thin films’, *Phys. Status Solidi C Conf.*, vol. 2, no. 1, pp. 256–259, 2005.

[40] D. Phan and G. Chung, ‘CO Gas Sensing Using Ga Doping ZnO Nanorods by Hydrothermal Method : Effects of Defects-Controlled’, *14th Int. Meet. Chem. Sensors*, pp. 1070–1073, 2012.

[41] L. C. K. Liau and J. S. Huang, ‘Effect of indium- and gallium-doped ZnO fabricated through sol-gel processing on energy level variations’, *Mater. Res. Bull.*, vol. 97, no. May 2017, pp. 6–12, 2018.

[42] H. Wang, S. Baek, J. Song, J. Lee, and S. Lim, ‘Microstructural and optical characteristics

of solution-grown Ga-doped ZnO nanorod arrays', *Nanotechnology*, vol. 19, no. 7, 2008.

[43] R. C. Alkire, P. N. Bartlett, and J. Lipkowski, *Nanopatterned and Nanoparticle-Modified Electrodes*. John Wiley & Sons, Incorporated, 2017.

[44] D. Li, Z. T. Liu, Y. H. Leung, A. B. Djurišić, M. H. Xie, and W. K. Chan, 'Transition metal-doped ZnO nanorods synthesized by chemical methods', *J. Phys. Chem. Solids*, vol. 69, no. 2–3, pp. 616–619, 2008.

[45] F. Li, L. Hu, Z. Li, and X. Huang, 'Influence of temperature on the morphology and luminescence of ZnO micro and nanostructures prepared by CTAB-assisted hydrothermal method', *J. Alloys Compd.*, vol. 465, no. 1–2, pp. 14–19, 2008.

[46] B. Baruwati, D. K. Kumar, and S. V. Manorama, 'Hydrothermal synthesis of highly crystalline ZnO nanoparticles: A competitive sensor for LPG and EtOH', *Sensors Actuators, B Chem.*, vol. 119, no. 2, pp. 676–682, 2006.

[47] J. Zhang, L. Sun, J. Yin, H. Su, and C. Liao, 'Control of ZnO Morphology via a Simple Solution Route Control of ZnO Morphology via a Simple Solution Route', vol. 14, no. 10, pp. 4172–4177, 2002.

[48] S. Baruah and J. Dutta, 'Hydrothermal growth of ZnO nanostructures', *Sci. Technol. Adv. Mater.*, vol. 10, no. 1, 2009.

[49] H. M. Rietveld, 'A profile refinement method for nuclear and magnetic structures', *J. Appl. Crystallogr.*, vol. 2, no. 2, pp. 65–71, 1969.

[50] D. L. Bish and S. A. Howard, 'Quantitative phase analysis using the Rietveld method', *J. Appl. Crystallogr.*, vol. 21, no. 2, pp. 86–91, 1988.

[51] R. S. Winburn, D. G. Grier, G. J. McCarthy, and R. B. Peterson, 'Rietveld quantitative X-ray diffraction analysis of NIST fly ash standard reference materials', *Powder Diffr.*, vol. 15, no. 3, pp. 163–172, 2000.

[52] N. V. Y. Scarlett and I. C. Madsen, 'Quantification of phases with partial or no known crystal structures', *Powder Diffr.*, vol. 21, no. 4, pp. 278–284, 2006.

[53] D. Jansen, C. Stabler, F. Goetz-Neunhoeffer, S. Dittrich, and J. Neubauer, 'Does Ordinary Portland Cement contain amorphous phase? A quantitative study using an external standard method', *Powder Diffr.*, vol. 26, no. 1, pp. 31–38, 2011.

[54] X. Y. Kong, Y. Ding, R. Yang, and Z. L. Wang, 'Single-Crystal Nanorings Formed by Epitaxial Self-Coiling of Polar Nanobelts', *Science (80-.).*, vol. 303, no. 5662, pp. 1348–1351, 2004.

[55] A. Singh and H. L. Vishwakarma, 'Study of structural, morphological, optical and electroluminescent properties of undoped ZnO nanorods grown by a simple chemical precipitation', *Mater. Sci. Pol.*, vol. 33, no. 4, pp. 751–759, 2015.

[56] B. Ludi and M. Niederberger, 'Zinc oxide nanoparticles: Chemical mechanisms and

classical and non-classical crystallization', *Dalt. Trans.*, vol. 42, no. 35, pp. 12554–12568, 2013.

[57] Z. L. Wang *et al.*, 'Semiconducting and piezoelectric oxide nanostructures induced by polar surfaces', *Adv. Funct. Mater.*, vol. 14, no. 10, pp. 943–956, 2004.

[58] B. H. Toby and R. B. Von Dreele, 'GSAS-II: The genesis of a modern open-source all purpose crystallography software package', *J. Appl. Crystallogr.*, vol. 46, no. 2, pp. 544–549, 2013.

[59] 'Diogo António Silva Coelho Solution Based Synthesis of ZnO Nanorods for Optoelectronic Applications', 2019.

[60] A. Pimentel *et al.*, 'Effect of solvents on ZnO nanostructures synthesized by solvothermal method assisted by microwave radiation: a photocatalytic study', *J. Mater. Sci.*, vol. 50, no. 17, pp. 5777–5787, 2015.

[61] E. Mohammadi, M. Aliofkhazraei, M. Hasanpoor, and M. Chipara, 'Hierarchical and Complex ZnO Nanostructures by Microwave-Assisted Synthesis: Morphologies, Growth Mechanism and Classification', *Crit. Rev. Solid State Mater. Sci.*, vol. 43, no. 6, pp. 475–541, 2018.

[62] L. Jäppinen *et al.*, 'Enhanced Photoluminescence in Acetylene-Treated ZnO Nanorods', *Nanoscale Res. Lett.*, vol. 11, no. 1, 2016.

[63] M. S. Al-Assiri, M. M. Mostafa, M. A. Ali, and M. M. El-Desoky, 'Synthesis, structural and electrical properties of annealed ZnO thin films deposited by pulsed laser deposition (PLD)', *Superlattices Microstruct.*, vol. 75, pp. 127–135, 2014.

[64] M. M. El-Desoky, M. A. Ali, G. Afifi, H. Imam, and M. S. Al-Assiri, 'Effects of Annealing Temperatures on the Structural and Dielectric Properties of ZnO Nanoparticles', *Silicon*, vol. 10, no. 2, pp. 301–307, 2018.

[65] N. I. Maad Tazri and W. M. Wan Ahmad Kamil, 'Effect of Annealing Temperature in ZnO for Photonic Applications', *J. Phys. Conf. Ser.*, vol. 1083, no. 1, 2018.

[66] Q. Humayun, M. Kashif, and U. Hashim, 'Structural, optical, electrical, and photoresponse properties of postannealed Sn-doped ZnO nanorods', *J. Nanomater.*, vol. 2013, 2013.

[67] D. Padilla Rueda, J. M. Vadillo, and J. J. Laserna, 'Effects of post-growth thermal annealing on room temperature pulsed laser deposited ZnO thin films', *J. Phys. Conf. Ser.*, vol. 687, no. 1, pp. 9–13, 2016.

[68] R. Raji and K. G. Gopchandran, 'ZnO nanostructures with tunable visible luminescence: Effects of kinetics of chemical reduction and annealing', *J. Sci. Adv. Mater. Devices*, vol. 2, no. 1, pp. 51–58, 2017.

[69] N. Kamarulzaman, M. F. Kasim, and R. Rusdi, 'Band Gap Narrowing and Widening of ZnO Nanostructures and Doped Materials', *Nanoscale Res. Lett.*, vol. 10, no. 1, 2015.

[70] B. Santoshkumar, S. Kalyanaraman, R. Vettumperumal, R. Thangavel, I. V. Kityk, and S. Velumani, ‘Structure-dependent anisotropy of the photoinduced optical nonlinearity in calcium doped ZnO nanorods grown by low cost hydrothermal method for photonic device applications’, *J. Alloys Compd.*, vol. 658, pp. 435–439, 2016.

[71] O. M. Ntwaeaborwa, S. J. Mofokeng, V. Kumar, and R. E. Kroon, ‘Structural, optical and photoluminescence properties of Eu3 + doped ZnO nanoparticles’, *Spectrochim. Acta - Part A Mol. Biomol. Spectrosc.*, vol. 182, no. April, pp. 42–49, 2017.

[72] A. F. V. da Fonseca *et al.*, ‘A theoretical and experimental investigation of Eu-doped ZnO nanorods and its application on dye sensitized solar cells’, *J. Alloys Compd.*, vol. 739, pp. 939–947, 2018.

[73] P. Mohanty, B. Kim, and J. Park, ‘Synthesis of single crystalline europium-doped ZnO nanowires’, *Mater. Sci. Eng. B Solid-State Mater. Adv. Technol.*, vol. 138, no. 3, pp. 224–227, 2007.

[74] A. Khan, M. I. Ahmed, A. Adam, A. M. Azad, and M. Qamar, ‘A novel fabrication methodology for sulfur-doped ZnO nanorods as an active photoanode for improved water oxidation in visible-light regime’, *Nanotechnology*, vol. 28, no. 5, 2017.

[75] H. Long, A. Habeeb, D. Kinyua, K. Wang, B. Wang, and P. Lu, ‘Influences of Ga Doping on Crystal Structure and Polarimetric Pattern of SHG in ZnO Nanofilms’, *Nanomaterials*, vol. 9, no. 6, p. 905, 2019.

[76] S. Goel, N. Sinha, H. Yadav, S. Godara, A. J. Joseph, and B. Kumar, ‘Ferroelectric Gd-doped ZnO nanostructures: Enhanced dielectric, ferroelectric and piezoelectric properties’, *Mater. Chem. Phys.*, vol. 202, pp. 56–64, 2017.

[77] E. Melo, ‘Síntese e caracterização de alvo de óxido de zinco dopado com alumínio’, *Aleph*, pp. 1–102, 2015.

[78] S. López-Romero, M. J. Quiroz-Jiménez, M. H. García, and A. Aguilar-Castillo, ‘Bright Red Luminescence and Structural Properties of Eu<sup>3+</sup> Ion Doped ZnO by Solution Combustion Technique’, *World J. Condens. Matter Phys.*, vol. 04, no. 04, pp. 227–234, 2014.

[79] J. U. Brehm, M. Winterer, and H. Hahn, ‘Synthesis and local structure of doped nanocrystalline zinc oxides’, *J. Appl. Phys.*, vol. 100, no. 6, pp. 1–9, 2006.

[80] A. Pimentel *et al.*, ‘Synthesis of long ZnO nanorods under microwave irradiation or conventional heating’, *J. Phys. Chem. C*, vol. 118, no. 26, pp. 14629–14639, 2014.

CHAPTER 6

6. Annexes

6.1. Annex A – Growth of ZnO nanowires

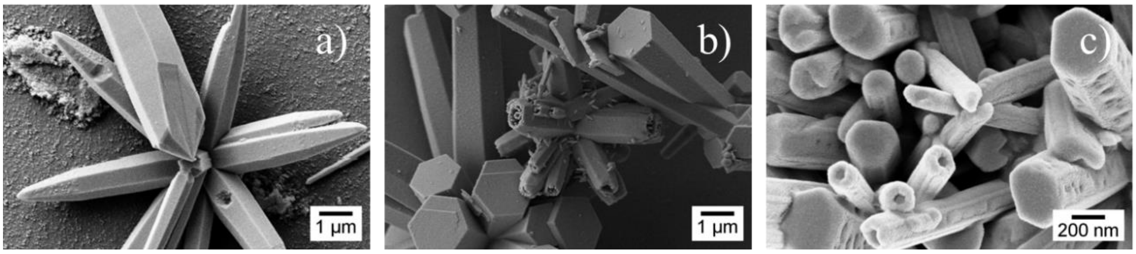

Figure 6.1: SEM images of nanostructures produced by microwave synthesis with 0 mol% (a), 1 mol% (b) and 5 mol% of calcium (c).

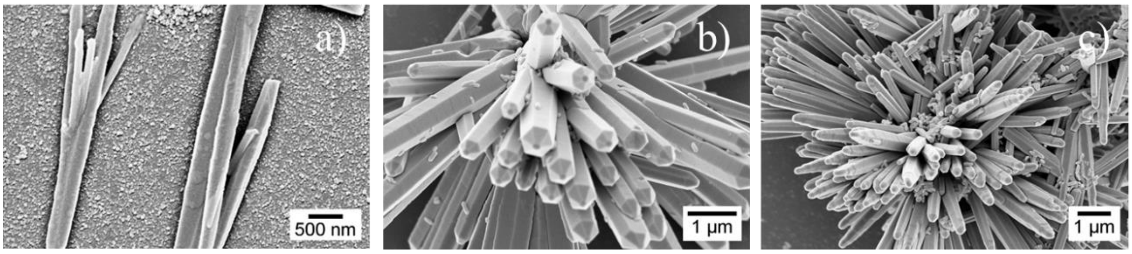

Figure 6.2: SEM images of nanostructures produced by conventional synthesis with 0 mol% (a) 1 mol% (b) and 5 mol% of europium (c).

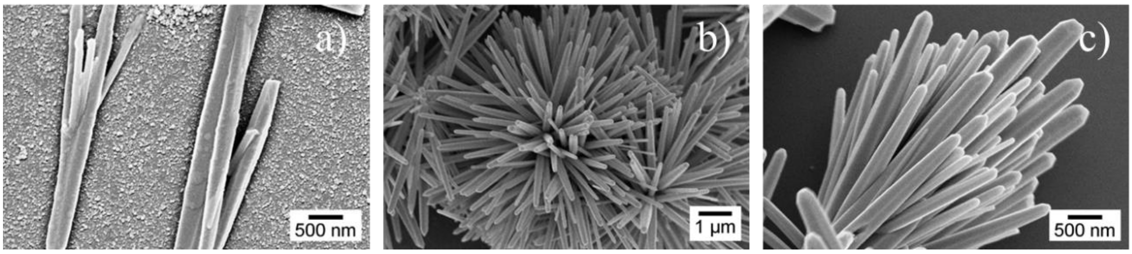

Figure 6.3: SEM images of nanostructures produced by conventional synthesis with 0 mol% (a), 1 mol% (b) and 5 mol% of gallium (c).

6.2. **Annex B – Structural Analysis of Nanostructures**

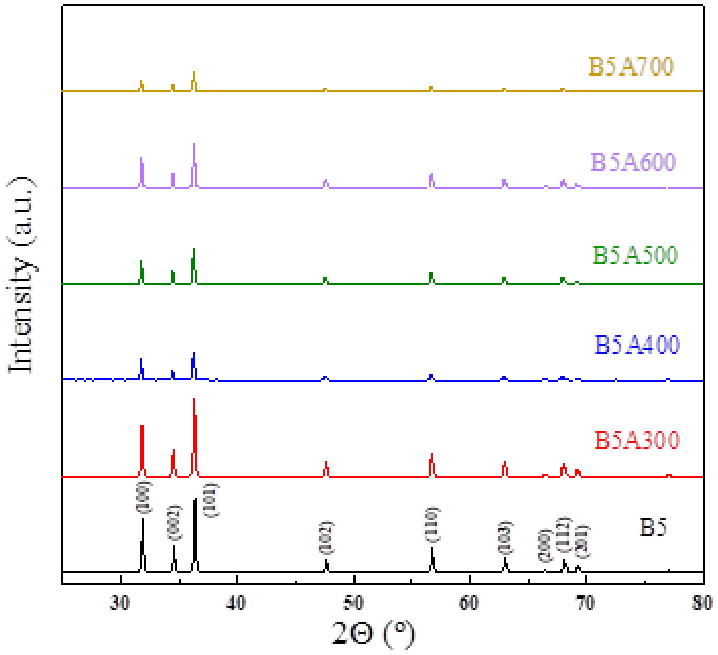

Figure 6.4: XRD diffractograms of ZnO nanostructures produced by conventional synthesis, annealed at different temperatures.

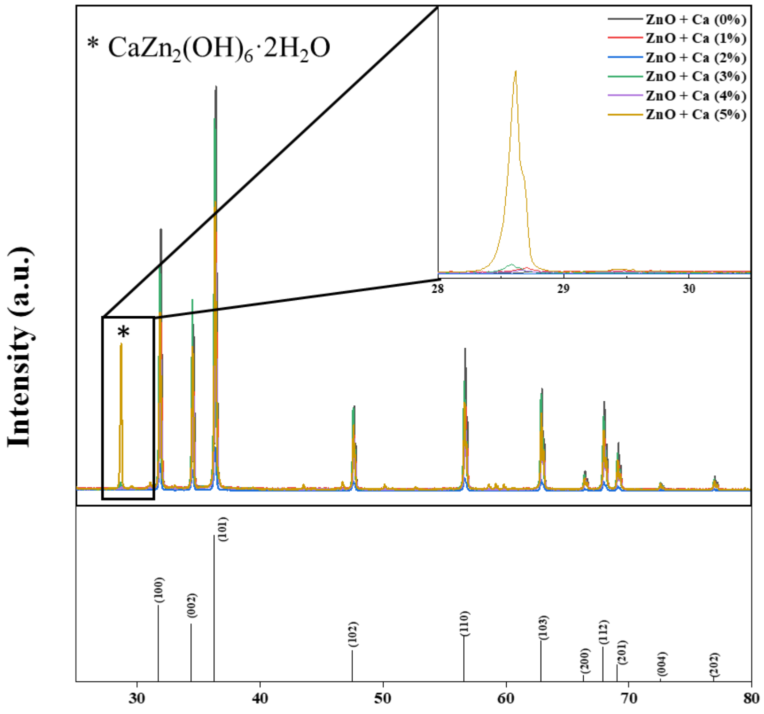

Figure 6.5: Example of XRD diffractograms of different calcium doping molar percentages produced by microwave synthesis.

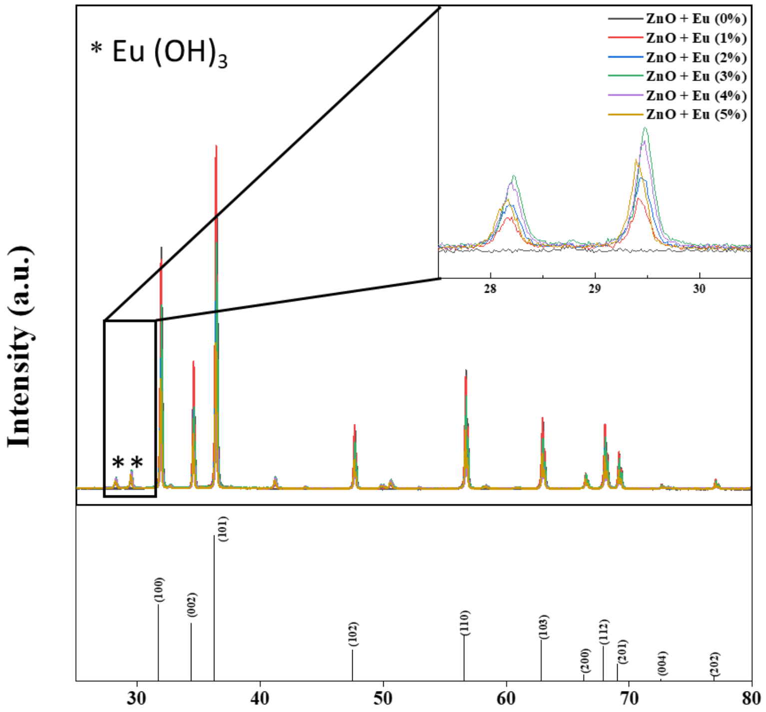

Figure 6.6: Example of XRD diffractograms of different europium doping molar percentages produced by conventional synthesis.

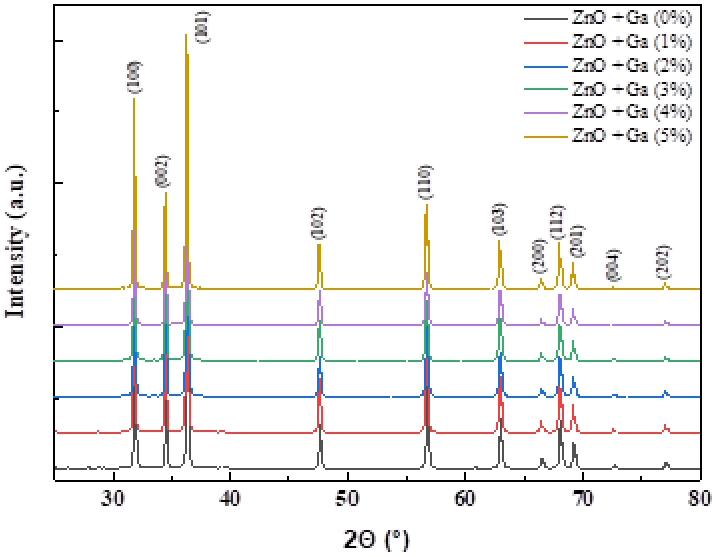

Figure 6.7: Example of XRD diffractograms of different gallium doping molar percentages produced by conventional synthesis.

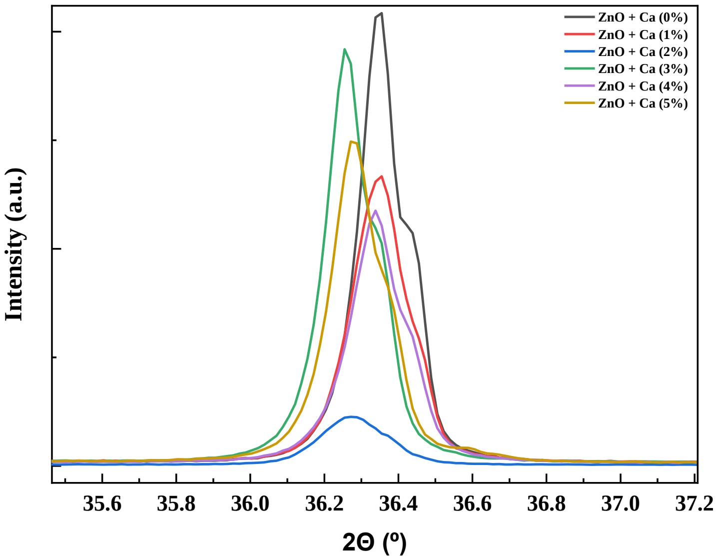

Figure 6.8: Zoom in on (101) difraction plane of XRD diffractograms of different calcium doping molar percentages produced by microwave synthesis.

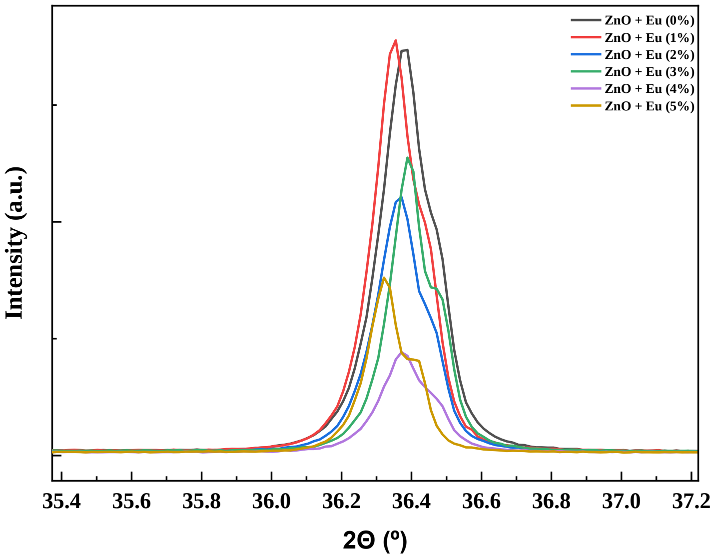

Figure 6.9: Zoom in on (101) difraction plane of XRD diffractograms of different europium doping molar percentages produced by conventional synthesis.

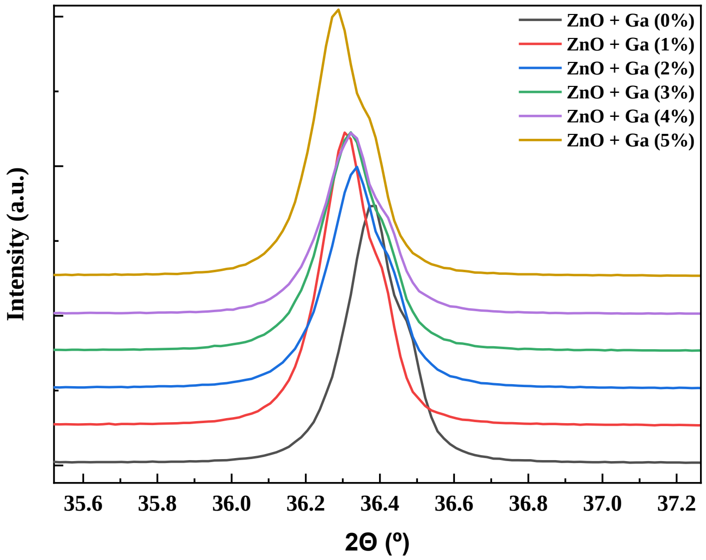

Figure 6.10: Zoom in on (101) difraction plane of XRD diffractograms of different gallium doping molar percentages produced by conventional synthesis.

6.3. **Annex C – Rietveld Refinement Procedure**

In this section will be presented a tutorial of how Rietveld Refinement method can be done. To begin it should be created a new project where all the next steps will be processed (Figure 6.11).

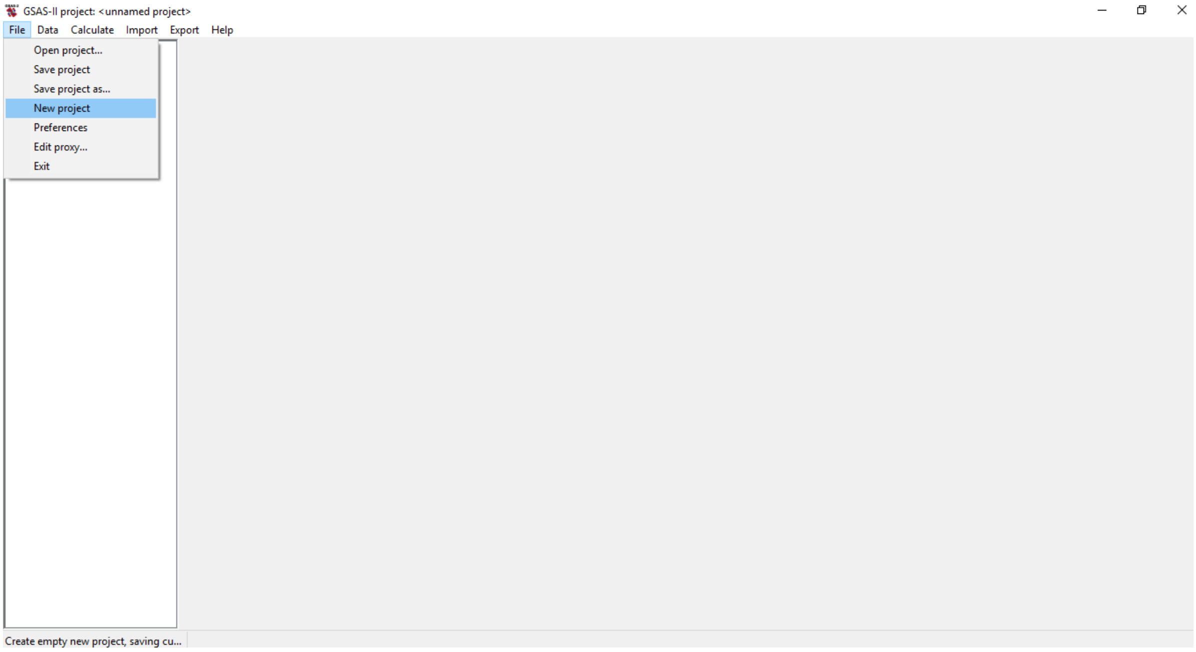

Create empty new project, saving cu...

Figure 6.11: Creating a new project in Gsas II.

The next step is importing the XRD file related to the instrument parameters (Figure 6.12 and Figure 6.13). This is the beginning of the instrument parameter calibration process needed before data collection.

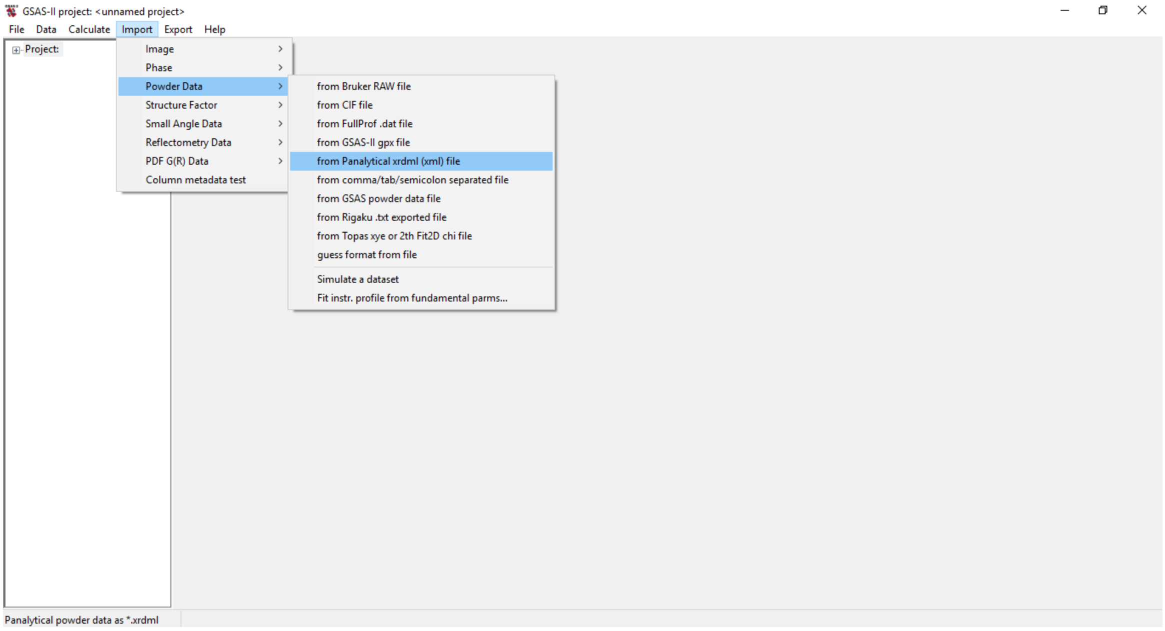

Panalytical powder data as *.xrdml

Figure 6.12: Importing na XRD data file on Gsas II.

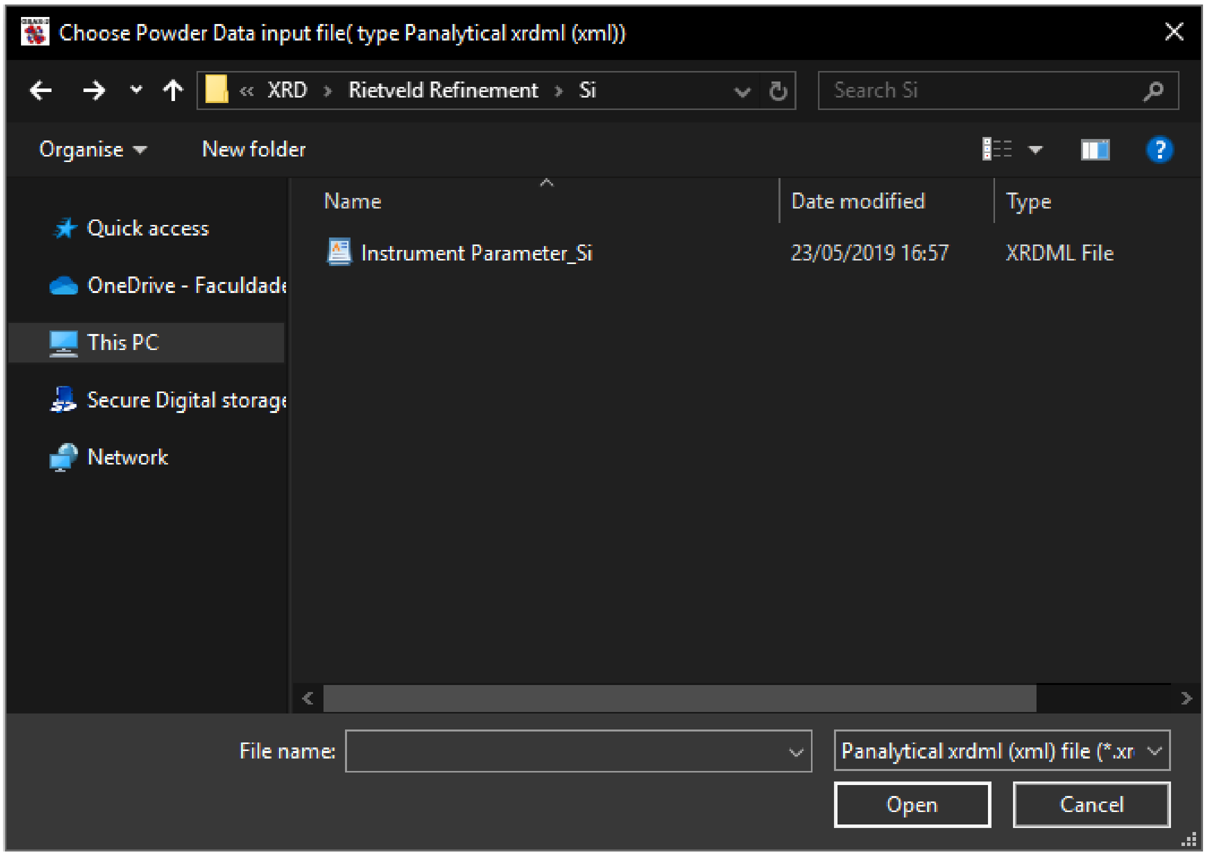

Choose Powder Data input file(type Panalytical xrdml (xml))

Name	Date modified	Type
Instrument Parameter_Si	23/05/2019 16:57	XRDML File

Figure 6.13: Selecting the file to determine the instrument parameters.

When opened the instrument file it should appear a window to confirm the file that the program must read (Figure 6.14).

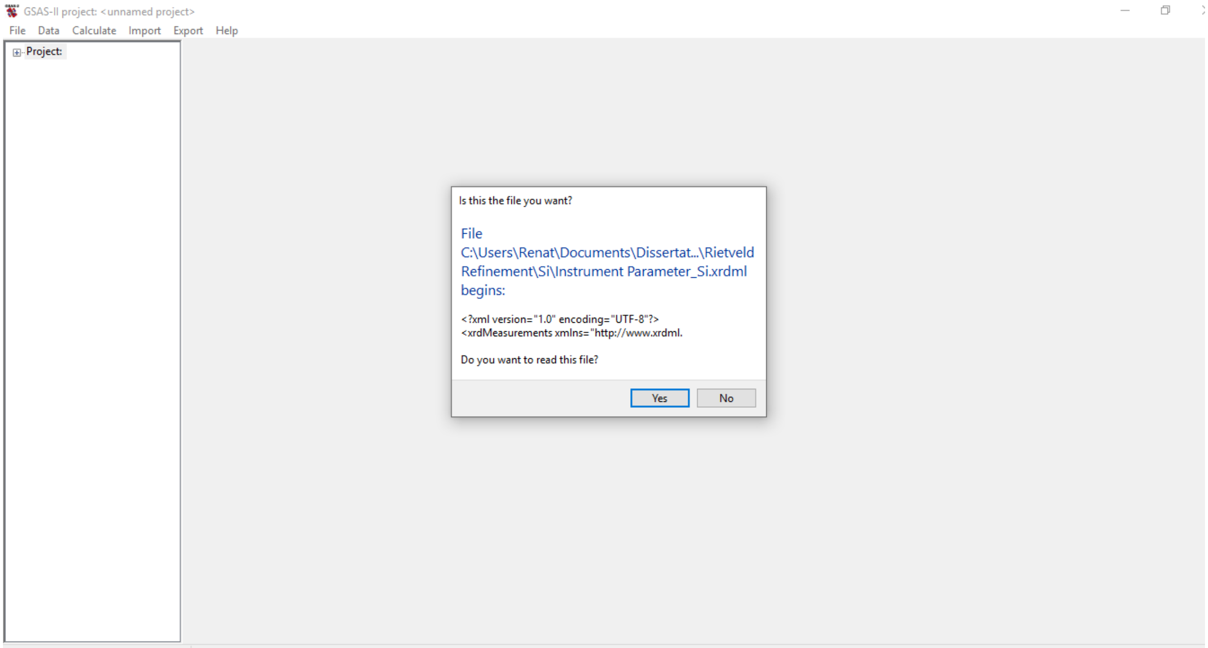

Is this the file you want?

File C:\Users\Renat\Documents\Dissertat...\Rietveld Refinement\Si\Instrument Parameter_Si.xrdml begins:

```
<?xml version="1.0" encoding="UTF-8"?>
<xrdMeasurements xmlns="http://www.xrdml.
```

Do you want to read this file?

Figure 6.14: Confirming the file that Gsas II must read.

By default, the program will ask for the instrument parameter file. Click cancel and a window with default instrument parameters should appear (Figure 6.15). For now, choose the "Defaults for Cukα lab data" (Figure 6.16).

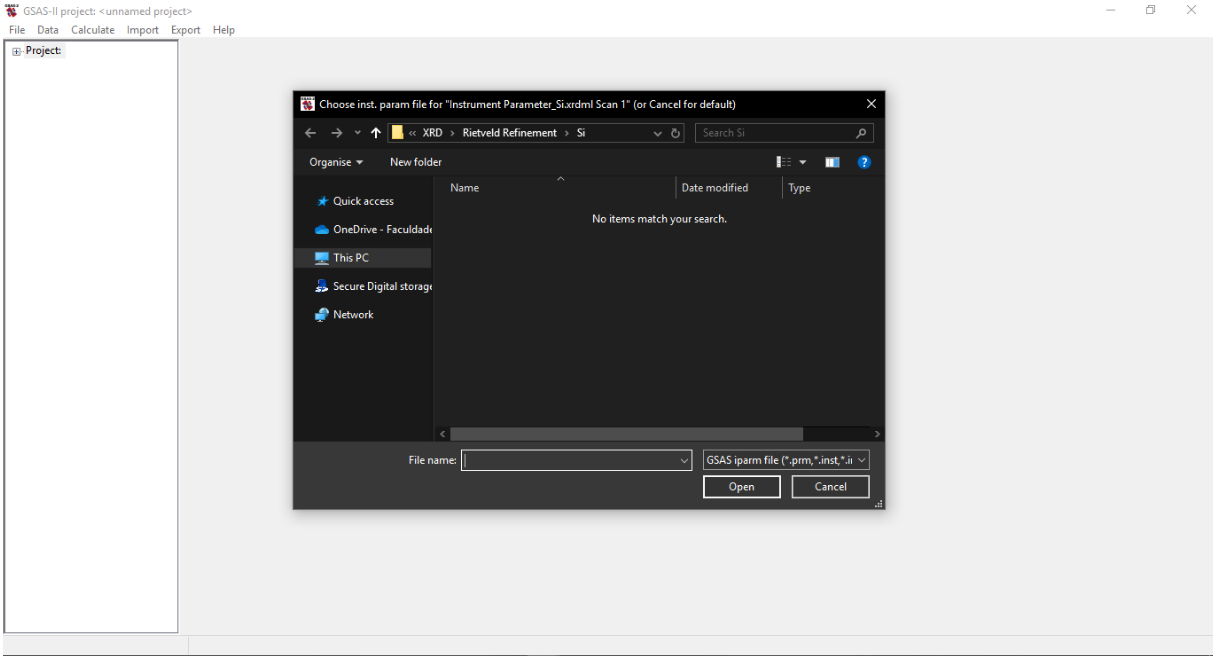

Choose inst. param file for "Instrument Parameter_Si.xrdml Scan 1" (or Cancel for default)

No items match your search.

Figure 6.15: Default window to select instrument parameter file on Gsas II.

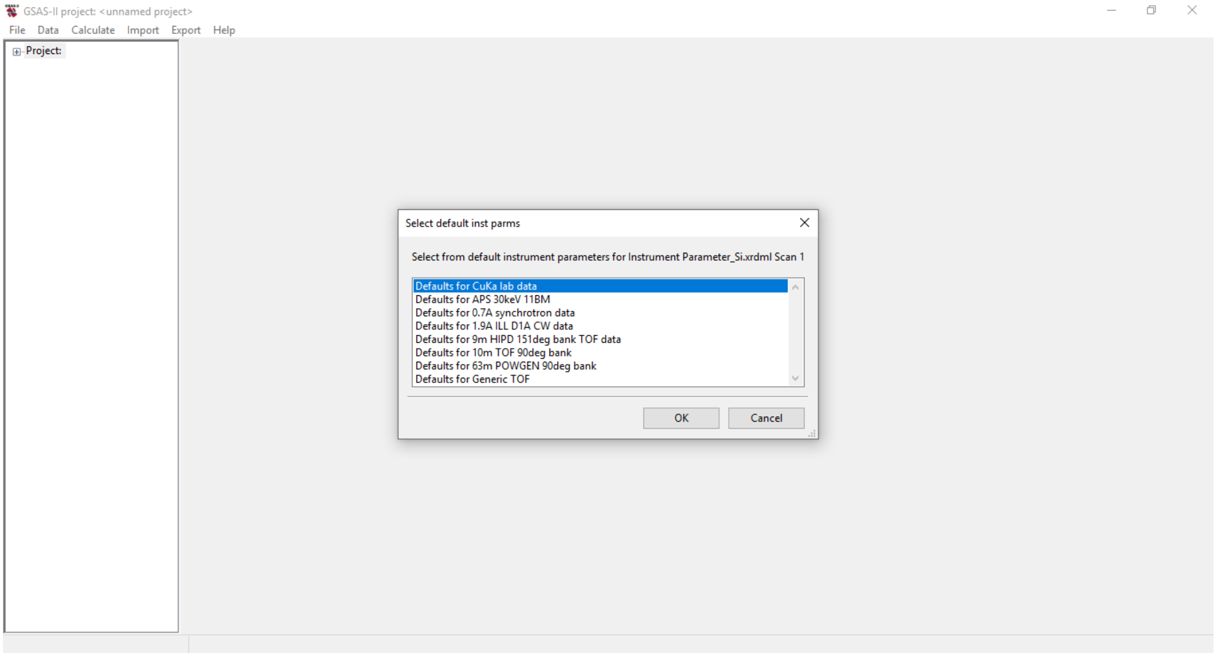

Select default inst parms

Select from default instrument parameters for Instrument Parameter_Si.xrdml Scan 1

Defaults for CuKa lab data
Defaults for APS 30keV 11BM
Defaults for 0.7A synchrotron data
Defaults for 1.9A ILL D1A CW data
Defaults for 9m HIPD 151deg bank TOF data
Defaults for 10m TOF 90deg bank
Defaults for 63m POWGEN 90deg bank
Defaults for Generic TOF

Figure 6.16: Window with the default intrument parameters for data on Gsas II.

At this point, two windows must appear. The one on the left has all the important parameters that should be altered to create the instrument parameter file. The one on the right as the XRD file ready to be refined (Figure 6.17).

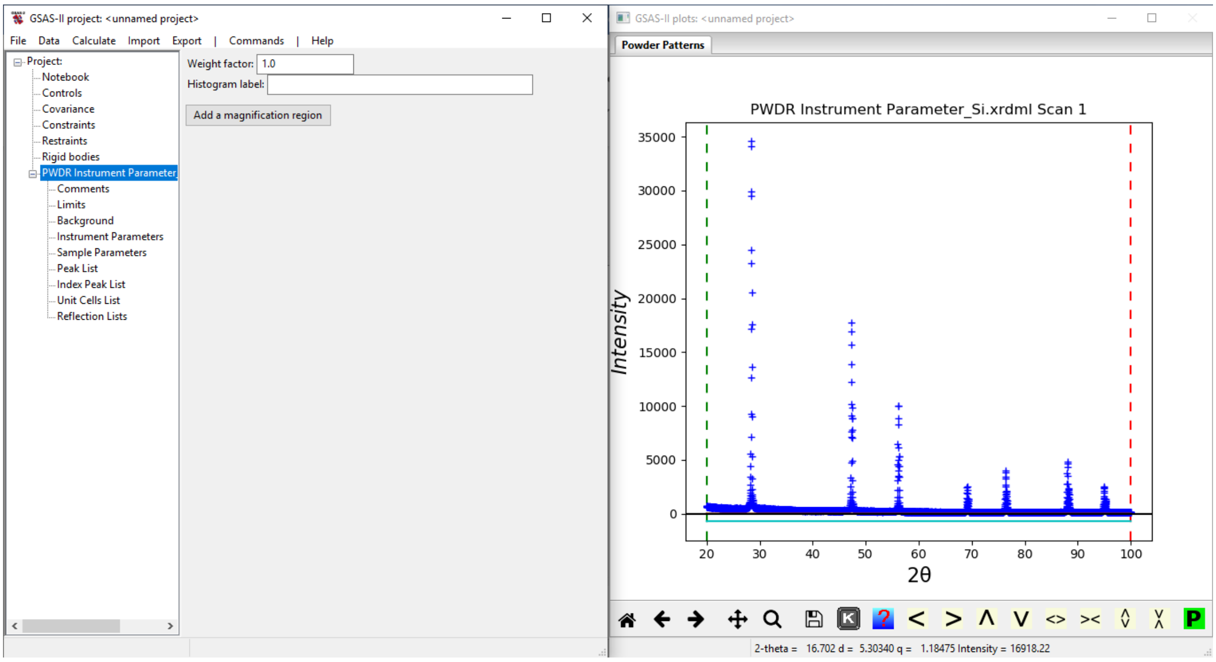

Weight factor: 1.0
Histogram label:

2-theta = 16.702 d = 5.30340 q = 1.18475 Intensity = 16918.22

Figure 6.17: On the left there is the data tree with the different parameters to change. On the right the initial XRD spectra of silicon.

In the subsection "Background", change the number of coefficients of Chebyshev function between 6 and 10 (Figure 6.18). This value is enough to improve the fitting of the background. Then go to instrument parameters and choose "source type" (Figure 6.19). In this study we use CuKα as the source.

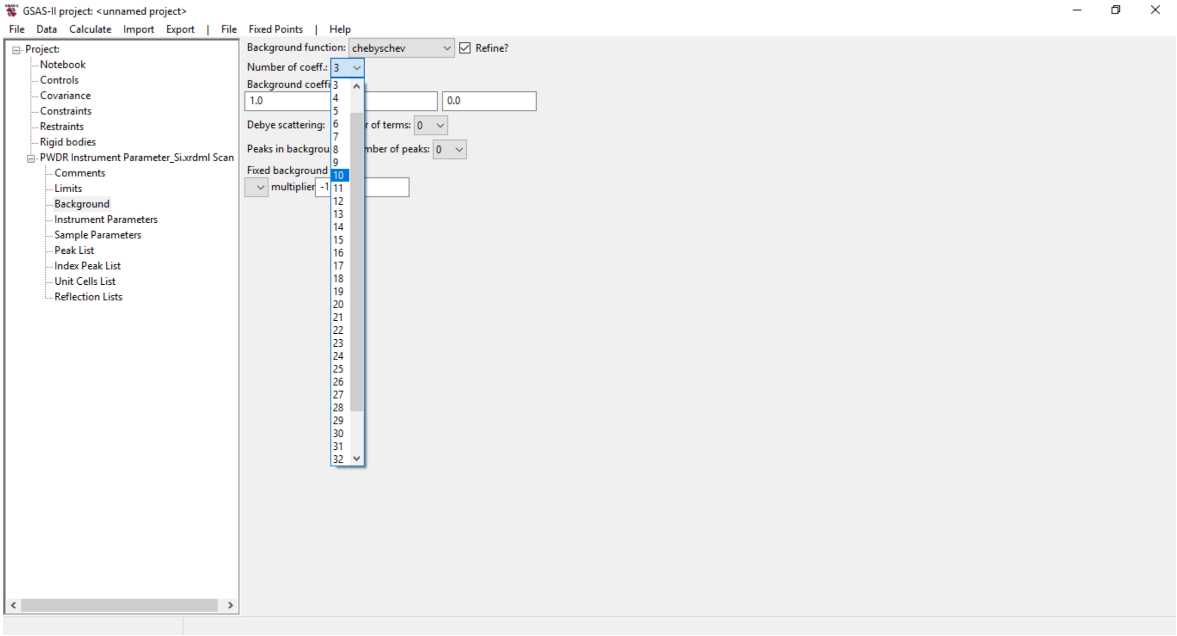

Background function: chebyschev ☑ Refine?
Number of coeff.: 3
Background coeffi
1.0 0.0
Debye scattering: r of terms: 0
Peaks in backgrou mber of peaks: 0
Fixed background
multiplier -1

Figure 6.18: Selecting the number of coefficients for the background function.

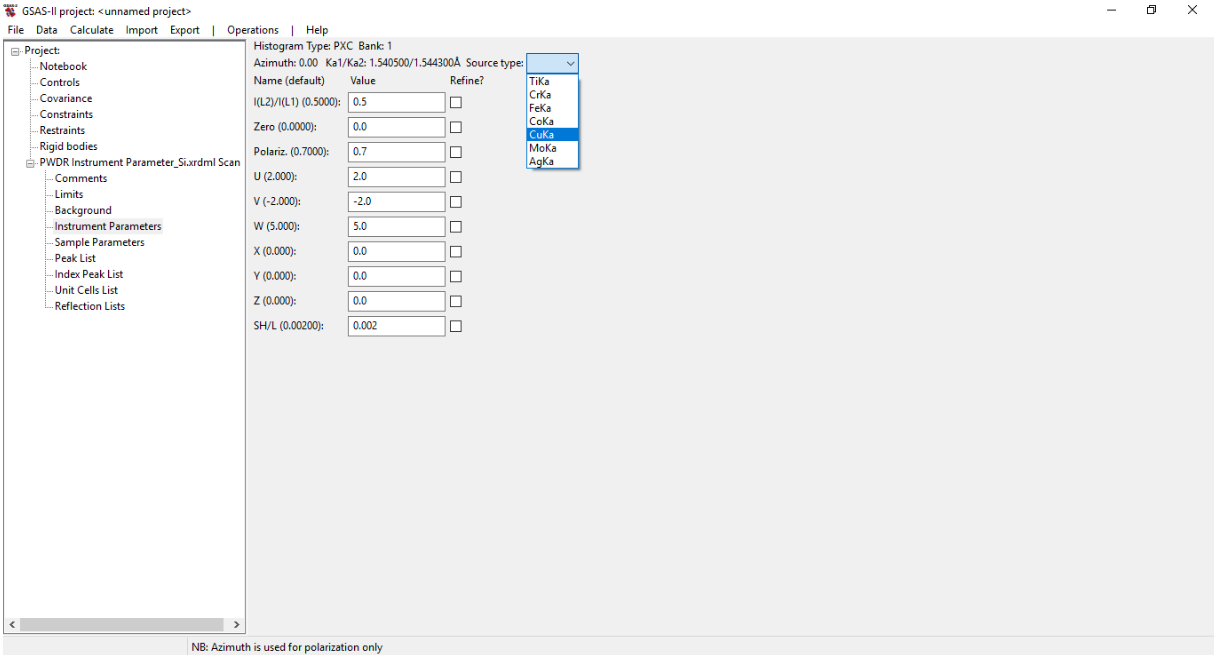

Histogram Type: PXC Bank: 1

Azimuth: 0.00 Ka1/Ka2: 1.540500/1.544300Å Source type:

Name (default)	Value	Refine?
I(L2)/I(L1) (0.5000):	0.5	☐
Zero (0.0000):	0.0	☐
Polariz. (0.7000):	0.7	☐
U (2.000):	2.0	☐
V (-2.000):	-2.0	☐
W (5.000):	5.0	☐
X (0.000):	0.0	☐
Y (0.000):	0.0	☐
Z (0.000):	0.0	☐
SH/L (0.00200):	0.002	☐

NB: Azimuth is used for polarization only

Figure 6.19: Selecting the Source type used.

Next step is searching for peaks in the XRD calibration data. To do that select peak list from the data tree, and then on “peak fitting” choose “Auto search” (Figure 6.20). Now a window with the XRD spectra and the correspondent peaks will appear (Figure 6.21).

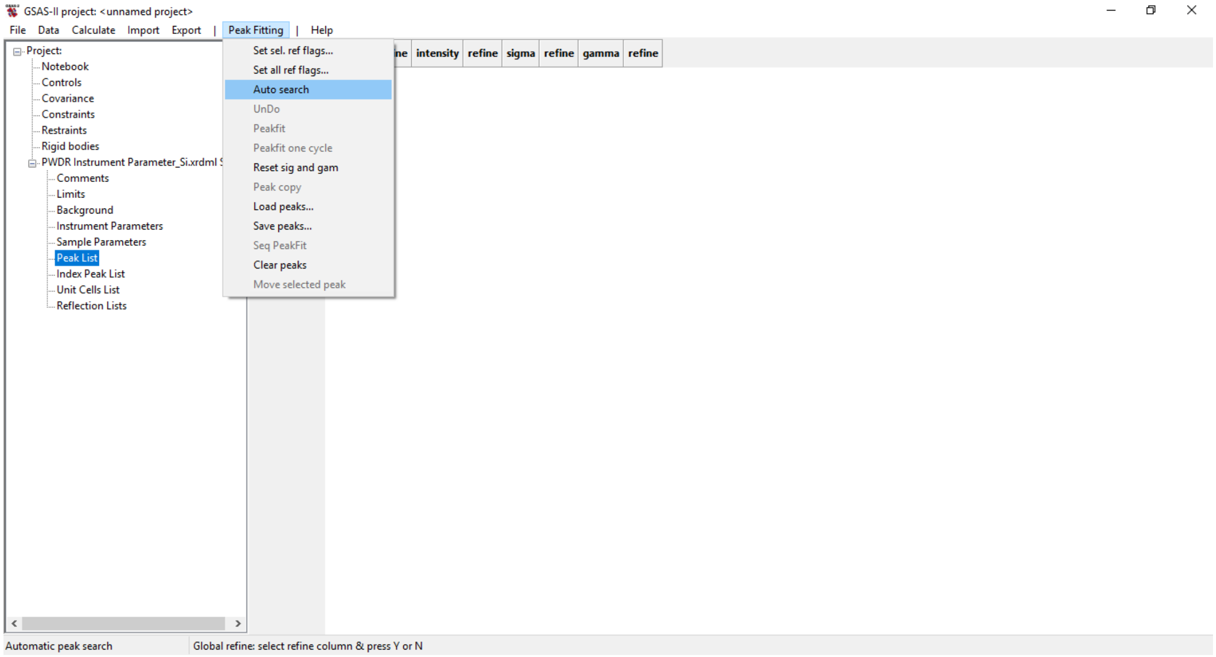

Automatic peak search

Global refine: select refine column & press Y or N

Figure 6.20: Step for searching peaks in an XRD data spectra.

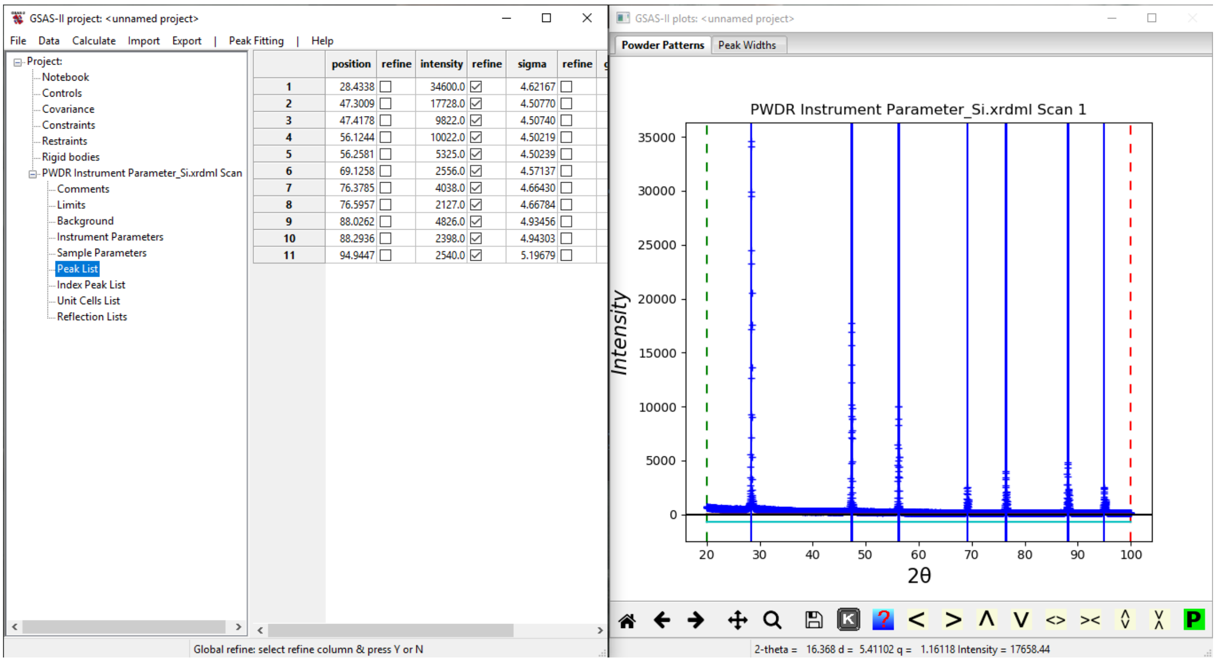

	position	refine	intensity	refine	sigma	refine
1	28.4338	☐	34600.0	☑	4.62167	☐
2	47.3009	☐	17728.0	☑	4.50770	☐
3	47.4178	☐	9822.0	☑	4.50740	☐
4	56.1244	☐	10022.0	☑	4.50219	☐
5	56.2581	☐	5325.0	☑	4.50239	☐
6	69.1258	☐	2556.0	☑	4.57137	☐
7	76.3785	☐	4038.0	☑	4.66430	☐
8	76.5957	☐	2127.0	☑	4.66784	☐
9	88.0262	☐	4826.0	☑	4.93456	☐
10	88.2936	☐	2398.0	☑	4.94303	☐
11	94.9447	☐	2540.0	☑	5.19679	☐

Global refine: select refine column & press Y or N

2-theta = 16.368 d = 5.41102 q = 1.16118 Intensity = 17658.44

Figure 6.21: On the left there is the peak list of the XRD data spectra represented on the right.

The next stage of process starts with refining all the intensities of the founded peaks. To do that check all the intensities boxes as shown in Figure 6.22. Then go to “Peak fitting” and choose “Peakfit”. As shown on Figure 6.23, the peaks are still a little off. Same procedure should be applied for positions (Figure 6.24 and Figure 6.25).

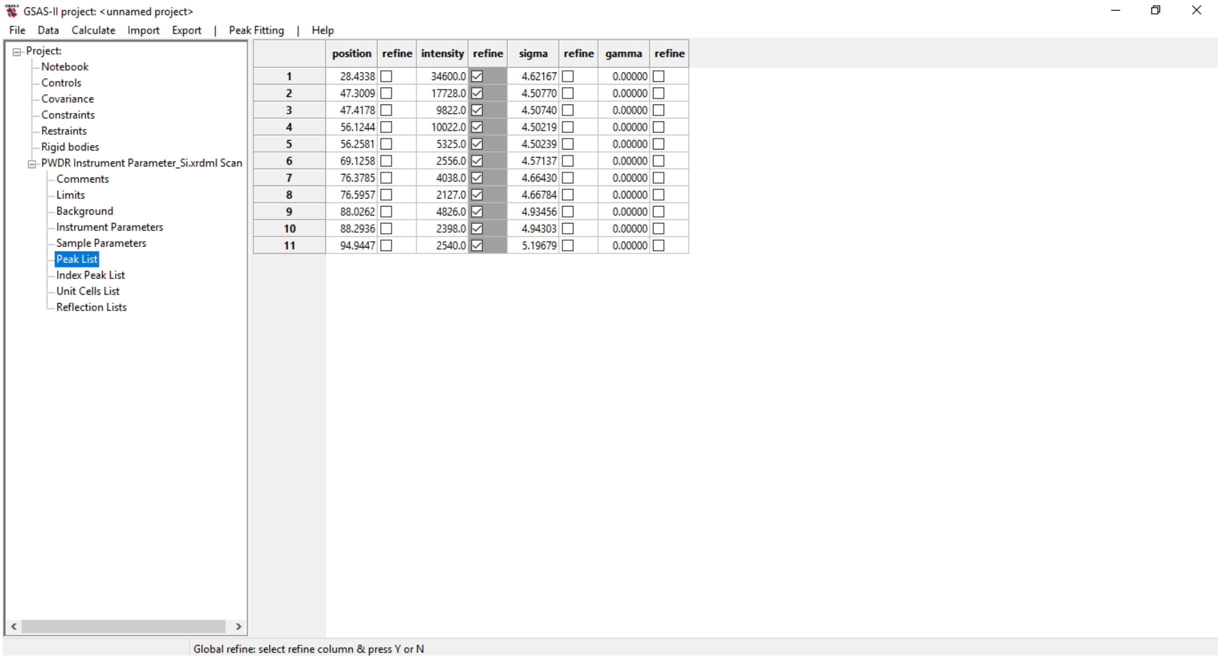

	position	refine	intensity	refine	sigma	refine	gamma	refine
1	28.4338	☐	34600.0	☑	4.62167	☐	0.00000	☐
2	47.3009	☐	17728.0	☑	4.50770	☐	0.00000	☐
3	47.4178	☐	9822.0	☑	4.50740	☐	0.00000	☐
4	56.1244	☐	10022.0	☑	4.50219	☐	0.00000	☐
5	56.2581	☐	5325.0	☑	4.50239	☐	0.00000	☐
6	69.1258	☐	2556.0	☑	4.57137	☐	0.00000	☐
7	76.3785	☐	4038.0	☑	4.66430	☐	0.00000	☐
8	76.5957	☐	2127.0	☑	4.66784	☐	0.00000	☐
9	88.0262	☐	4826.0	☑	4.93456	☐	0.00000	☐
10	88.2936	☐	2398.0	☑	4.94303	☐	0.00000	☐
11	94.9447	☐	2540.0	☑	5.19679	☐	0.00000	☐

Global refine: select refine column & press Y or N

Figure 6.22: Checking all the boxes for all intensities.

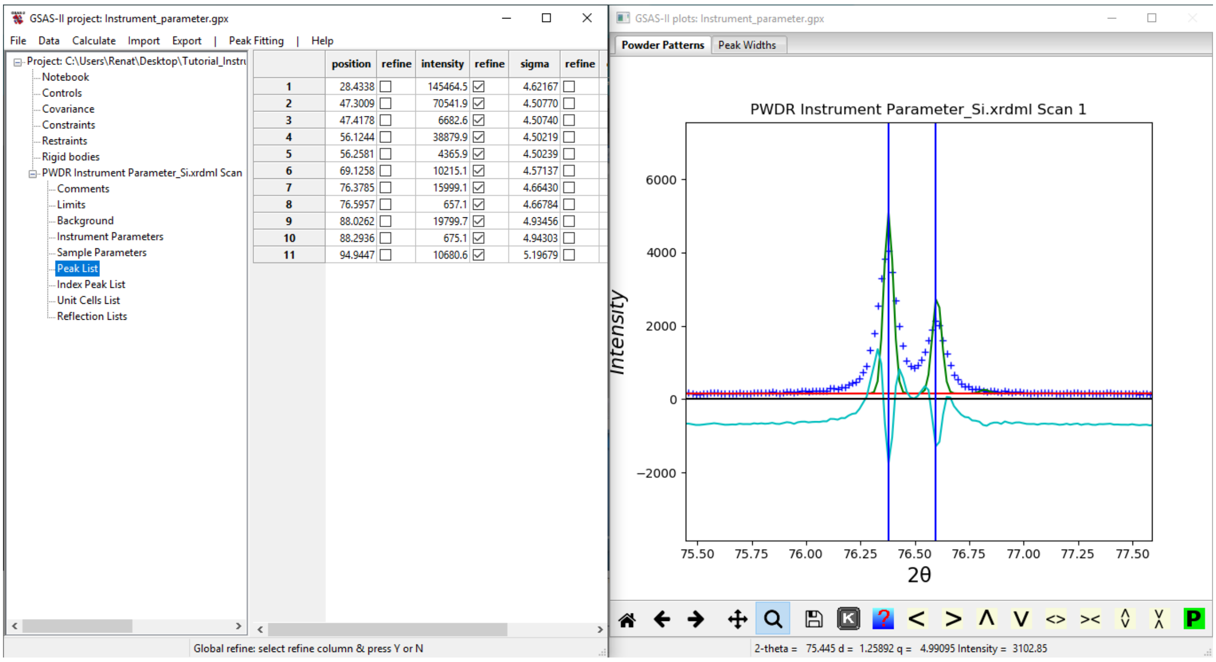

	position	refine	intensity	refine	sigma	refine
1	28.4338	☐	145464.5	☑	4.62167	☐
2	47.3009	☐	70541.9	☑	4.50770	☐
3	47.4178	☐	6682.6	☑	4.50740	☐
4	56.1244	☐	38879.9	☑	4.50219	☐
5	56.2581	☐	4365.9	☑	4.50239	☐
6	69.1258	☐	10215.1	☑	4.57137	☐
7	76.3785	☐	15999.1	☑	4.66430	☐
8	76.5957	☐	657.1	☑	4.66784	☐
9	88.0262	☐	19799.7	☑	4.93456	☐
10	88.2936	☐	675.1	☑	4.94303	☐
11	94.9447	☐	10680.6	☑	5.19679	☐

Global refine: select refine column & press Y or N

2-theta = 75.445 d = 1.25892 q = 4.99095 Intensity = 3102.85

Figure 6.23: On the right a zoom in on the XRD spectra shows the calcuted values not yet well fitted with the experimental values.

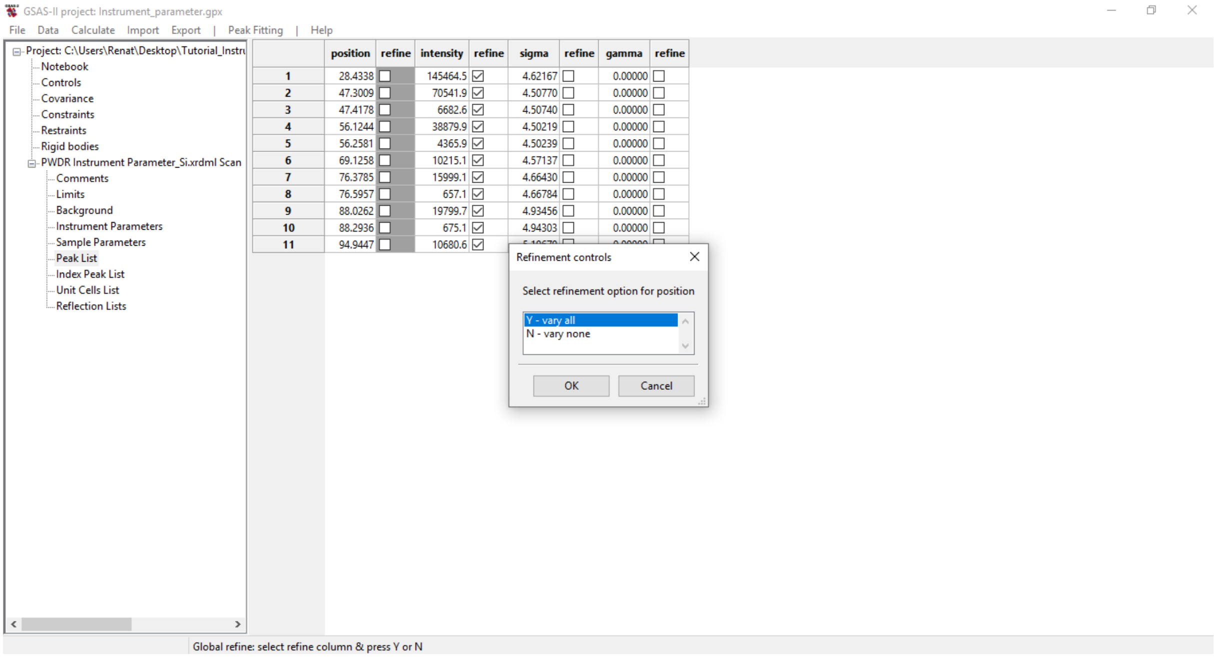

	position	refine	intensity	refine	sigma	refine	gamma	refine
1	28.4338	☐	145464.5	☑	4.62167	☐	0.00000	☐
2	47.3009	☐	70541.9	☑	4.50770	☐	0.00000	☐
3	47.4178	☐	6682.6	☑	4.50740	☐	0.00000	☐
4	56.1244	☐	38879.9	☑	4.50219	☐	0.00000	☐
5	56.2581	☐	4365.9	☑	4.50239	☐	0.00000	☐
6	69.1258	☐	10215.1	☑	4.57137	☐	0.00000	☐
7	76.3785	☐	15999.1	☑	4.66430	☐	0.00000	☐
8	76.5957	☐	657.1	☑	4.66784	☐	0.00000	☐
9	88.0262	☐	19799.7	☑	4.93456	☐	0.00000	☐
10	88.2936	☐	675.1	☑	4.94303	☐	0.00000	☐
11	94.9447	☐	10680.6	☑	[illegible]	☐	[illegible]	☐

Refinement controls

Select refinement option for position

Y - vary all
N - vary none

Global refine: select refine column & press Y or N

Figure 6.24: Checking all the boxes for all positions.

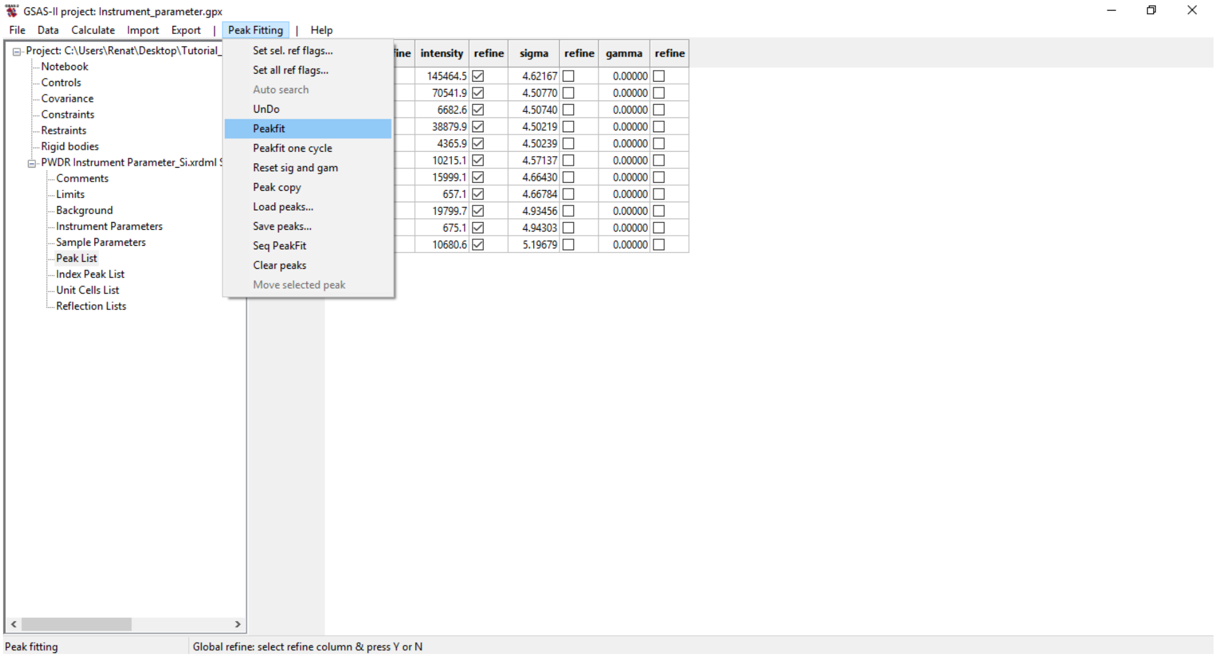

intensity	refine	sigma	refine	gamma	refine
145464.5	☑	4.62167	☐	0.00000	☐
70541.9	☑	4.50770	☐	0.00000	☐
6682.6	☑	4.50740	☐	0.00000	☐
38879.9	☑	4.50219	☐	0.00000	☐
4365.9	☑	4.50239	☐	0.00000	☐
10215.1	☑	4.57137	☐	0.00000	☐
15999.1	☑	4.66430	☐	0.00000	☐
657.1	☑	4.66784	☐	0.00000	☐
19799.7	☑	4.93456	☐	0.00000	☐
675.1	☑	4.94303	☐	0.00000	☐
10680.6	☑	5.19679	☐	0.00000	☐

Global refine: select refine column & press Y or N

Figure 6.25: Fitting the position values of the peaks.

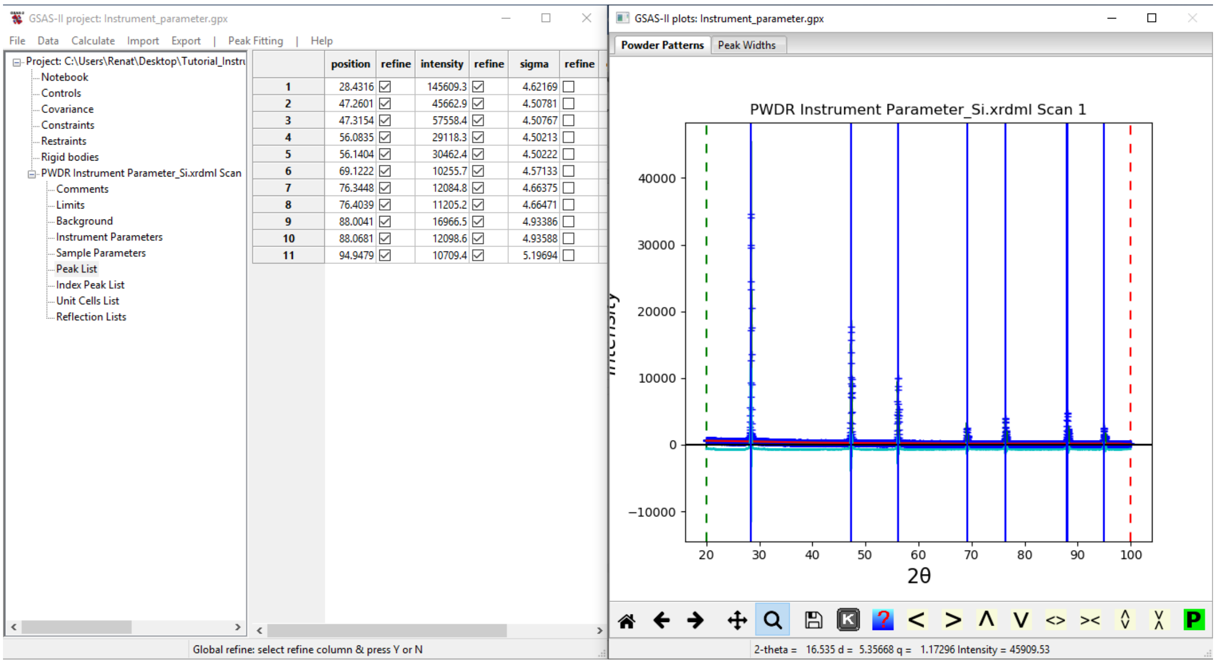

	position	refine	intensity	refine	sigma	refine
1	28.4316	☑	145609.3	☑	4.62169	☐
2	47.2601	☑	45662.9	☑	4.50781	☐
3	47.3154	☑	57558.4	☑	4.50767	☐
4	56.0835	☑	29118.3	☑	4.50213	☐
5	56.1404	☑	30462.4	☑	4.50222	☐
6	69.1222	☑	10255.7	☑	4.57133	☐
7	76.3448	☑	12084.8	☑	4.66375	☐
8	76.4039	☑	11205.2	☑	4.66471	☐
9	88.0041	☑	16966.5	☑	4.93386	☐
10	88.0681	☑	12098.6	☑	4.93588	☐
11	94.9479	☑	10709.4	☑	5.19694	☐

Global refine: select refine column & press Y or N

2-theta = 16.535 d = 5.35668 q = 1.17296 Intensity = 45909.53

Figure 6.26: XRD spectra fitted are shown on the right. The position and intensity refined values are shown on the left.

To improve the fitting, go to “instrument parameters” and check U, W and X. Next step is to set V, Y and SH/L to zero (Later on they will change to default minimum) as shown on Figure 6.27. Then go to “peak list” in “Peak Fitting” and select “Peakfit” (Figure 6.28). As shown on Figure 6.29 and Figure 6.30, the fitting is much improved and the X, U and W parameters are refined as well as the V, Y and SH/L are set to default minima. Last step is to save the instrument parameters. Go to “instrument parameters” in “Operations” tab and choose “save profile” (Figure 6.31). Now the instrument parameter file is saved for later use.

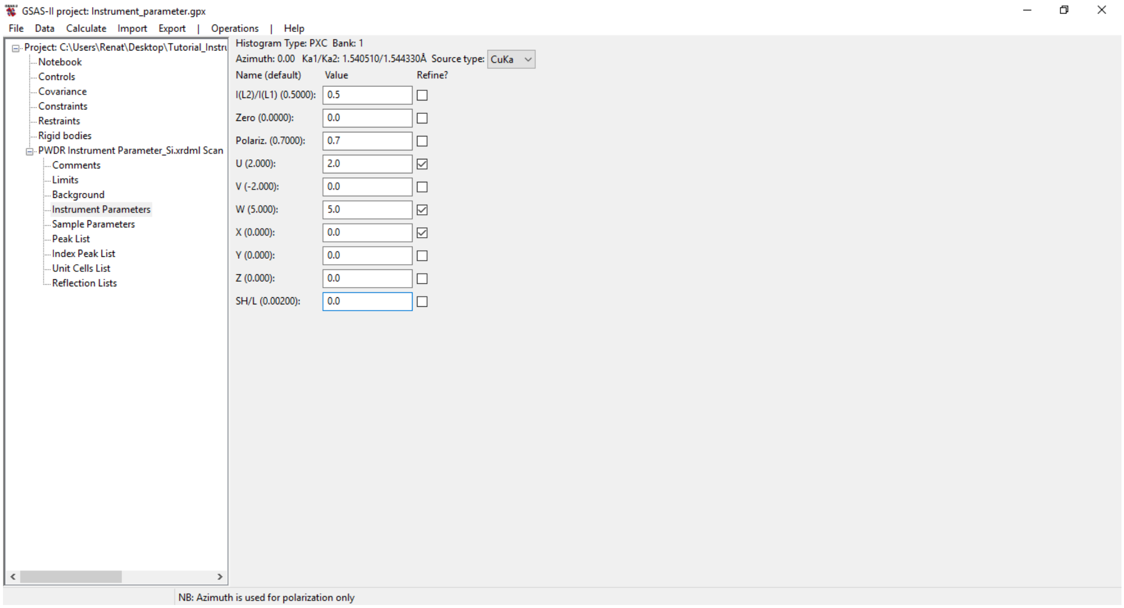

Histogram Type: PXC Bank: 1

Azimuth: 0.00 Ka1/Ka2: 1.540510/1.544330Å Source type: CuKa

Name (default)	Value	Refine?
I(L2)/I(L1) (0.5000):	0.5	☐
Zero (0.0000):	0.0	☐
Polariz. (0.7000):	0.7	☐
U (2.000):	2.0	☑
V (-2.000):	0.0	☐
W (5.000):	5.0	☑
X (0.000):	0.0	☑
Y (0.000):	0.0	☐
Z (0.000):	0.0	☐
SH/L (0.00200):	0.0	☐

NB: Azimuth is used for polarization only

Figure 6.27: Selecting U, W and X to refine and set V, Y and SH/L to zero.

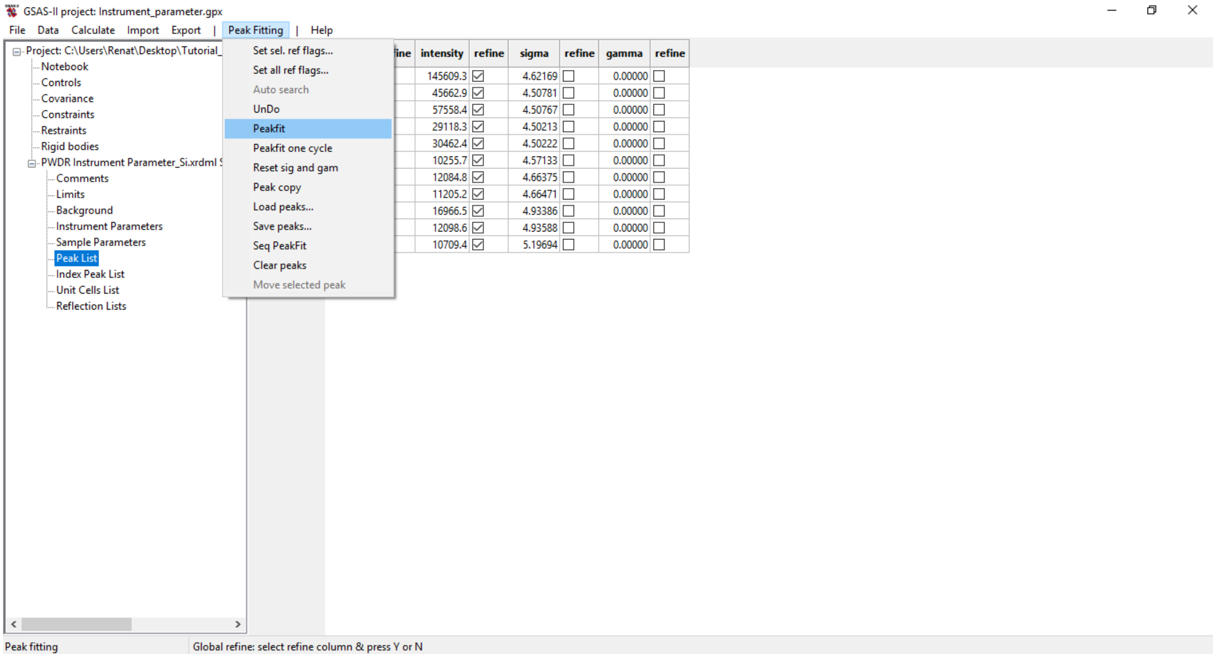

intensity	refine	sigma	refine	gamma	refine
145609.3	☑	4.62169	☐	0.00000	☐
45662.9	☑	4.50781	☐	0.00000	☐
57558.4	☑	4.50767	☐	0.00000	☐
29118.3	☑	4.50213	☐	0.00000	☐
30462.4	☑	4.50222	☐	0.00000	☐
10255.7	☑	4.57133	☐	0.00000	☐
12084.8	☑	4.66375	☐	0.00000	☐
11205.2	☑	4.66471	☐	0.00000	☐
16966.5	☑	4.93386	☐	0.00000	☐
12098.6	☑	4.93588	☐	0.00000	☐
10709.4	☑	5.19694	☐	0.00000	☐

Peak fitting

Global refine: select refine column & press Y or N

Figure 6.28: Fitting the XRD data values again.

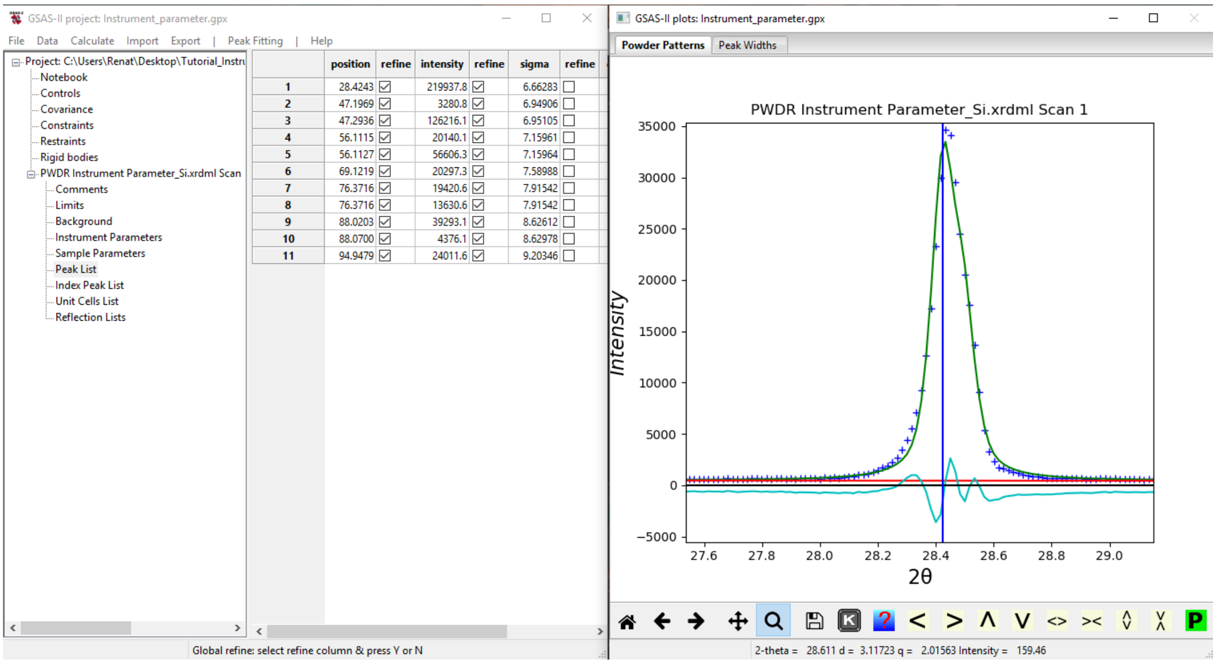

	position	refine	intensity	refine	sigma	refine
1	28.4243	☑	219937.8	☑	6.66283	☐
2	47.1969	☑	3280.8	☑	6.94906	☐
3	47.2936	☑	126216.1	☑	6.95105	☐
4	56.1115	☑	20140.1	☑	7.15961	☐
5	56.1127	☑	56606.3	☑	7.15964	☐
6	69.1219	☑	20297.3	☑	7.58988	☐
7	76.3716	☑	19420.6	☑	7.91542	☐
8	76.3716	☑	13630.6	☑	7.91542	☐
9	88.0203	☑	39293.1	☑	8.62612	☐
10	88.0700	☑	4376.1	☑	8.62978	☐
11	94.9479	☑	24011.6	☑	9.20346	☐

Global refine: select refine column & press Y or N

2-theta = 28.611 d = 3.11723 q = 2.01563 Intensity = 159.46

Figure 6.29: On the right a zoom in on the XRD spectra shows the calcuted values well fitted with the experimental values.

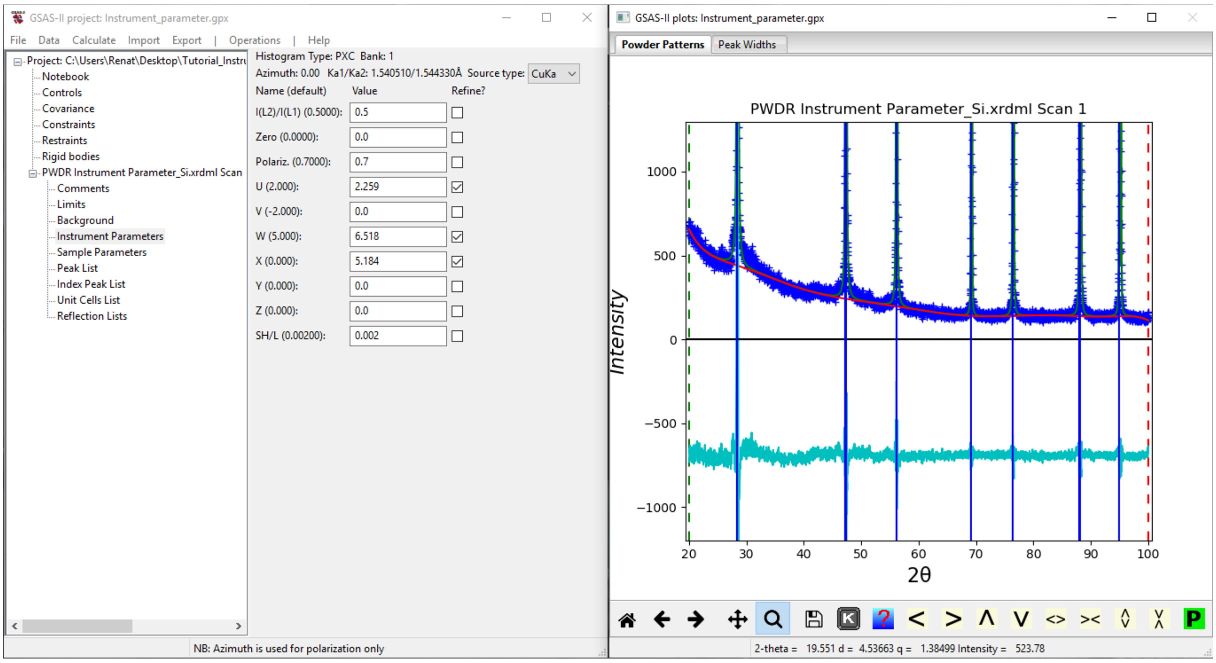

Histogram Type: PXC Bank: 1

Azimuth: 0.00 Ka1/Ka2: 1.540510/1.544330Å Source type: CuKa

Name (default)	Value	Refine?
I(L2)/I(L1) (0.5000):	0.5	☐
Zero (0.0000):	0.0	☐
Polariz. (0.7000):	0.7	☐
U (2.000):	2.259	☑
V (-2.000):	0.0	☐
W (5.000):	6.518	☑
X (0.000):	5.184	☑
Y (0.000):	0.0	☐
Z (0.000):	0.0	☐
SH/L (0.00200):	0.002	☐

NB: Azimuth is used for polarization only

2-theta = 19.551 d = 4.53663 q = 1.38499 Intensity = 523.78

Figure 6.30: On the left some instrument parameters already refined and other set to default minima. On the right the XRD spectra (blue) fitted as well as the background (red).

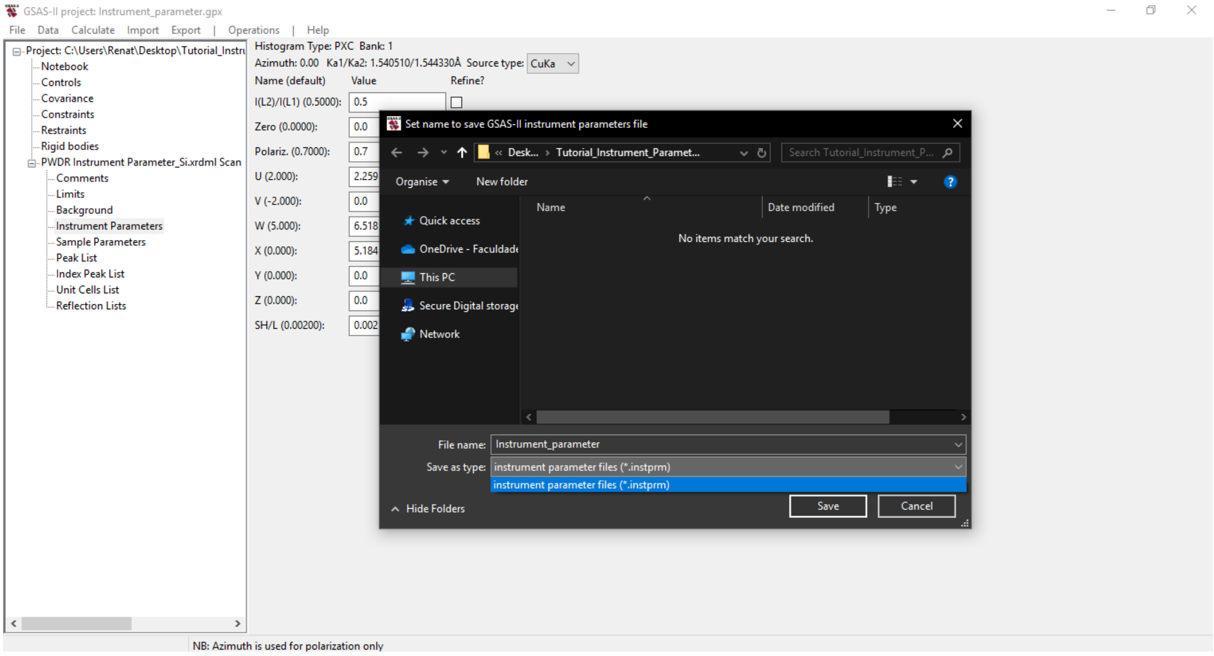
GSAS-II project: Instrument_parameter.gpx

Project: C:\Users\Renat\Desktop\Tutorial_Instru

PWDR Instrument Parameter_Si.xrdml Scan

Histogram Type: PXC Bank: 1

Azimuth: 0.00 Ka1/Ka2: 1.540510/1.544330Å Source type: CuKa

Name (default)	Value	Refine?
I(L2)/I(L1) (0.5000):	0.5	☐
Zero (0.0000):	0.0	
Polariz. (0.7000):	0.7	
U (2.000):	2.259	
V (-2.000):	0.0	
W (5.000):	6.518	
X (0.000):	5.184	
Y (0.000):	0.0	
Z (0.000):	0.0	
SH/L (0.00200):	0.002	

Set name to save GSAS-II instrument parameters file

No items match your search.

File name: Instrument_parameter

Save as type: instrument parameter files (*.instprm)

NB: Azimuth is used for polarization only

Figure 6.31: Saving the instrument parameter file for future use.

From now on the instrument parameter file is settled. What comes next is the Rietveld Refinement itself. First thing to do is select new project as done previously on Figure 6.11. Then import the XRD file that´s supposed to refine (Figure 6.12). A window must appear (Figure 6.32) for choosing the instrument parameter file (saved as .instprm) created before (Figure 6.31). On the data tree select background and choose 10 numbers of coefficients for the background function as done on Figure 6.18.

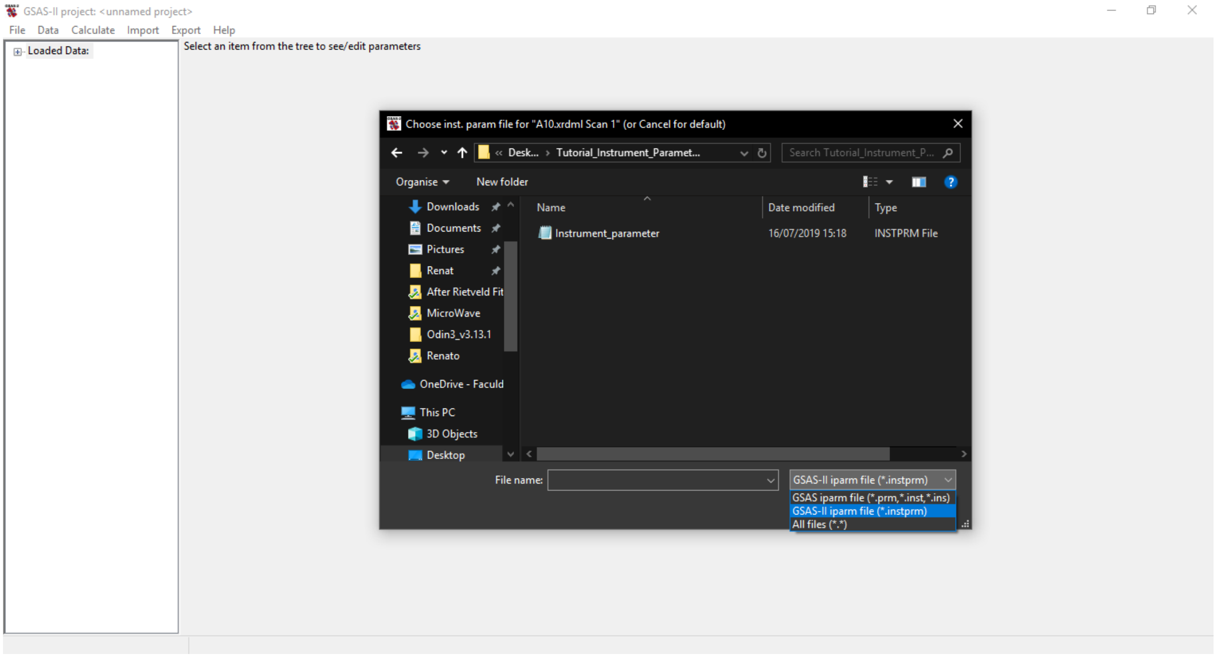
GSAS-II project: <unnamed project>

Select an item from the tree to see/edit parameters

Choose inst. param file for "A10.xrdml Scan 1" (or Cancel for default)

Name	Date modified	Type
Instrument_parameter	16/07/2019 15:18	INSTPRM File

File name:

GSAS-II iparm file (*.instprm)

Figure 6.32: Selecting the properly file to open.

Next step must be changing the type of diffractometer to Bragg-Bretano as seen in Figure 6.33. Afterwards its necessary to import a phase to work with (Figure 6.34). In this work a ZnO phase cif file was used (Figure 6.35). After that a histogram must be added to the new phase to continue the refinement as shown on Figure 6.36.

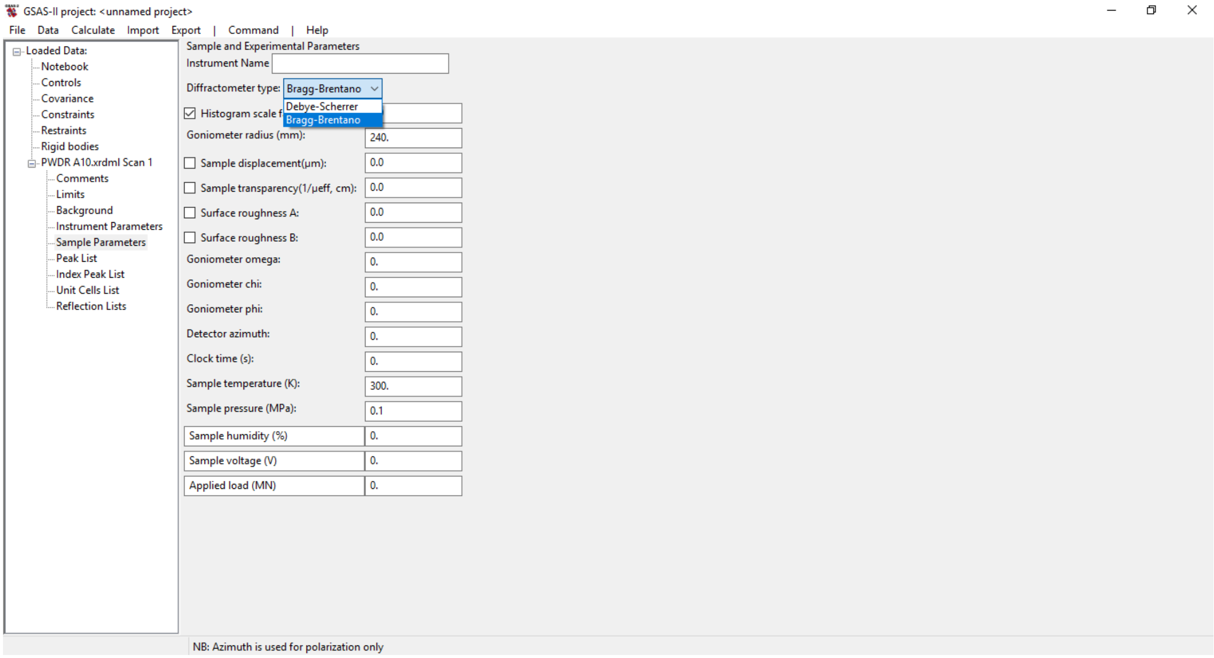

Sample and Experimental Parameters
Instrument Name
Diffractometer type: Bragg-Brentano
☑ Histogram scale f
Goniometer radius (mm): 240.
☐ Sample displacement(µm): 0.0
☐ Sample transparency(1/µeff, cm): 0.0
☐ Surface roughness A: 0.0
☐ Surface roughness B: 0.0
Goniometer omega: 0.
Goniometer chi: 0.
Goniometer phi: 0.
Detector azimuth: 0.
Clock time (s): 0.
Sample temperature (K): 300.
Sample pressure (MPa): 0.1
Sample humidity (%) 0.
Sample voltage (V) 0.
Applied load (MN) 0.
NB: Azimuth is used for polarization only

Figure 6.33: Selecting Bragg-Brettano diffractometer type.

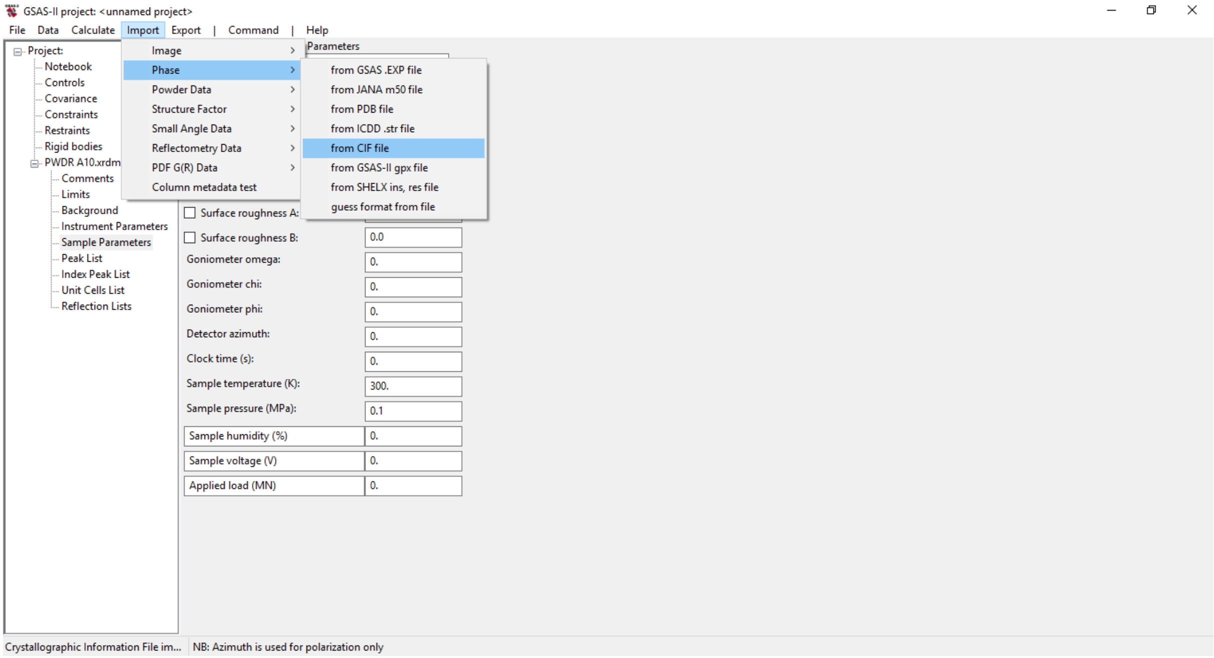

☐ Surface roughness A:
☐ Surface roughness B: 0.0
Goniometer omega: 0.
Goniometer chi: 0.
Goniometer phi: 0.
Detector azimuth: 0.
Clock time (s): 0.
Sample temperature (K): 300.
Sample pressure (MPa): 0.1
Sample humidity (%) 0.
Sample voltage (V) 0.
Applied load (MN) 0.
Crystallographic Information File im...
NB: Azimuth is used for polarization only

Figure 6.34: Importing a ZnO phase as a CIF file.

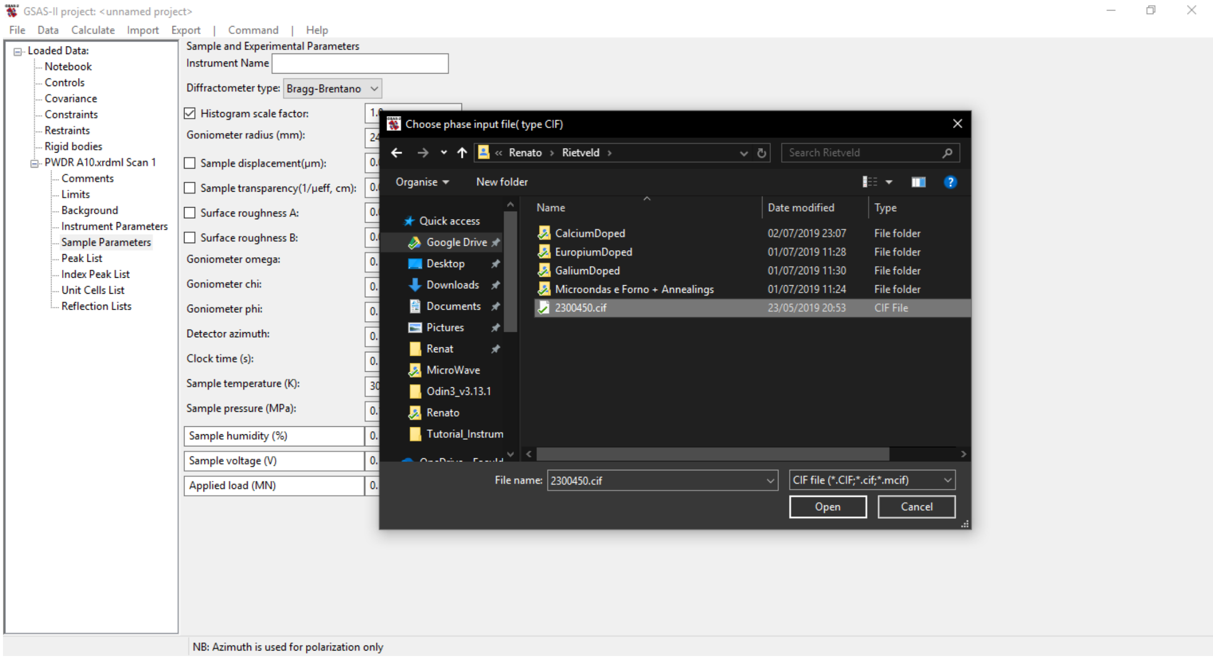

Sample and Experimental Parameters

Instrument Name:

Diffractometer type: Bragg-Brentano

☑ Histogram scale factor: 1.

Goniometer radius (mm): 24

☐ Sample displacement(μm): 0.

☐ Sample transparency(1/μeff, cm): 0.

☐ Surface roughness A: 0.

☐ Surface roughness B: 0.

Goniometer omega: 0.

Goniometer chi: 0.

Goniometer phi: 0.

Detector azimuth: 0.

Clock time (s): 0.

Sample temperature (K): 30

Sample pressure (MPa): 0.

Sample humidity (%): 0.

Sample voltage (V): 0.

Applied load (MN): 0.

NB: Azimuth is used for polarization only

Choose phase input file(type CIF)

« Renato › Rietveld ›

Name	Date modified	Type
CalciumDoped	02/07/2019 23:07	File folder
EuropiumDoped	01/07/2019 11:28	File folder
GaliumDoped	01/07/2019 11:30	File folder
Microondas e Forno + Annealings	01/07/2019 11:24	File folder
2300450.cif	23/05/2019 20:53	CIF File

File name: 2300450.cif

CIF file (*.CIF;*.cif;*.mcif)

Figure 6.35: Choosing the ZnO phase CIF file.

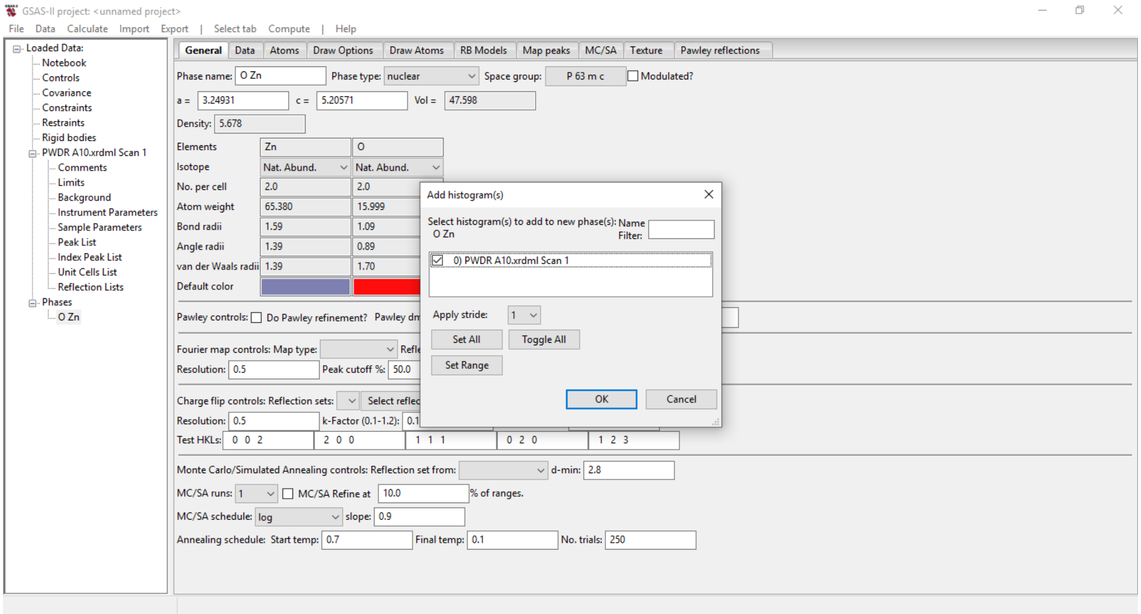

Phase name: O Zn Phase type: nuclear Space group: P 63 m c ☐ Modulated?

a = 3.24931 c = 5.20571 Vol = 47.598

Density: 5.678

Elements	Zn	O
Isotope	Nat. Abund.	Nat. Abund.
No. per cell	2.0	2.0
Atom weight	65.380	15.999
Bond radii	1.59	1.09
Angle radii	1.39	0.89
van der Waals radii	1.39	1.70
Default color	🟪	🟥

Pawley controls: ☐ Do Pawley refinement? Pawley dm

Fourier map controls: Map type: Refle

Resolution: 0.5 Peak cutoff %: 50.0

Charge flip controls: Reflection sets: Select reflec

Resolution: 0.5 k-Factor (0.1-1.2): 0.1

Test HKLs: 0 0 2 2 0 0 1 1 1 0 2 0 1 2 3

Monte Carlo/Simulated Annealing controls: Reflection set from: d-min: 2.8

MC/SA runs: 1 ☐ MC/SA Refine at 10.0 % of ranges.

MC/SA schedule: log slope: 0.9

Annealing schedule: Start temp: 0.7 Final temp: 0.1 No. trials: 250

Add histogram(s)

Select histogram(s) to add to new phase(s): O Zn Name Filter:

☑ 0) PWDR A10.xrdml Scan 1

Apply stride: 1

Figure 6.36: Selecting the histogram to add the new phase.

From now on refinement of the parameters can be started. Primarily start with refining the background and histogram scale factor (Figure 6.37). Then unit cell parameters a and c must be refined (Figure 6.38). Afterwards instrument parameters need to be refined. Starting with zero parameter (Figure 6.39), then U parameter (Figure 6.40) joined by V parameter (Figure 6.41) and at last U parameter as shown on Figure 6.42. To improve the results thermal parameters are refined (Figure 6.43). Now a zoom in on the three most important peaks shows a well fitted curve with the full width at half maximum calculated values close to the observed ones.

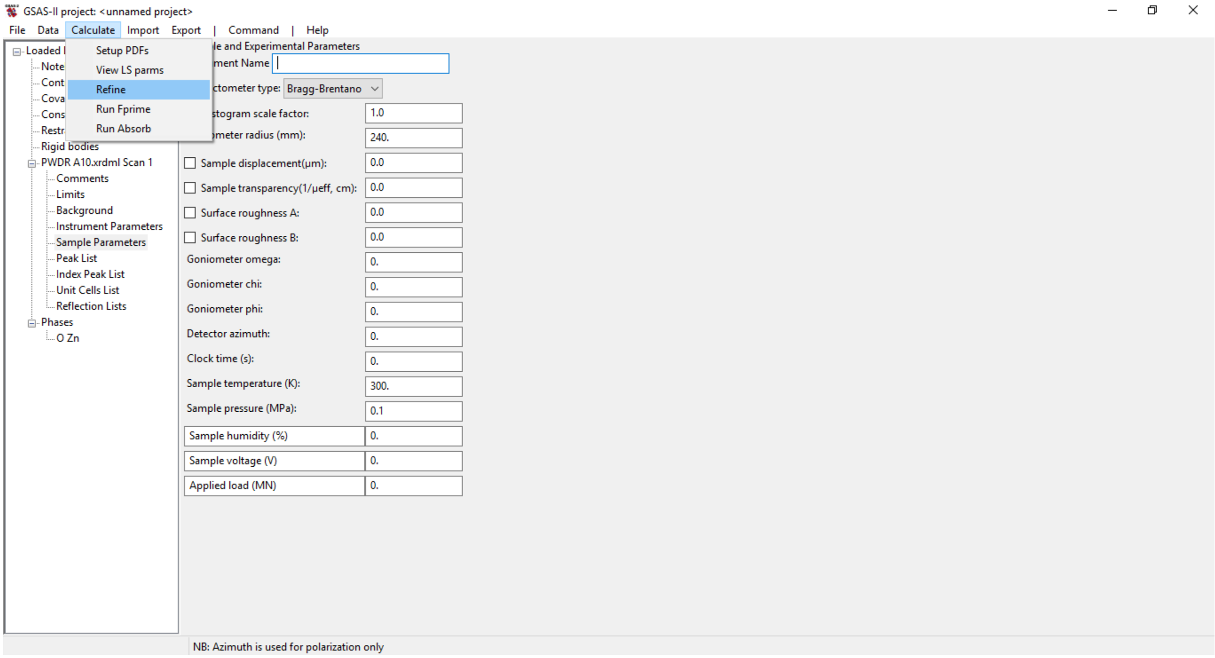

le and Experimental Parameters

ment Name

ctometer type: Bragg-Brentano

stogram scale factor: 1.0

meter radius (mm): 240.

☐ Sample displacement(μm): 0.0

☐ Sample transparency(1/μeff, cm): 0.0

☐ Surface roughness A: 0.0

☐ Surface roughness B: 0.0

Goniometer omega: 0.

Goniometer chi: 0.

Goniometer phi: 0.

Detector azimuth: 0.

Clock time (s): 0.

Sample temperature (K): 300.

Sample pressure (MPa): 0.1

Sample humidity (%): 0.

Sample voltage (V): 0.

Applied load (MN): 0.

NB: Azimuth is used for polarization only

Figure 6.37: Refining the background and histogram scale factor.

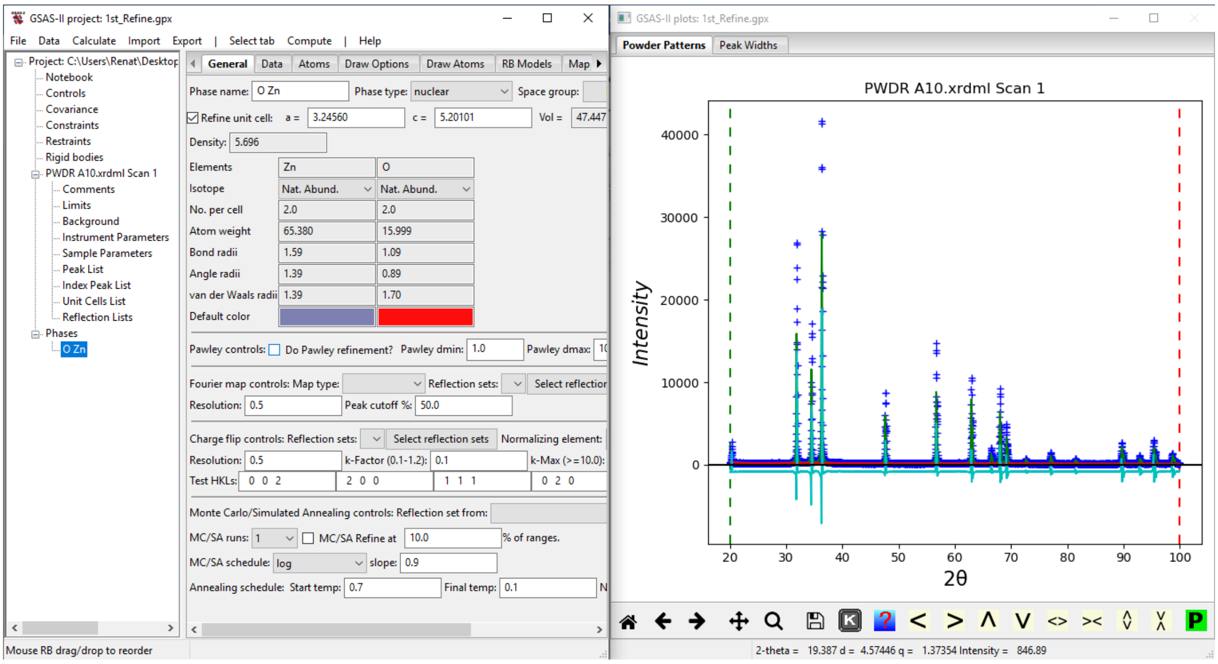

Phase name: O Zn Phase type: nuclear Space group:

☑ Refine unit cell: a = 3.24560 c = 5.20101 Vol = 47.447

Density: 5.696

Elements	Zn	O
Isotope	Nat. Abund.	Nat. Abund.
No. per cell	2.0	2.0
Atom weight	65.380	15.999
Bond radii	1.59	1.09
Angle radii	1.39	0.89
van der Waals radii	1.39	1.70
Default color	▨	🟥

Pawley controls: ☐ Do Pawley refinement? Pawley dmin: 1.0 Pawley dmax: 1(

Fourier map controls: Map type: Reflection sets: Select reflection

Resolution: 0.5 Peak cutoff %: 50.0

Charge flip controls: Reflection sets: Select reflection sets Normalizing element:

Resolution: 0.5 k-Factor (0.1-1.2): 0.1 k-Max (>=10.0):

Test HKLs: 0 0 2 2 0 0 1 1 1 0 2 0

Monte Carlo/Simulated Annealing controls: Reflection set from:

MC/SA runs: 1 ☐ MC/SA Refine at 10.0 % of ranges.

MC/SA schedule: log slope: 0.9

Annealing schedule: Start temp: 0.7 Final temp: 0.1 N

2-theta = 19.387 d = 4.57446 q = 1.37354 Intensity = 846.89

Figure 6.38: Refining unit cell.

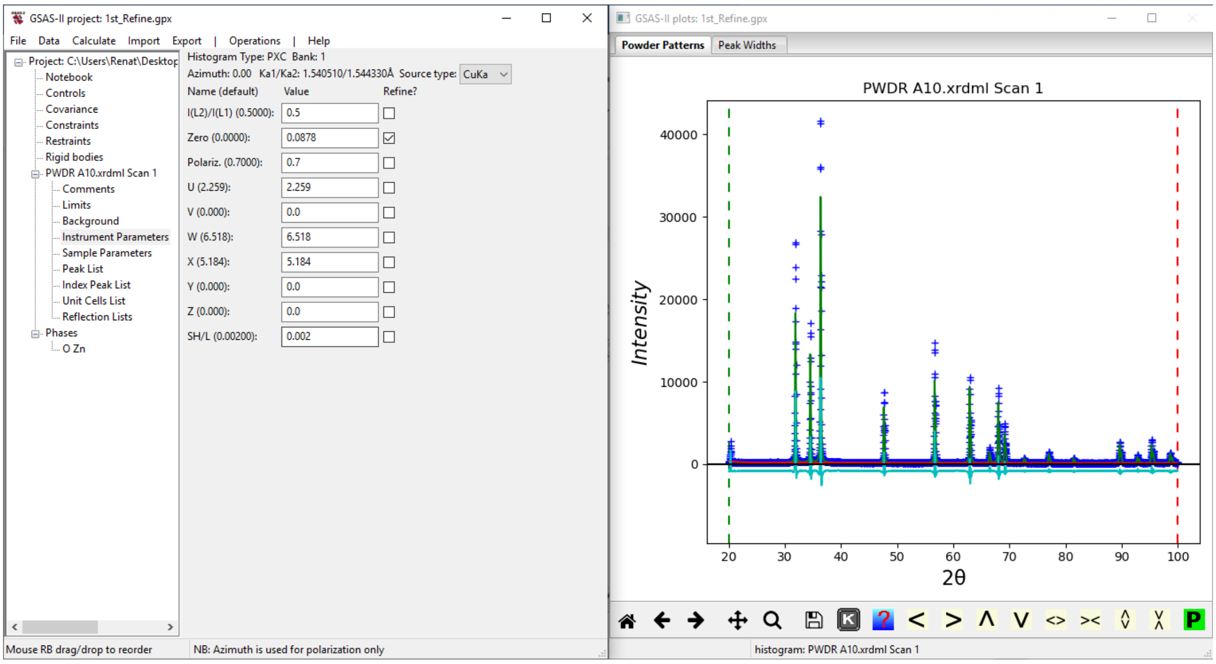

Histogram Type: PXC Bank: 1
Azimuth: 0.00 Ka1/Ka2: 1.540510/1.544330Å Source type: CuKa

Name (default)	Value	Refine?
I(L2)/I(L1) (0.5000):	0.5	☐
Zero (0.0000):	0.0878	☑
Polariz. (0.7000):	0.7	☐
U (2.259):	2.259	☐
V (0.000):	0.0	☐
W (6.518):	6.518	☐
X (5.184):	5.184	☐
Y (0.000):	0.0	☐
Z (0.000):	0.0	☐
SH/L (0.00200):	0.002	☐

NB: Azimuth is used for polarization only

Figure 6.39: Refining Zero parameter.

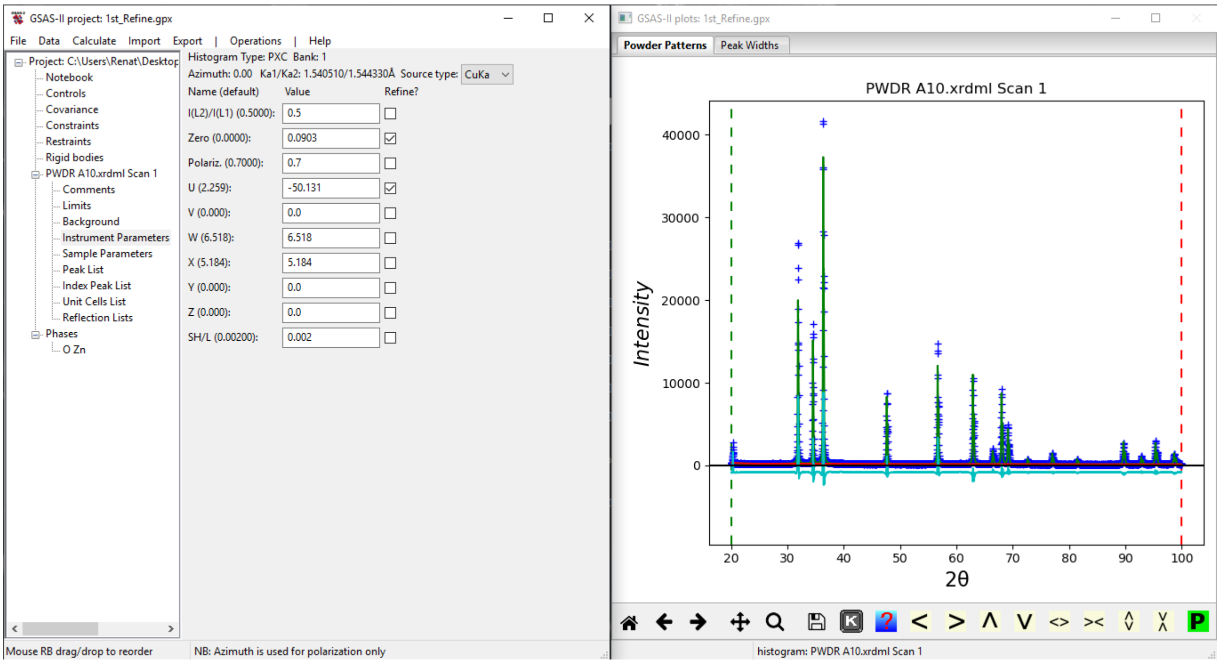

Histogram Type: PXC Bank: 1
Azimuth: 0.00 Ka1/Ka2: 1.540510/1.544330Å Source type: CuKa

Name (default)	Value	Refine?
I(L2)/I(L1) (0.5000):	0.5	☐
Zero (0.0000):	0.0903	☑
Polariz. (0.7000):	0.7	☐
U (2.259):	-50.131	☑
V (0.000):	0.0	☐
W (6.518):	6.518	☐
X (5.184):	5.184	☐
Y (0.000):	0.0	☐
Z (0.000):	0.0	☐
SH/L (0.00200):	0.002	☐

NB: Azimuth is used for polarization only

Figure 6.40: Refining Zero + U parameters.

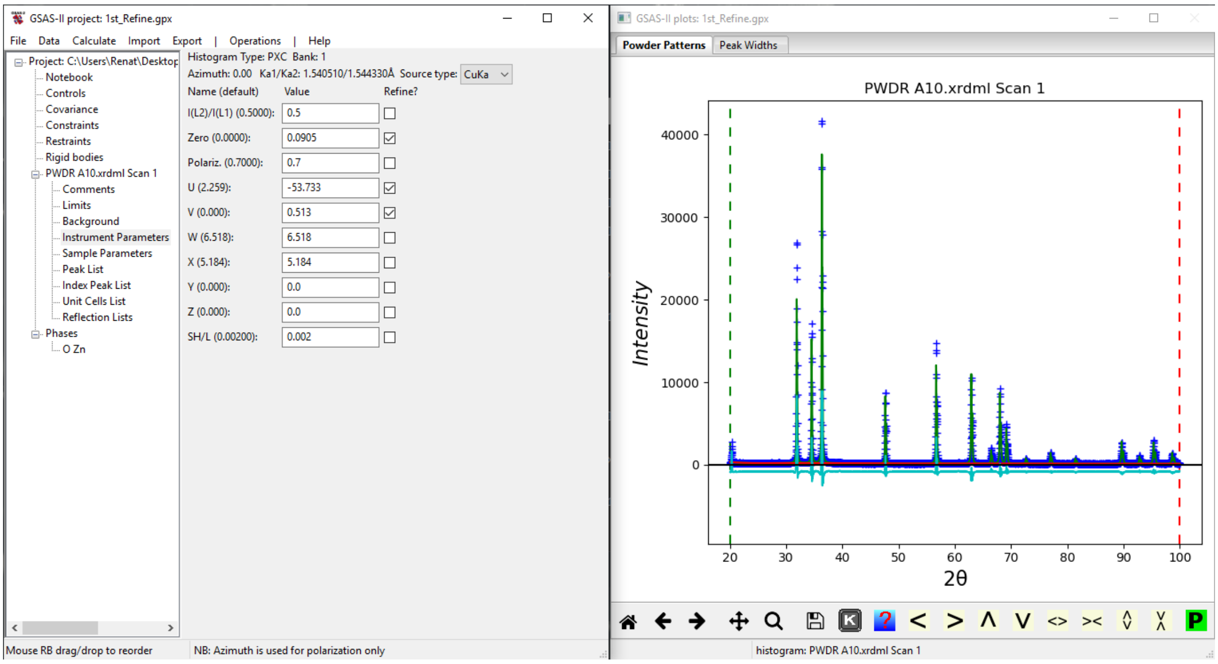

Histogram Type: PXC Bank: 1

Azimuth: 0.00 Ka1/Ka2: 1.540510/1.544330Å Source type: CuKa

Name (default)	Value	Refine?
I(L2)/I(L1) (0.5000):	0.5	☐
Zero (0.0000):	0.0905	☑
Polariz. (0.7000):	0.7	☐
U (2.259):	-53.733	☑
V (0.000):	0.513	☑
W (6.518):	6.518	☐
X (5.184):	5.184	☐
Y (0.000):	0.0	☐
Z (0.000):	0.0	☐
SH/L (0.00200):	0.002	☐

Figure 6.41: Refining Zero + U + V parameters.

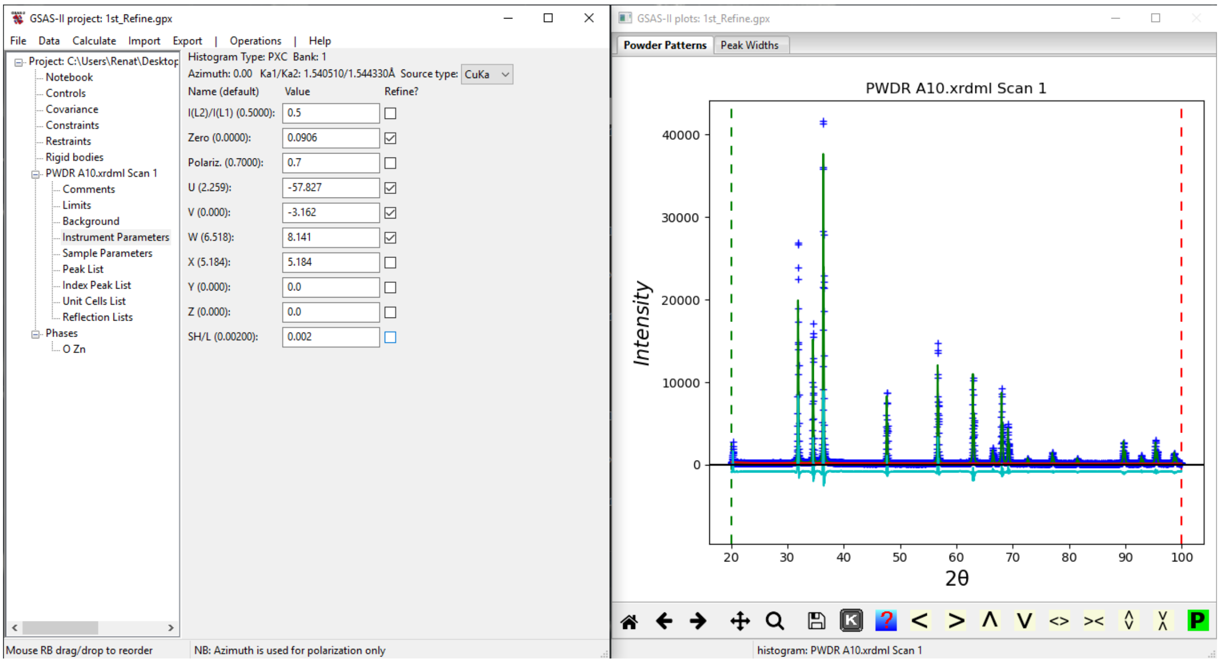

Histogram Type: PXC Bank: 1

Azimuth: 0.00 Ka1/Ka2: 1.540510/1.544330Å Source type: CuKa

Name (default)	Value	Refine?
I(L2)/I(L1) (0.5000):	0.5	☐
Zero (0.0000):	0.0906	☑
Polariz. (0.7000):	0.7	☐
U (2.259):	-57.827	☑
V (0.000):	-3.162	☑
W (6.518):	8.141	☑
X (5.184):	5.184	☐
Y (0.000):	0.0	☐
Z (0.000):	0.0	☐
SH/L (0.00200):	0.002	☐

Figure 6.42: Refining zero + U + V + W parameters.

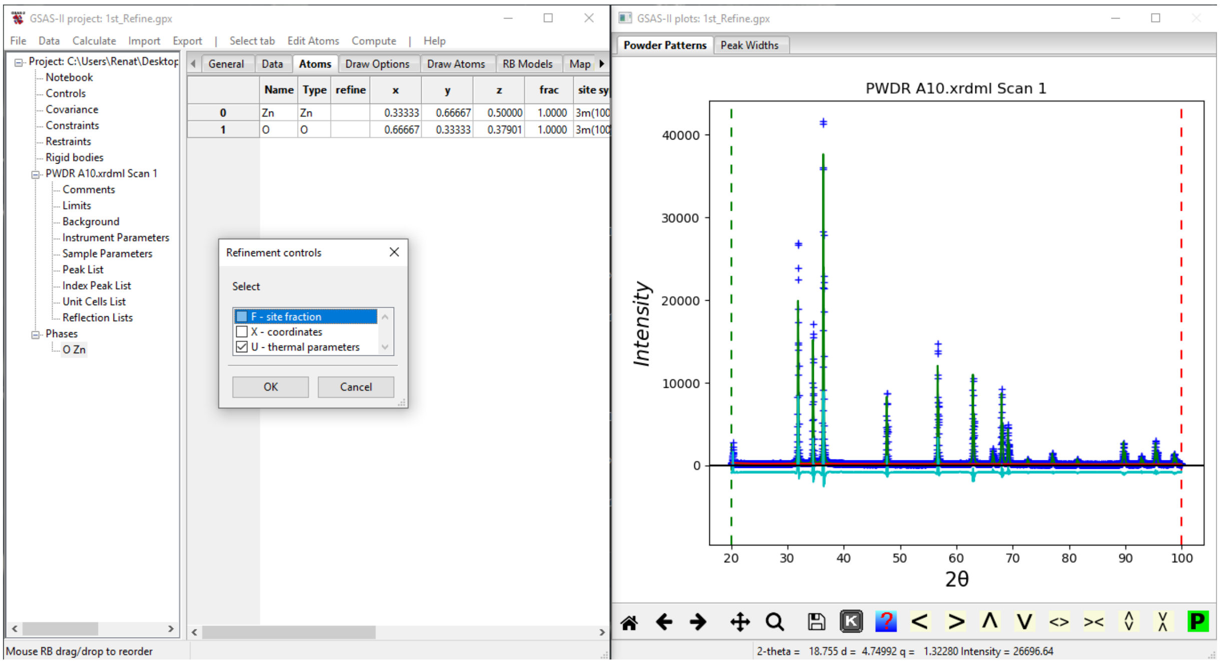

	Name	Type	refine	x	y	z	frac	site sy
0	Zn	Zn		0.33333	0.66667	0.50000	1.0000	3m(100
1	O	O		0.66667	0.33333	0.37901	1.0000	3m(100

Refinement controls

Select

☐ F - site fraction
☐ X - coordinates
☑ U - thermal parameters

2-theta = 18.755 d = 4.74992 q = 1.32280 Intensity = 26696.64

Figure 6.43: Refining thermal parameters.

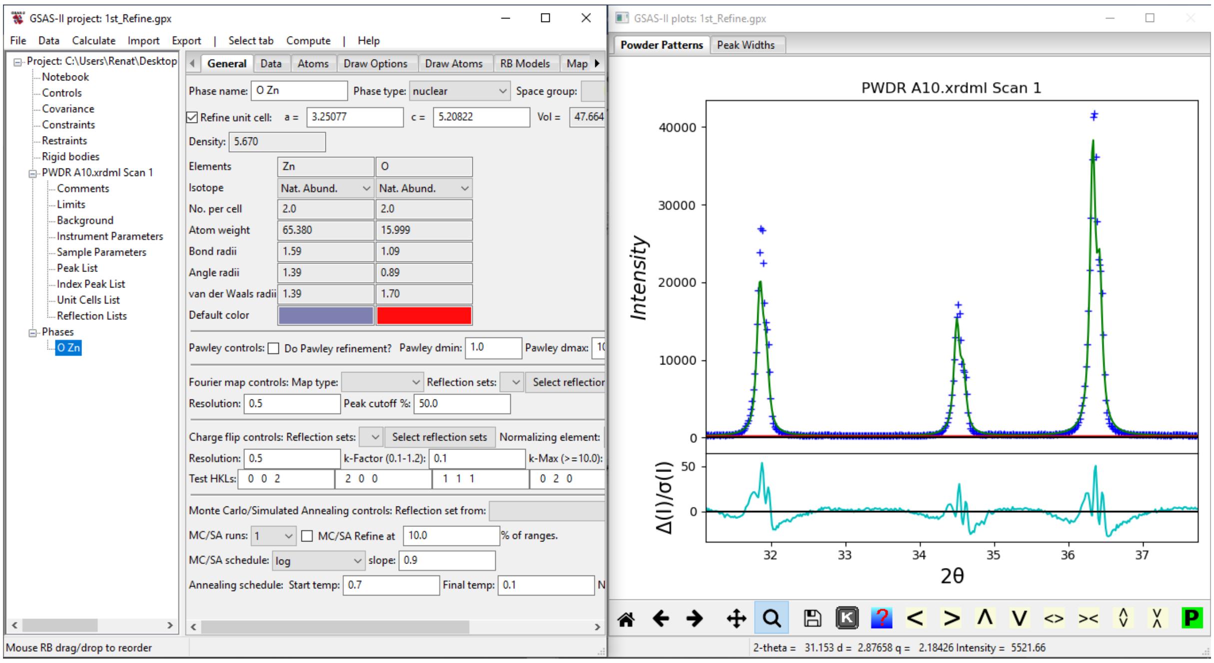

Phase name: O Zn Phase type: nuclear Space group:

☑ Refine unit cell: a = 3.25077 c = 5.20822 Vol = 47.664

Density: 5.670

Elements	Zn	O
Isotope	Nat. Abund.	Nat. Abund.
No. per cell	2.0	2.0
Atom weight	65.380	15.999
Bond radii	1.59	1.09
Angle radii	1.39	0.89
van der Waals radii	1.39	1.70
Default color	🟪	🟥

Pawley controls: ☐ Do Pawley refinement? Pawley dmin: 1.0 Pawley dmax: 1(

Fourier map controls: Map type: Reflection sets:

Resolution: 0.5 Peak cutoff %: 50.0

Charge flip controls: Reflection sets: Normalizing element:

Resolution: 0.5 k-Factor (0.1-1.2): 0.1 k-Max (>=10.0):

Test HKLs: 0 0 2 | 2 0 0 | 1 1 1 | 0 2 0

Monte Carlo/Simulated Annealing controls: Reflection set from:

MC/SA runs: 1 ☐ MC/SA Refine at 10.0 % of ranges.

MC/SA schedule: log slope: 0.9

Annealing schedule: Start temp: 0.7 Final temp: 0.1

2-theta = 31.153 d = 2.87658 q = 2.18426 Intensity = 5521.66

Figure 6.44: On the left lattice parameters a and c refined. On the right a zoom in of the three important peaks.

As far as this work is concerned the refinement reach the best results so the Rietveld refinement is concluded. Notice that this refinement doesn´t have an end so it can be done until it gets a better fitting of the calculated profile and the observed data.

LOMBADA

[Título da Dissertação] (Tipo de letra: Arial, 10pt normal)

[Primeiro e último nome do candidato(a)] *(Tipo de letra: Arial, 10pt normal)*